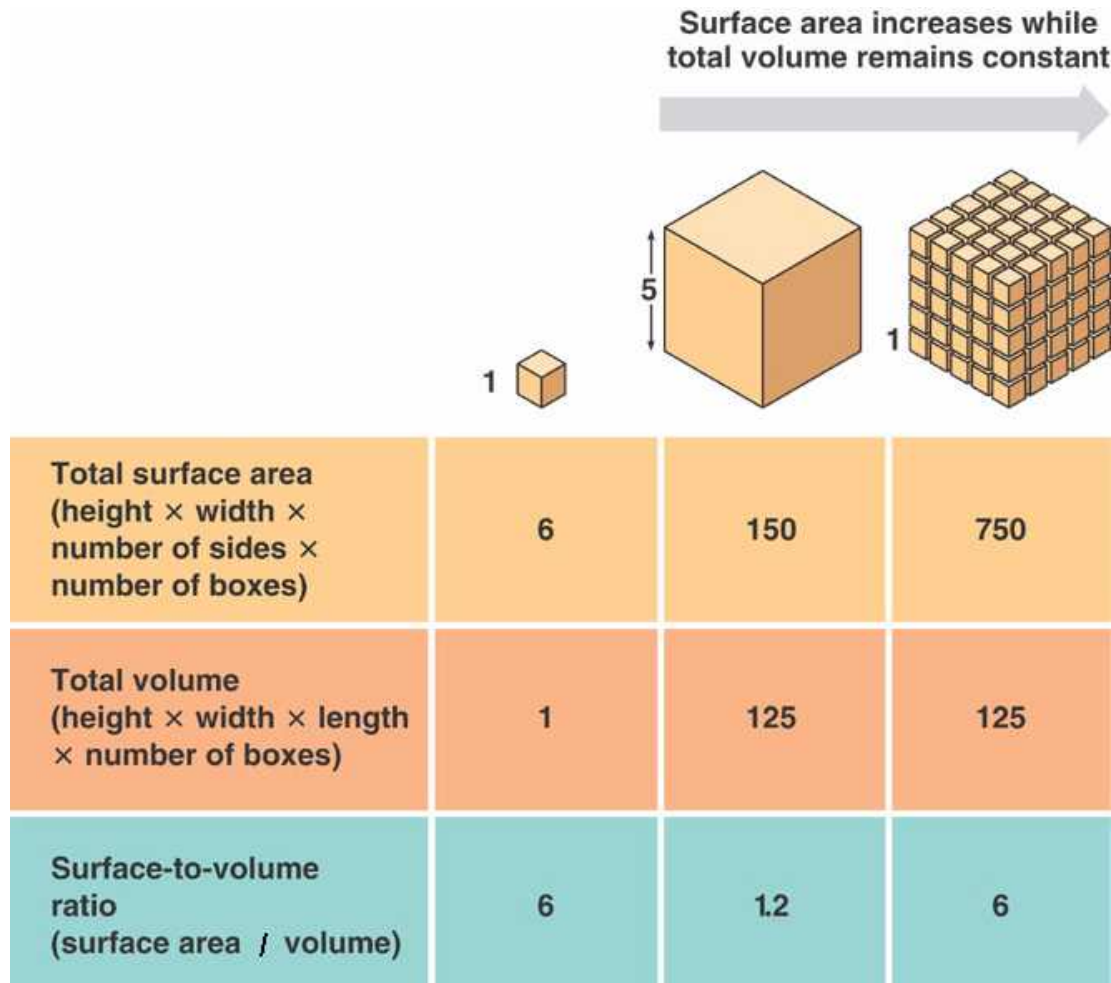
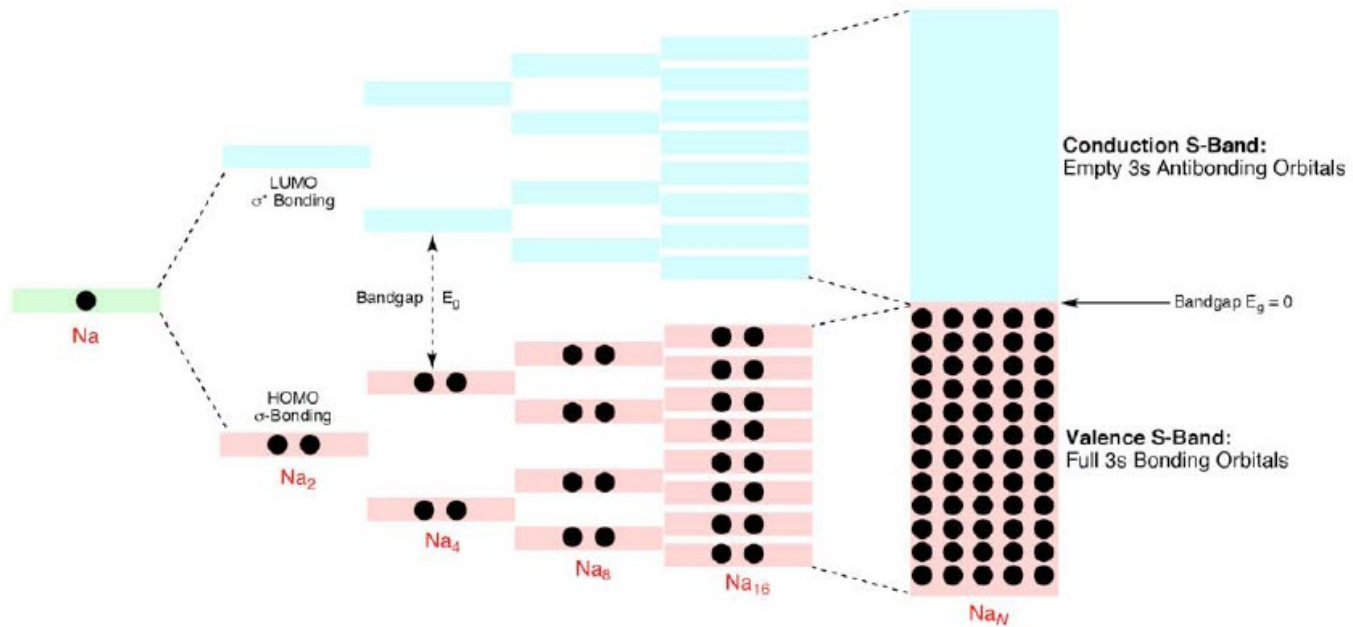
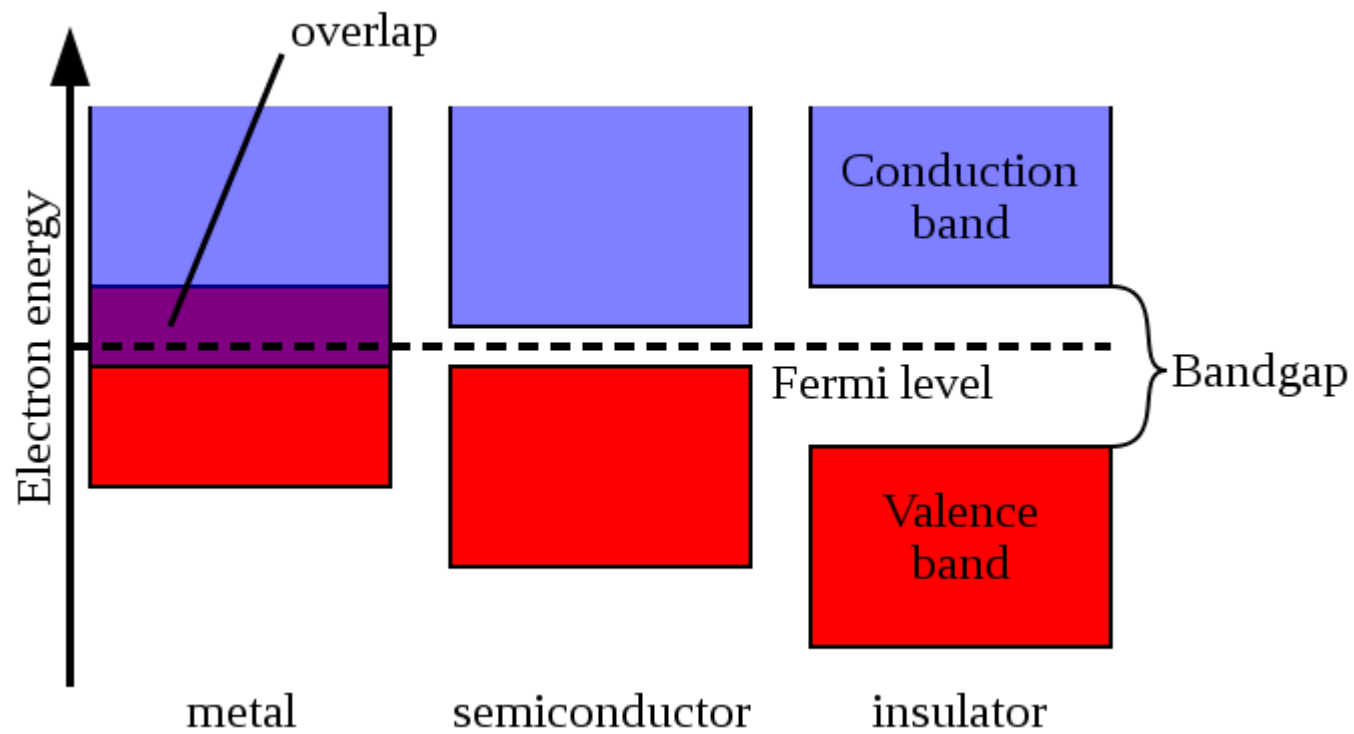


Surface to Volume Ratio

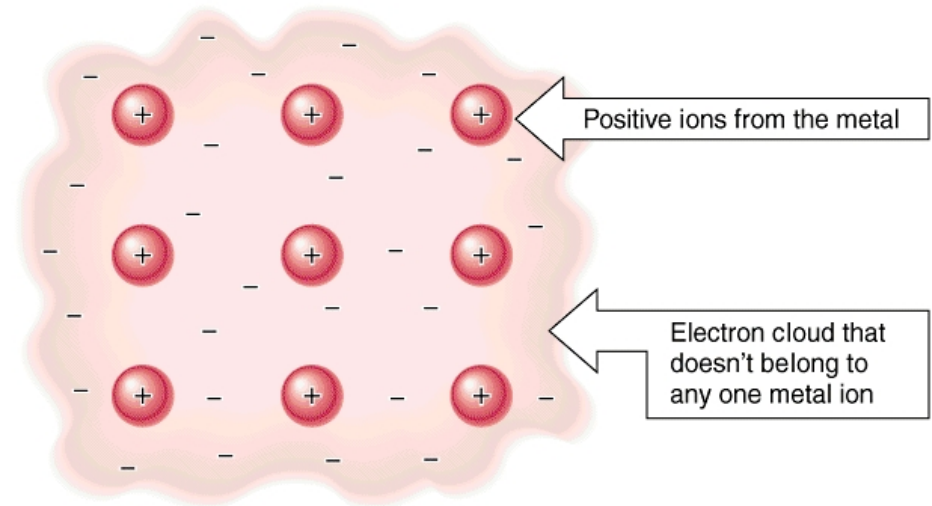
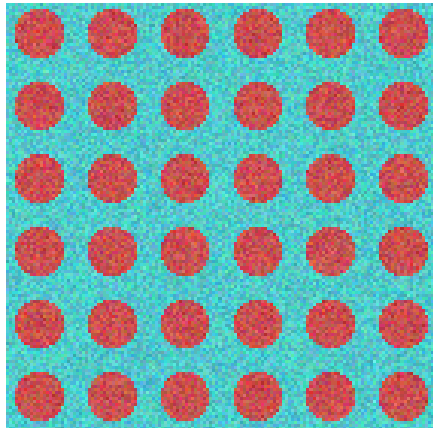


Bandgap





Electron Sea

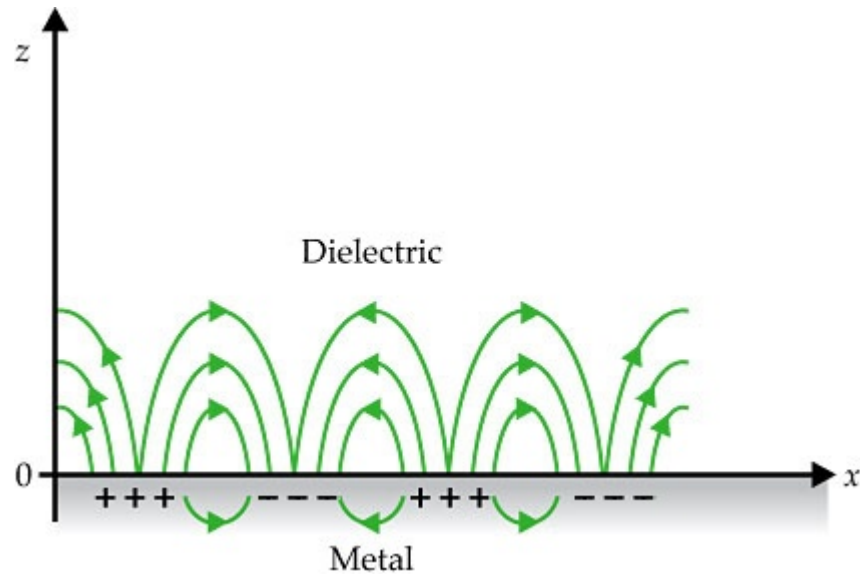


Copyright 1998 by John Wiley and Sons, Inc. All rights reserved.

$$m \frac{d^2 \delta x}{dt^2} = e E_x = -m \omega_p^2 \delta x,$$

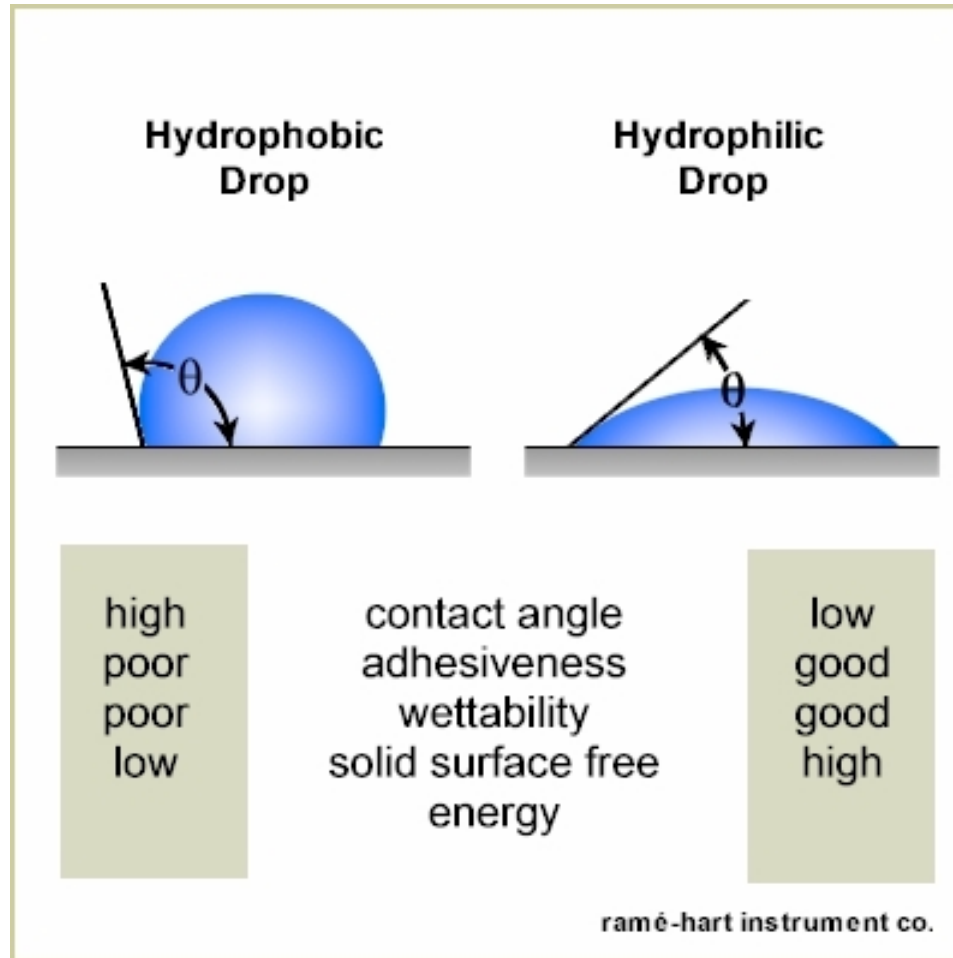
$$\omega_p^2 = \frac{n e^2}{\epsilon_0 m},$$

Surface Plasmon



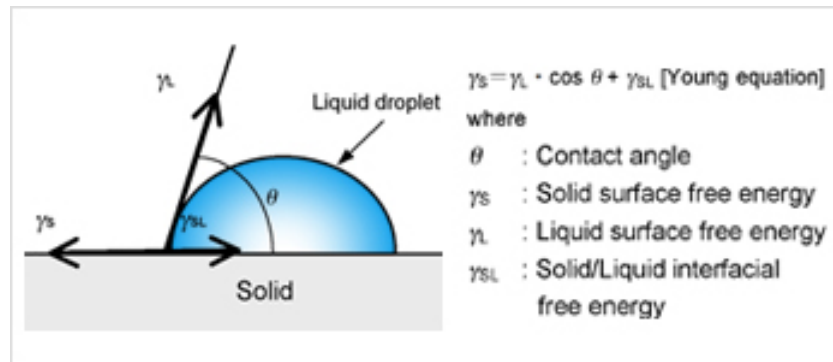
$$\epsilon_m = 1 - \frac{\omega_p^2}{\omega^2}$$

Contact Angle

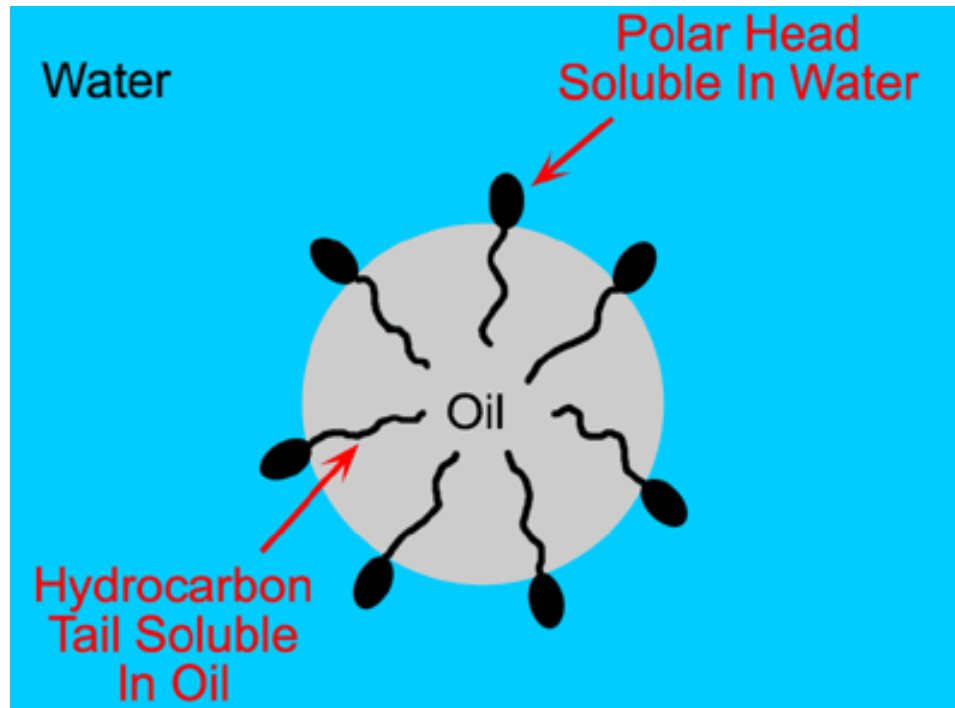


Young's Equation

$$\gamma_{SL} + \gamma_{LV} \cos \theta_c = \gamma_{SV}$$



Surfactant



DLVO Theory

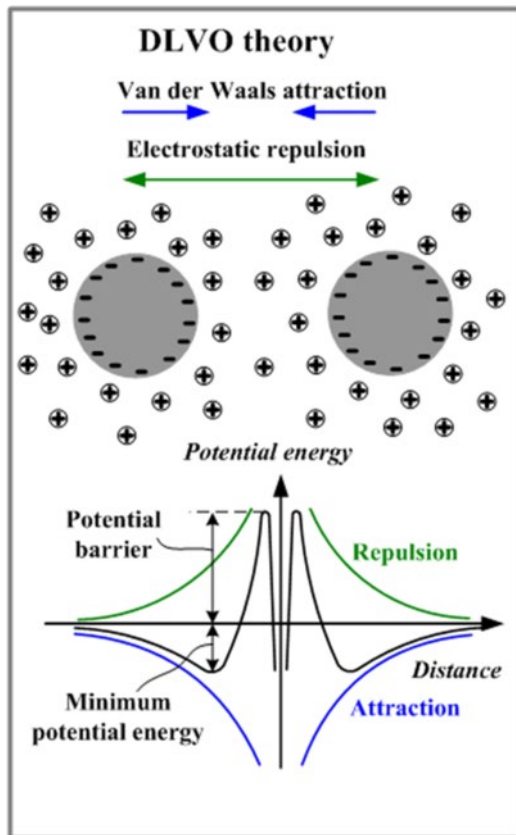
$$V_T = V_A + V_R + V_S$$

$$V_A = -A/(12 \pi D^2)$$

A is the Hamaker constant and D is the particle separation

$$V_R = 2 \pi \epsilon a \xi^2 \exp(-\kappa D)$$

a is the particle radius, π is the solvent permeability,
 κ is a function of the ionic composition and ξ is the zeta potential

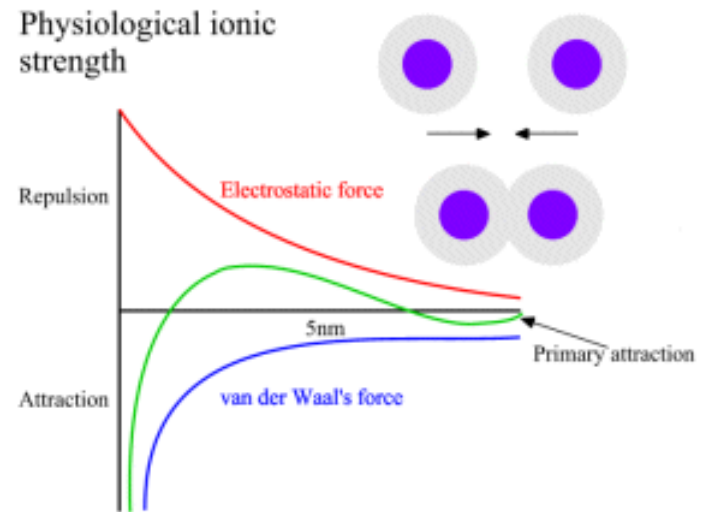
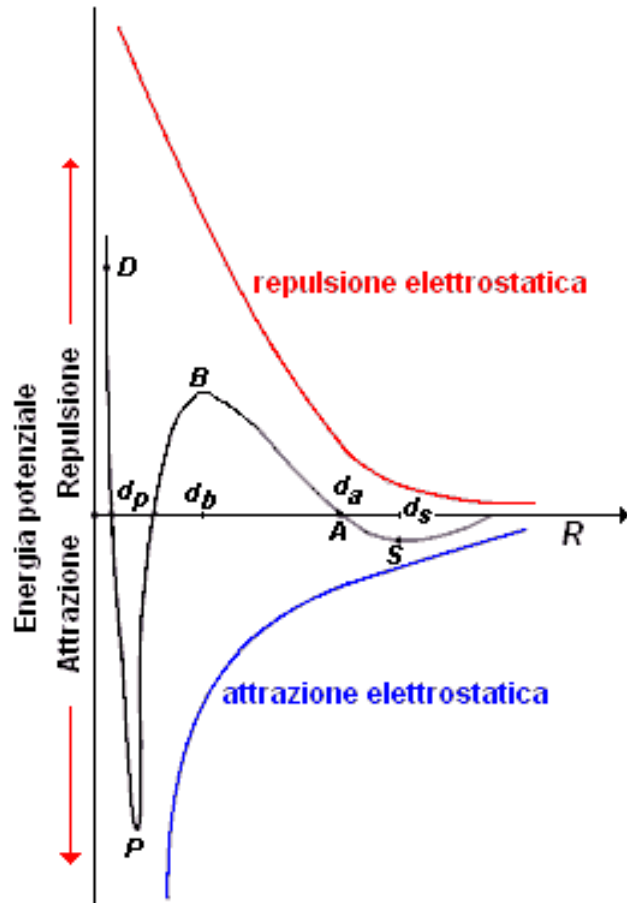


$$\omega = \omega_{el} + \omega_{vdW}$$

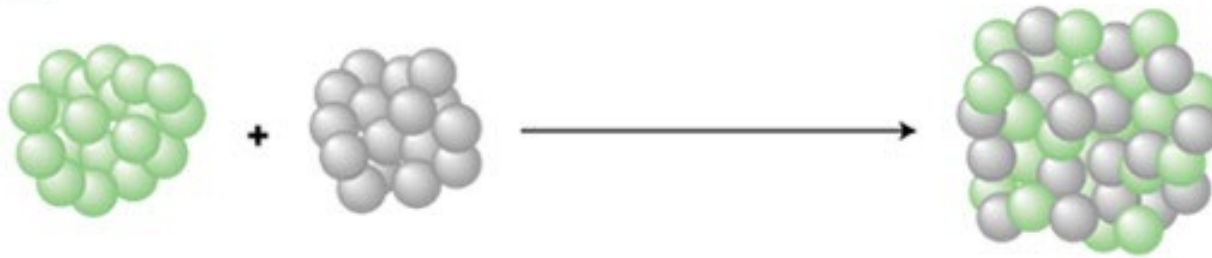
$$\omega = 64RTc_{\infty}\gamma_0^2 \frac{1}{\kappa} e^{-\kappa d} - \frac{A}{12\pi d^2}$$

$$\omega = 64RTc_{\infty}\gamma_0^2 \sqrt{\frac{RT\varepsilon}{F^2 \sum z^2 c_{\infty}}} e^{-\sqrt{\frac{F^2 \sum z^2 c_{\infty}}{RT\varepsilon}} d} - \frac{A}{12\pi d^2}$$

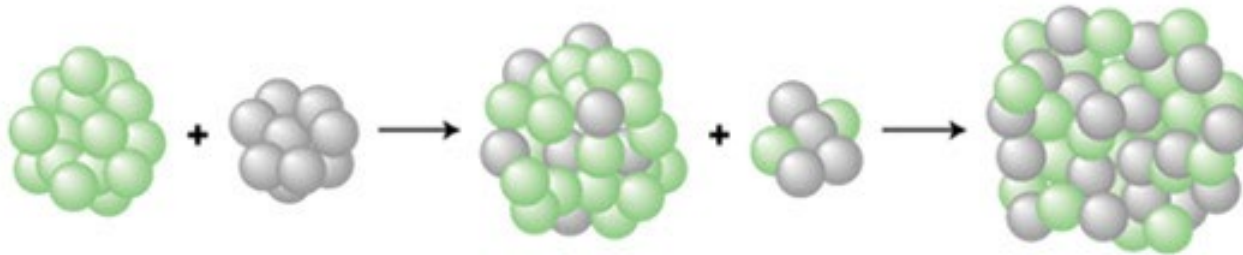
DLVO Theory



a Coalescence



b Ostwald ripening



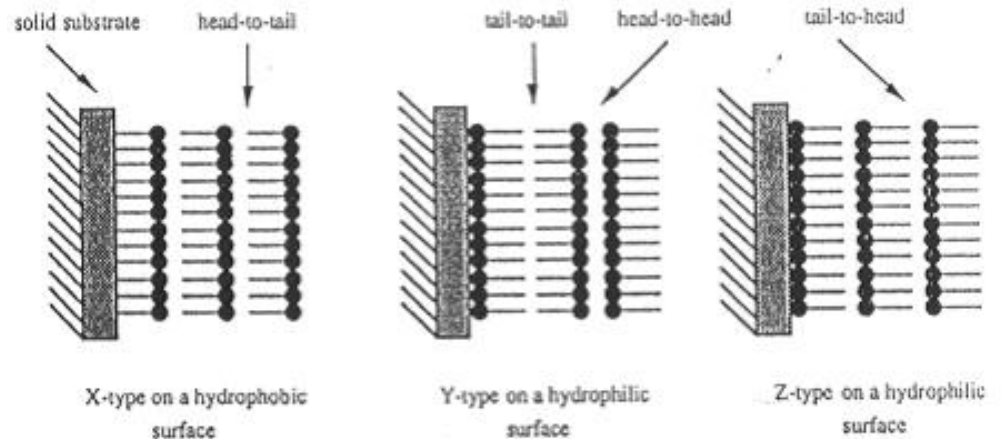
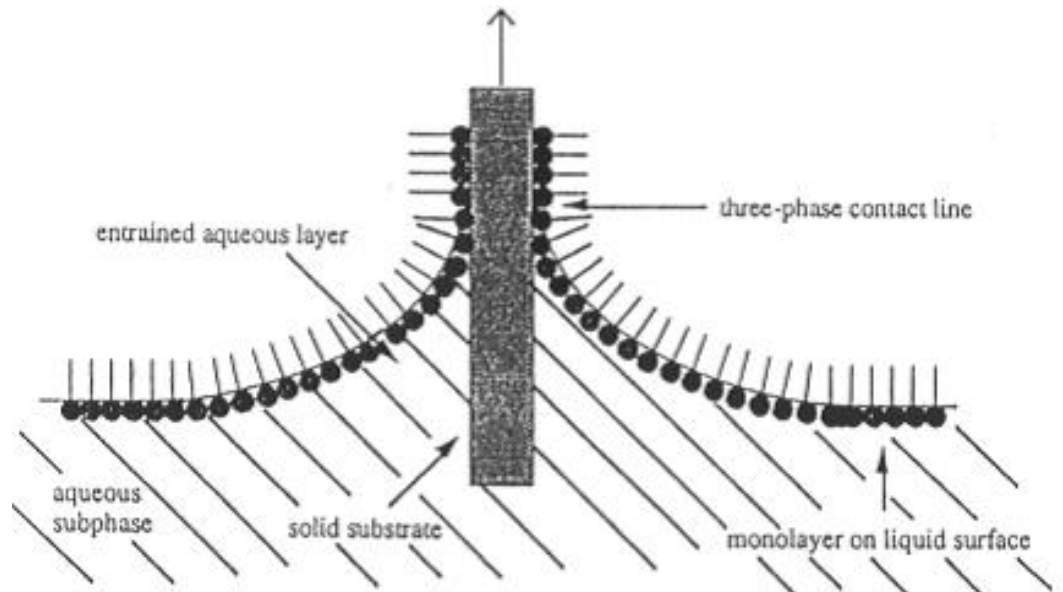
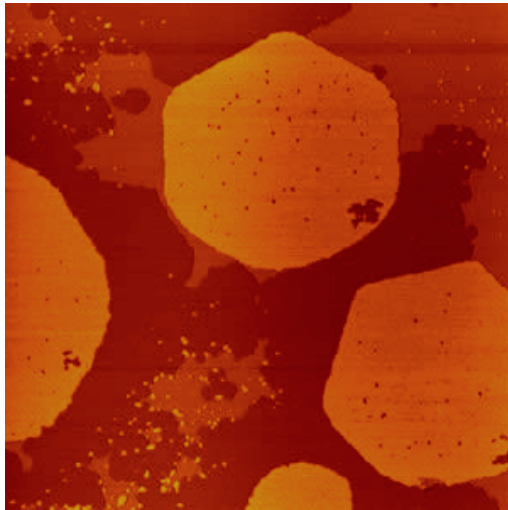
Two main mechanisms are shown here: **a**, coalescence sintering, and **b**, Ostwald ripening sintering. Coalescence sintering occurs when two clusters touch or collide and merge to form one bigger cluster. In contrast, Ostwald ripening sintering occurs by evaporation of atoms from one cluster, which then transfer to another. This is a dynamic process — both clusters exchange atoms, but the rate of loss from the smaller cluster is higher, because of the lower average coordination of atoms at the surface and their relative ease of removal. Thus big clusters get bigger at the expense of smaller clusters, which shrink and eventually disappear. The latter process is the usual form of sintering for metal clusters on a supported surface that are well spaced apart, although coalescence can occur for a high density of clusters. In general, the presence of the surface results in SMORS (surface-mediated Ostwald ripening sintering) in which material is transferred from one cluster to another by diffusion across the surface, and not through the gas phase.

Synthesis of Nanoparticles and Surface Modifications

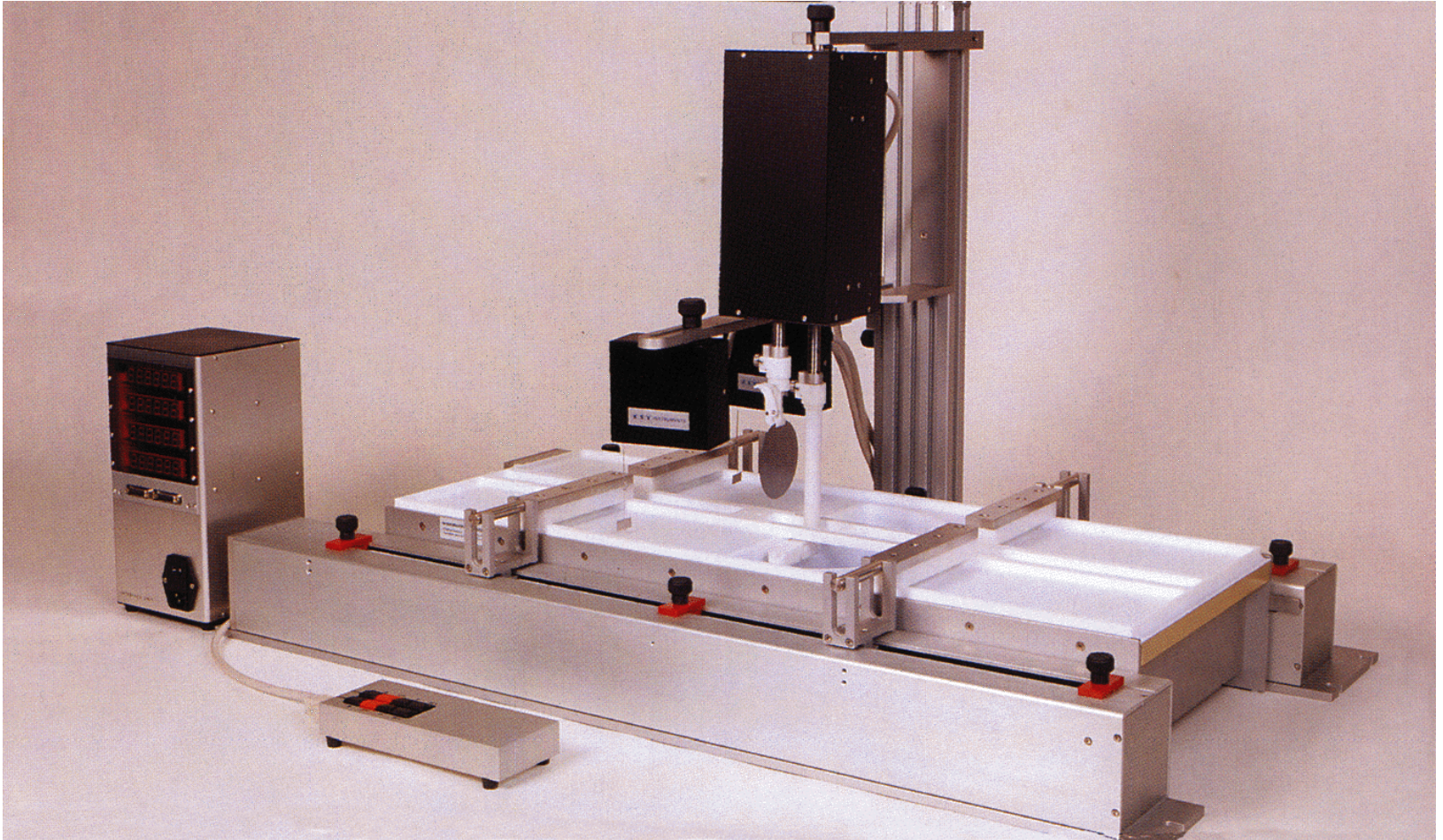
Self-Assembly

- Static assembly
- Dynamic assembly
 - $RT = 8.314 \text{ J/mol} \times 300 = 2.4 \text{ kJ/mol}$
- Driving forces
 - Chemisorption
 - Surface effect
 - Hydrophobic-hydrophilic
 - Intermolecular forces
 - Capillary force

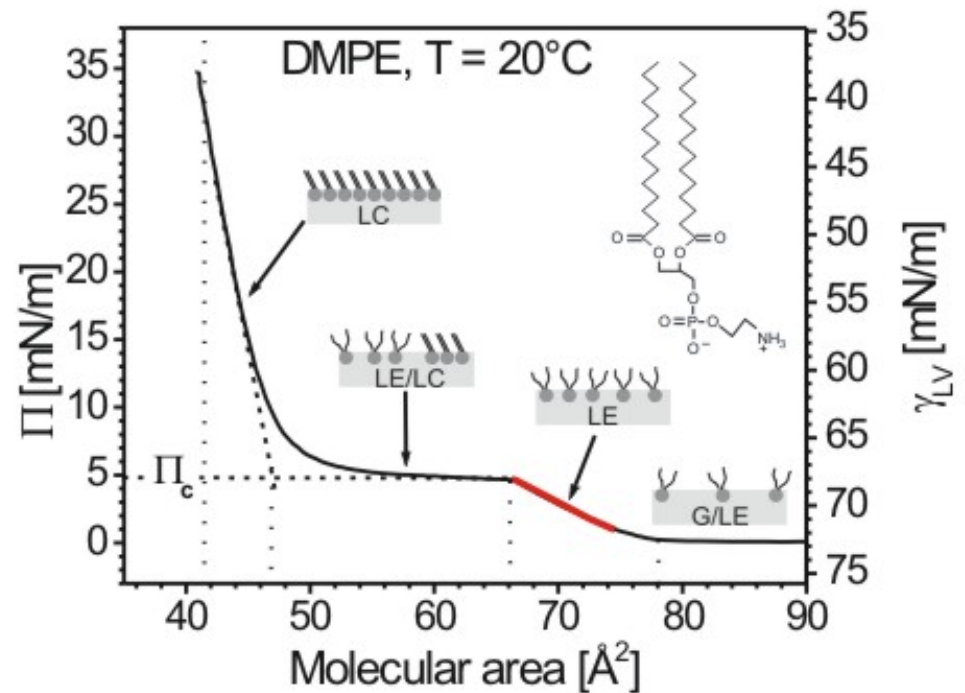
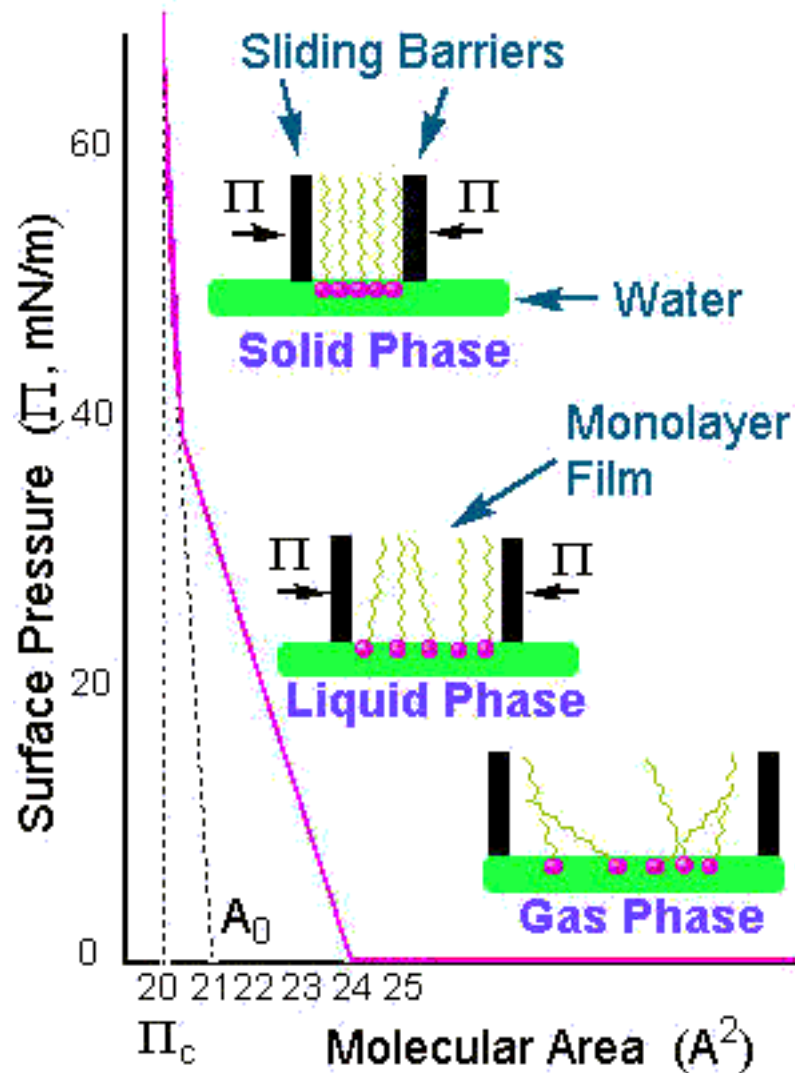
Langmuir-Blodgett Films



Langmuir-Blodgett Films

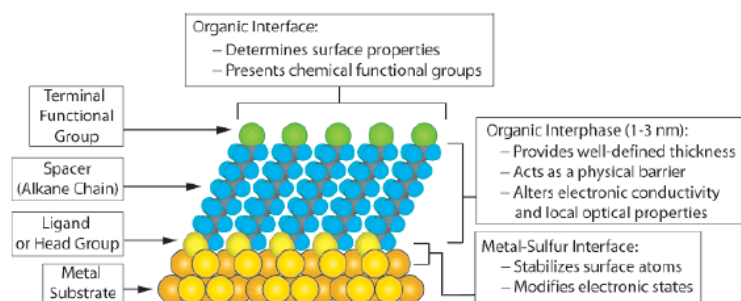


Isotherm



Self-Assemble Monolayer (SAM)

Chem. Rev. 2005, 105, 1103–1169



S-Au 25-30 Kcal/mole
Si-O 190 kcal/mole

Morphology of Substrate				Morphology of Substrate			
Ligand	Substrates	Thin Films or Bulk Material	Nanoparticles or Other Nanostructures	Ligand	Substrates	Thin Films or Bulk Material	Nanoparticles or Other Nanostructures
ROH	Fe ₃ O ₄	36	35	RSSR'	Ag	89	90
	Si-H	37			Au	20	90-92
	Si				CdS		61
RCOO-/RCOOH	α -Al ₂ O ₃	38,39			Pd	30	
	Fe ₃ O ₄		40		Au	93	
	Ni		41,42				
	Ti/TiO ₂	43		RCSSH	Au	94	
RCOO-OOCR	Si(111):H	44			CdSe		95
	Si(100):H			RS ₂ O ₃ Na ⁺	Au	96	98
Ene-diol	Fe ₃ O ₄		45		Cu	97	
RNH ₂	FeS ₂	46		RSeH	Ag	99	
	Mica	47			Au	100,101	
	Stainless Steel 316L	48			CdS		60
	YBa ₂ Cu ₃ O _{7-δ}	49			CdSe		102
	CdSe		50	RSeSeR'	Au	101	
RC \equiv N	Ag	51		R ₃ P	Au		103
	Au				FeS ₂		
R-N=N'(BF ₄)	GaAs(100)	52			CdS	46	104
	Pd	52			CdSe		104
	Si(111):H	52			CdTe		104
RSH	Ag	26	53,54		Co		105,106
	Ag ₉₀ Ni ₁₀	55		R ₃ P=O	CdS		104
	AgS		56		CdSe		104
	Au	26	57		CdTe		104
	AuAg		58				
	AuCu		58	RPO ₃ ²⁻ /RP(O)(OH) ₂	Al	107	
	Au ₈ Pd ₁₋₈		58		Al-OH	108	
	CdTe		59		Ca ₁₀ (PO ₄) ₆ (CO ₃) ₂ (OH) ₂	109	
	CdSe		60		GaAs	110	
	CdS		61,62		GaN	110	
	Cu	26	58		Indium tin oxide	111	
	FePt		63-66		(ITO)		
	GaAs	67			Mica	112	
	Ge	68			TiO ₂	113,114	
	Hg	69-71			ZrO ₂	114,115	
	HgTe		72		CdSe		116-118
	InP	73			CdTe		118,119
	Ir		74	RPO ₄ ³⁻	Al ₂ O ₃	120	
	Ni	75			Nb ₂ O ₅	120	
	PbS		76-78		Ta ₂ O ₅	121	
	Pd	30	74,79		TiO ₂	120,122	
	PdAg		58				
	Pt	32	80	RNaC	Pt	123	124
	Ru		81		Si	37	
	Stainless Steel 316L	48			Si(111):H	125	
	YBa ₂ Cu ₃ O _{7-δ}	82		RSiX ₃ X = H, Cl, OCH ₂ CH ₃	HfO ₂	126	
	Zn	83			ITO	127	
	ZnSe	84			PtO	128	
	ZnS		85		TiO ₂	113,126,129	
			87		ZrO ₂	126,129	
RSAc	Au	86					
	Au						
	Au						
RSR'	Au	88					

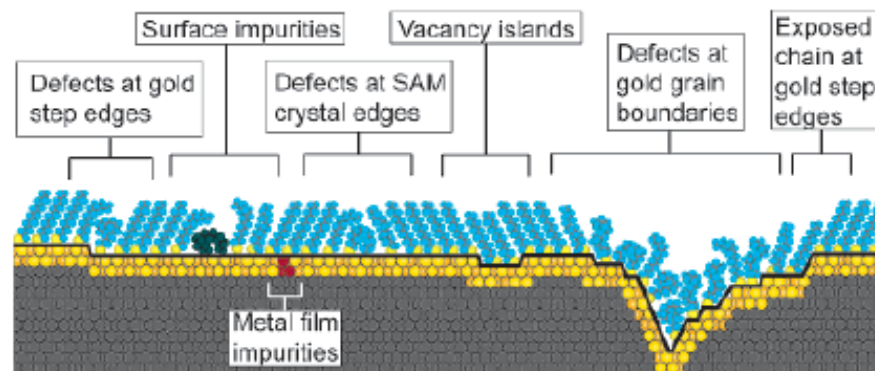
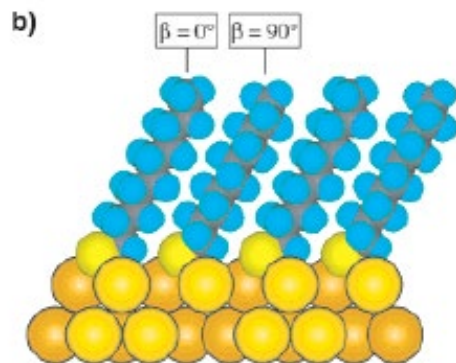
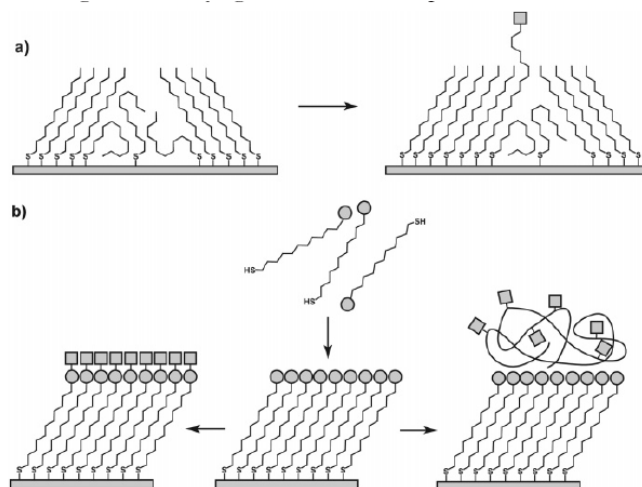
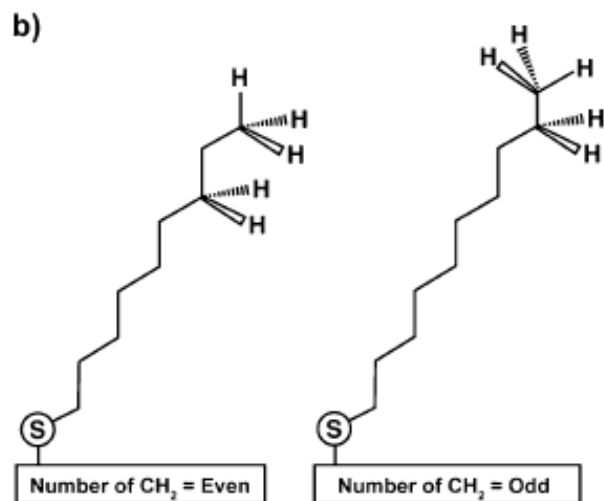


Figure 7. Schematic illustration of some of the intrinsic and extrinsic defects found in SAMs formed on polycrystalline substrates. The dark line at the metal–sulfur interface is a visual guide for the reader and indicates the changing topography of the substrate itself.



^a (a) Insertion of a functional adsorbate at a defect site in a preformed SAM. (b) Transformation of a SAM with exposed functional groups (circles) by either chemical reaction or adsorption of another material.

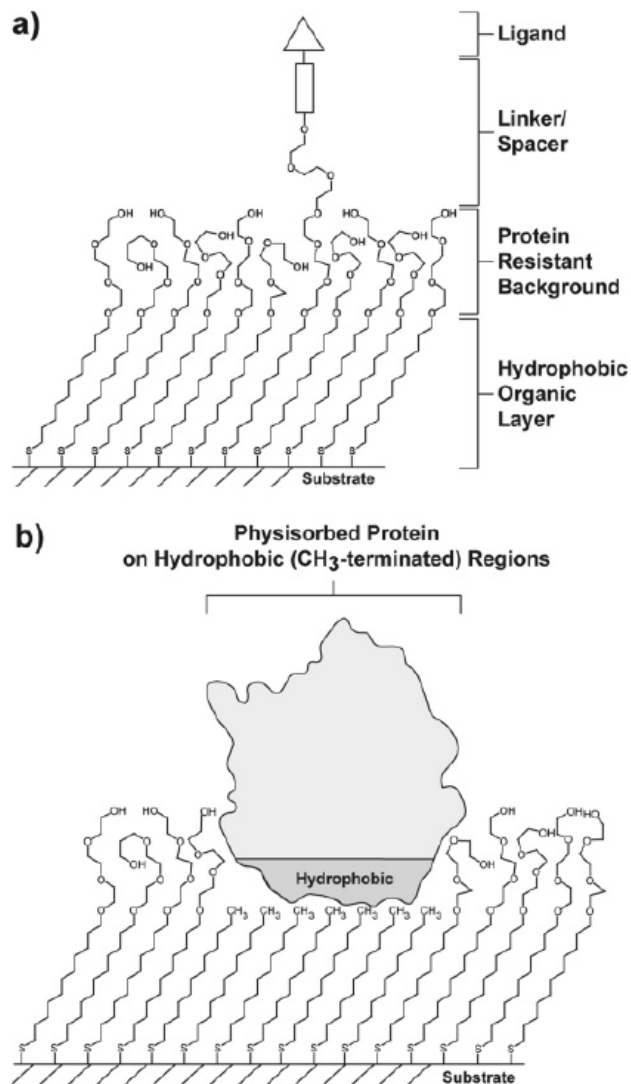


Figure 21. Schematic illustrations of (a) a mixed SAM and (b) a patterned SAM. Both types are used for applications in biology and biochemistry.

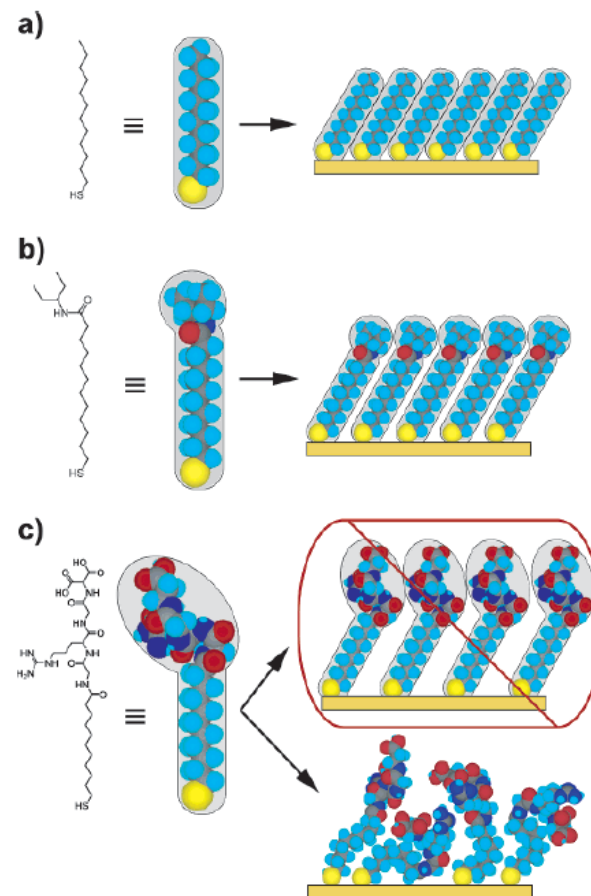


Figure 22. Schematic diagram illustrating the effects that large terminal groups have on the packing density and organization of SAMs. (a) Small terminal groups such as $-\text{CH}_3$, $-\text{CN}$, etc., do not distort the secondary organization of the organic layer and have no effect on the sulfur arrangement. (b) Slightly larger groups (like the branched amide shown here) begin to distort the organization of the organic layer, but the strongly favorable energetics of metal-sulfur binding drive a highly dense arrangement of adsorbates. (c) Large terminal groups (peptides, proteins, antibodies) sterically are unable to adopt a secondary organization similar to that for alkanethiols with small terminal groups. The resulting structures probably are more disordered and less dense than those formed with the types of molecules in a and b.

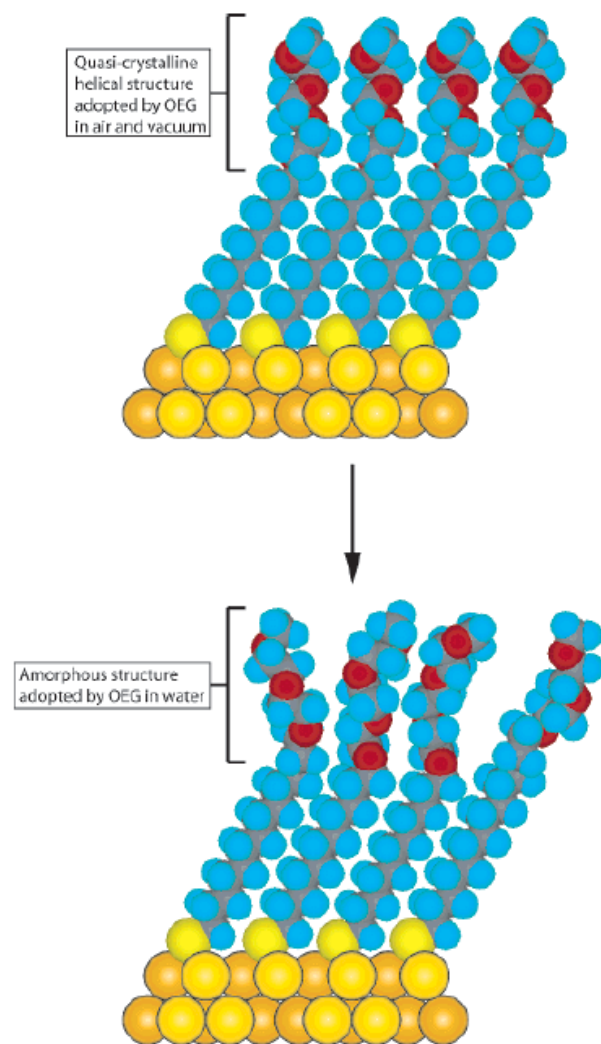
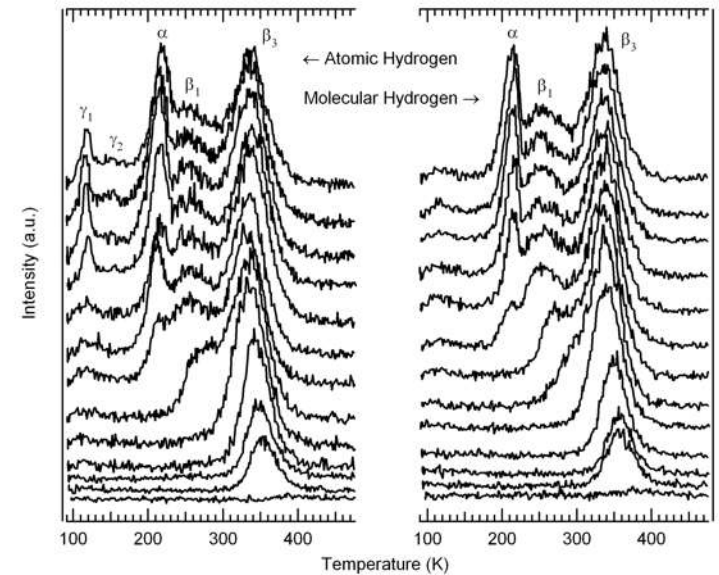


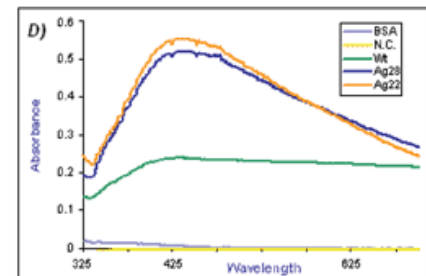
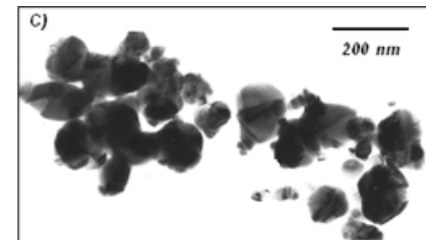
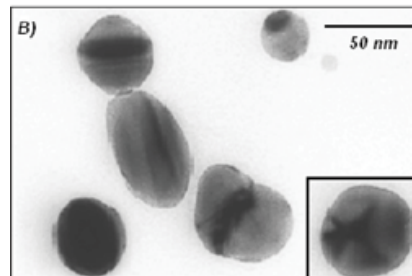
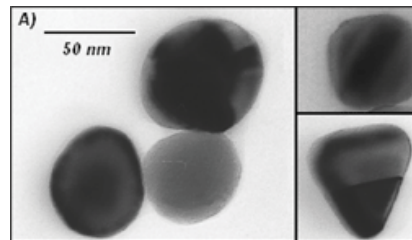
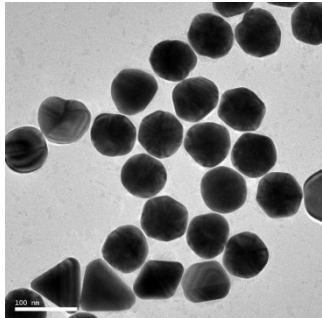
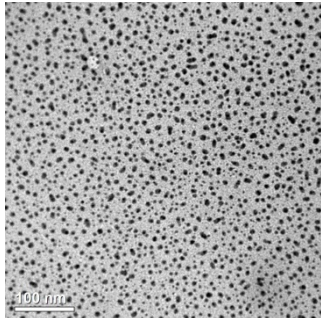
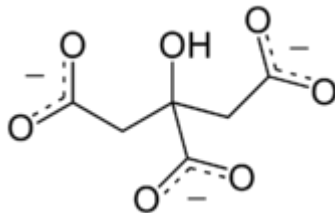
Figure 23. Schematic illustration of the order–disorder transition evidenced by SAMs of alkanethiolates terminated with triethylene glycol. The EG_3 group loses conformational ordering upon solvation in water.

Temperature Programmed Desorption



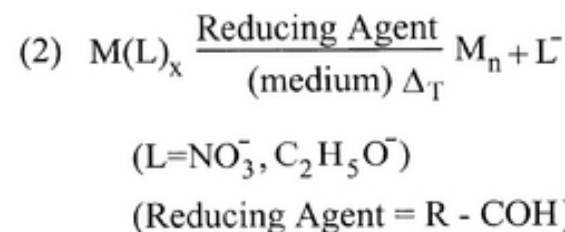
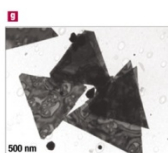
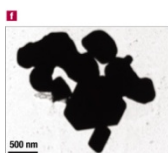
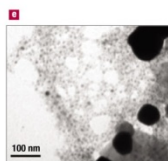
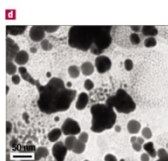
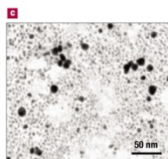
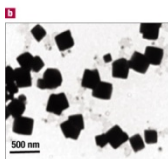
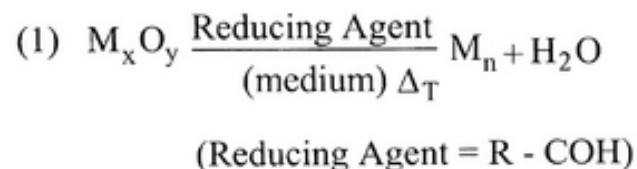
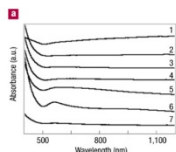
Synthesis of Silver Nanoparticles

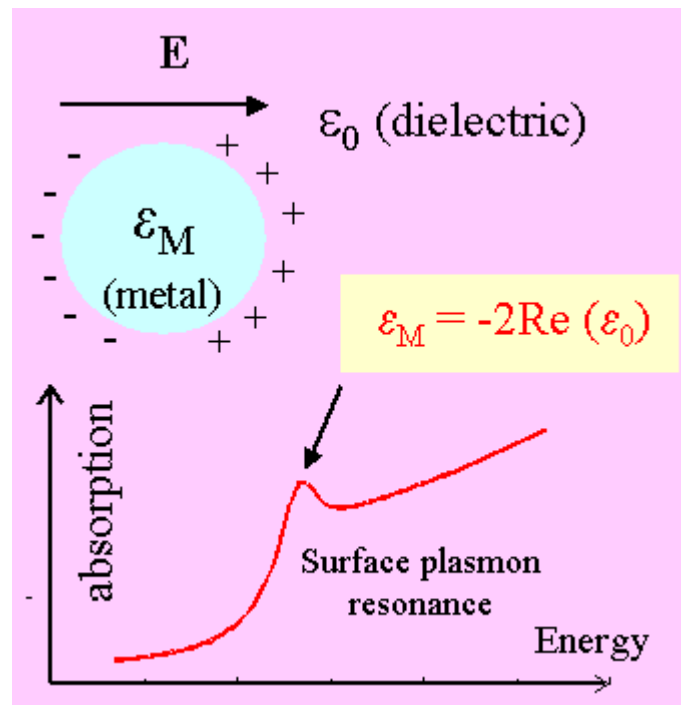
1. A solution of AgNO_3 ($1.0 \times 10^{-3} \text{ M}$) in deionized water was heated until it began to boil.
2. Sodium citrate solution was added dropwise to the silver nitrate solution as soon as the boiling commenced. The color of the solution slowly turned into grayish yellow, indicating the reduction of the Ag^+ ions.
3. Heating was continued for an additional 15 min, and then the solution was cooled to room temperature before employing for further experimentation.



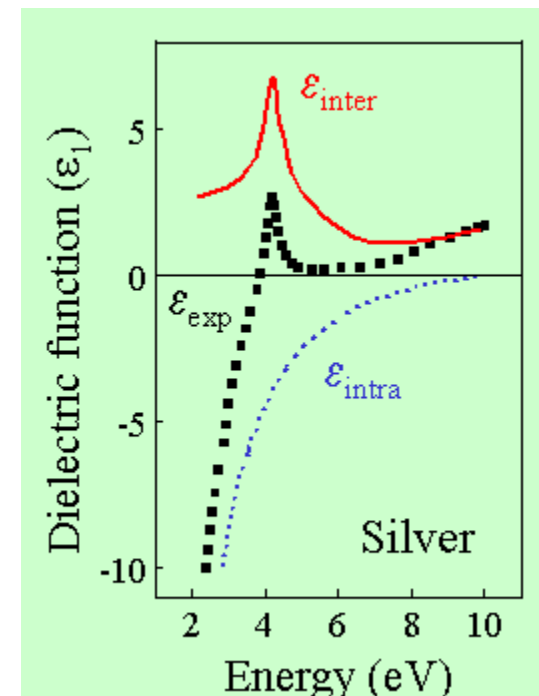
Synthesis of Gold Nanoparticles

1. Add 20 mL of 1.0 mM HAuCl_4 to a 50 mL round bottom flask on a stirring hot plate.
2. Add a magnetic stir bar and bring the solution to a boil.
3. To the boiling solution, add 2 mL of a 1% solution of trisodium citrate dihydrate
4. The gold sol gradually forms as the citrate reduces the gold(III). Stop heating when a deep red color is obtained.



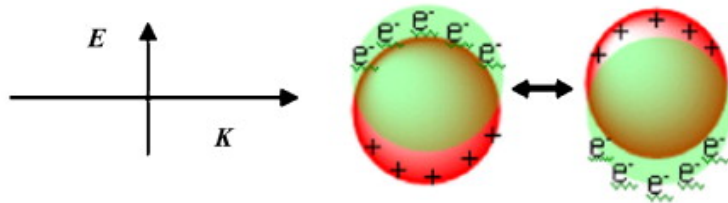


$$\epsilon_{eff} = \epsilon_0 + 3N\epsilon_0 \frac{\epsilon_M - \epsilon_0}{\epsilon_M + 2\epsilon_0}$$

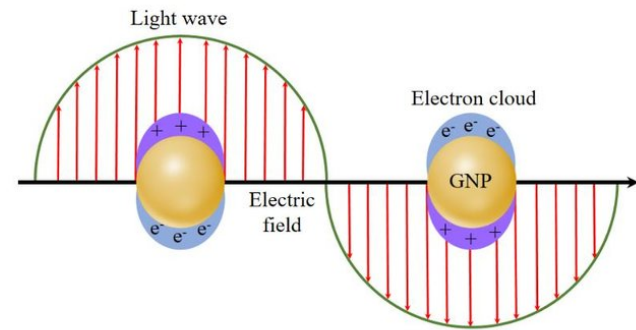
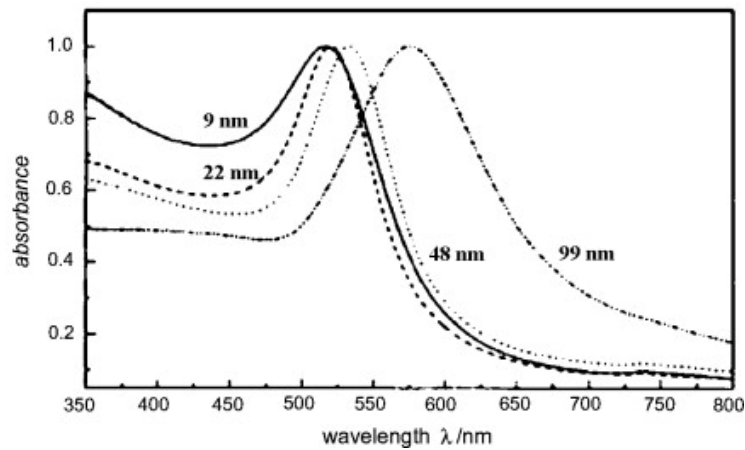


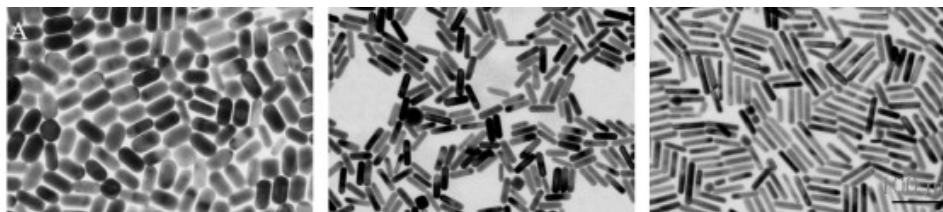
Localized Surface Plasmon

A

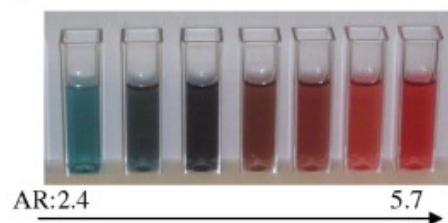


B

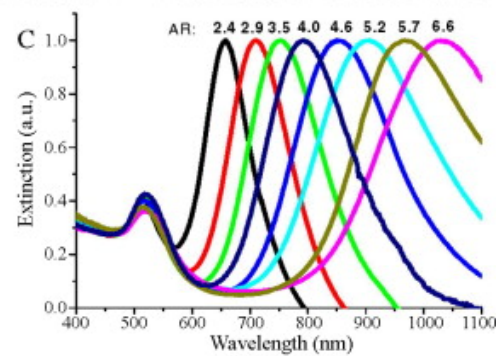




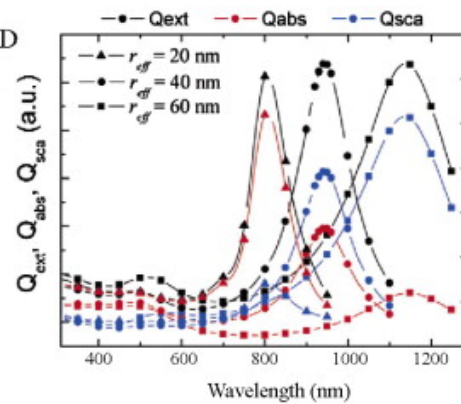
B



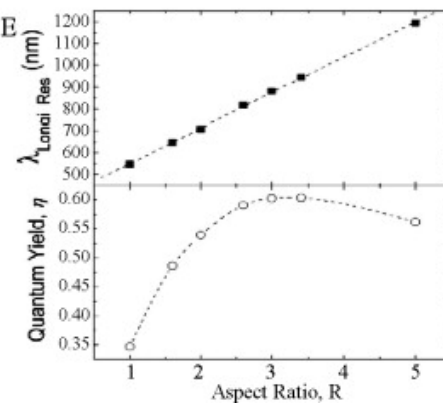
C



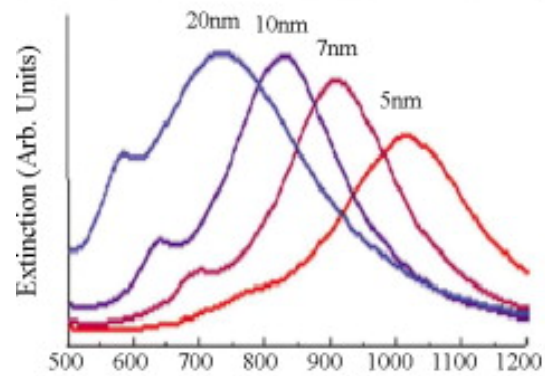
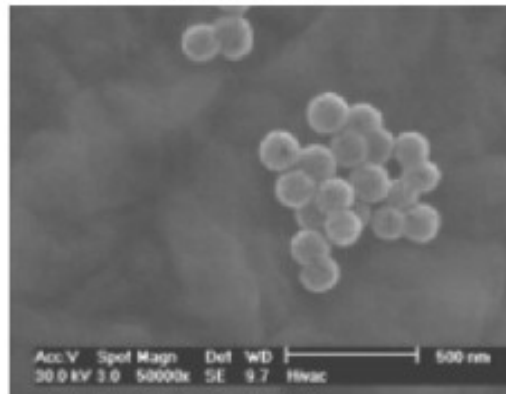
D



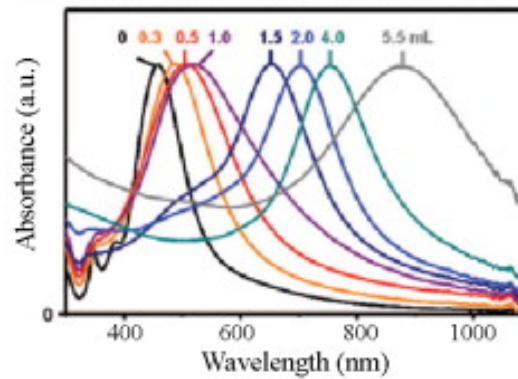
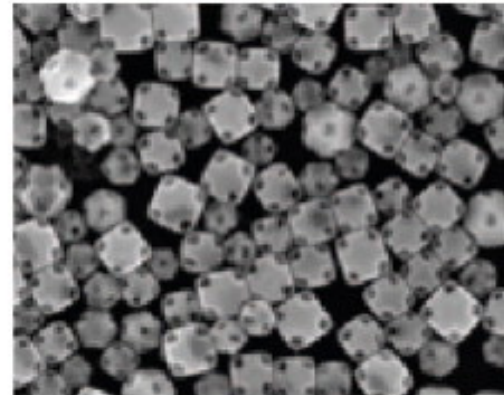
E



A. gold nanoshell

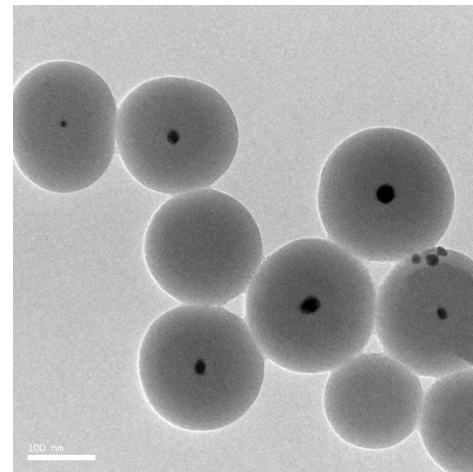
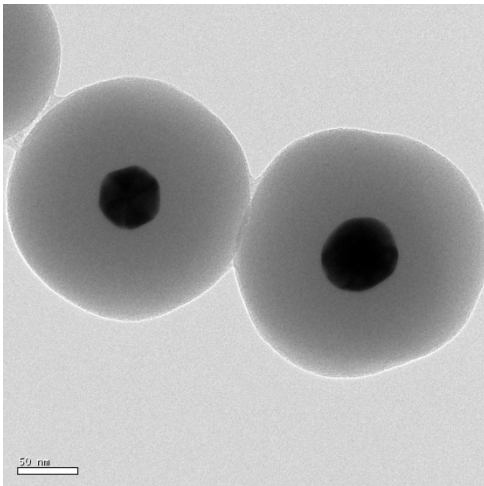


B. gold nanocage

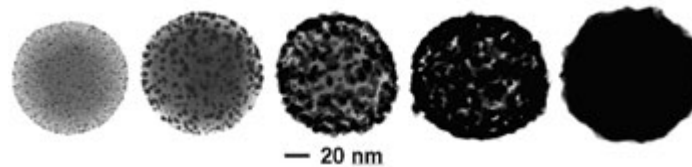
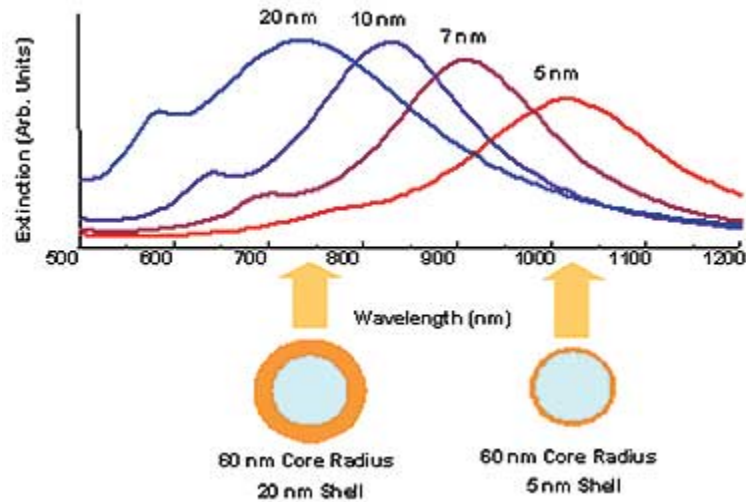


Construction of Core Shell Ag/Au@SiO₂ Nanoparticles

1. Under vigorous stirring, 1 ml of the silver/ gold colloids solution was mixed with 250 mL of isopropanol and 25 mL of deionized water.
2. Immediately after the addition of 4 mL of 30% ammonium hydroxide, different amounts of tetraethoxysilane (TEOS) were added to the reaction mixture.
3. To obtain different silica layer thicknesses, TEOS solutions with a concentration between 50% and 100% was added to the suspension. The reaction was stirred at room temperature for 30 minutes and then was allowed to age without agitation at 4 °C overnight.
4. Each suspension of silica-coated silver/gold nanoparticles was washed and centrifuged, followed by re-suspension in water. The thickness of the silica layers was determined from TEM images .



Core-Shell Nanoparticles



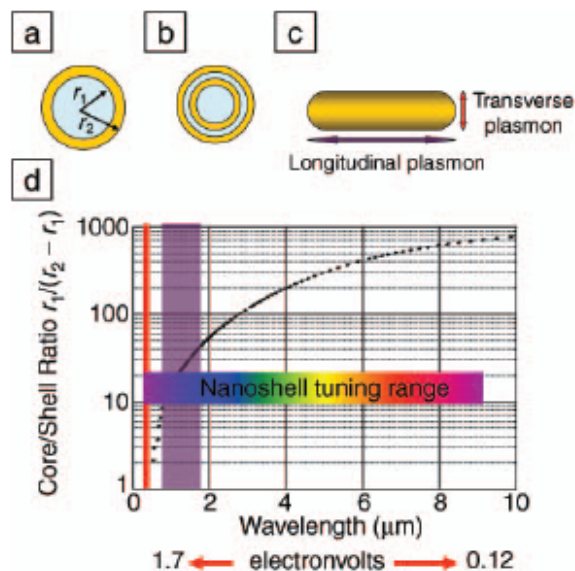


Figure 1. (a) Schematic illustration of a silica-core, gold-shell nanoshell, indicating inner (r_1) and outer (r_2) radii of the shell layers. (b) Depiction of a four-layer, concentric nanoshell. (c) Schematic illustration of a metallic nanorod. (d) Plot of nanoshell resonance as a function of core and shell dimensions, overlaid with reported spectral ranges of nanorod resonances (red, transverse plasmon; purple, longitudinal plasmon), and reported nanoshell and concentric nanoshell combined spectral range of plasmon response.

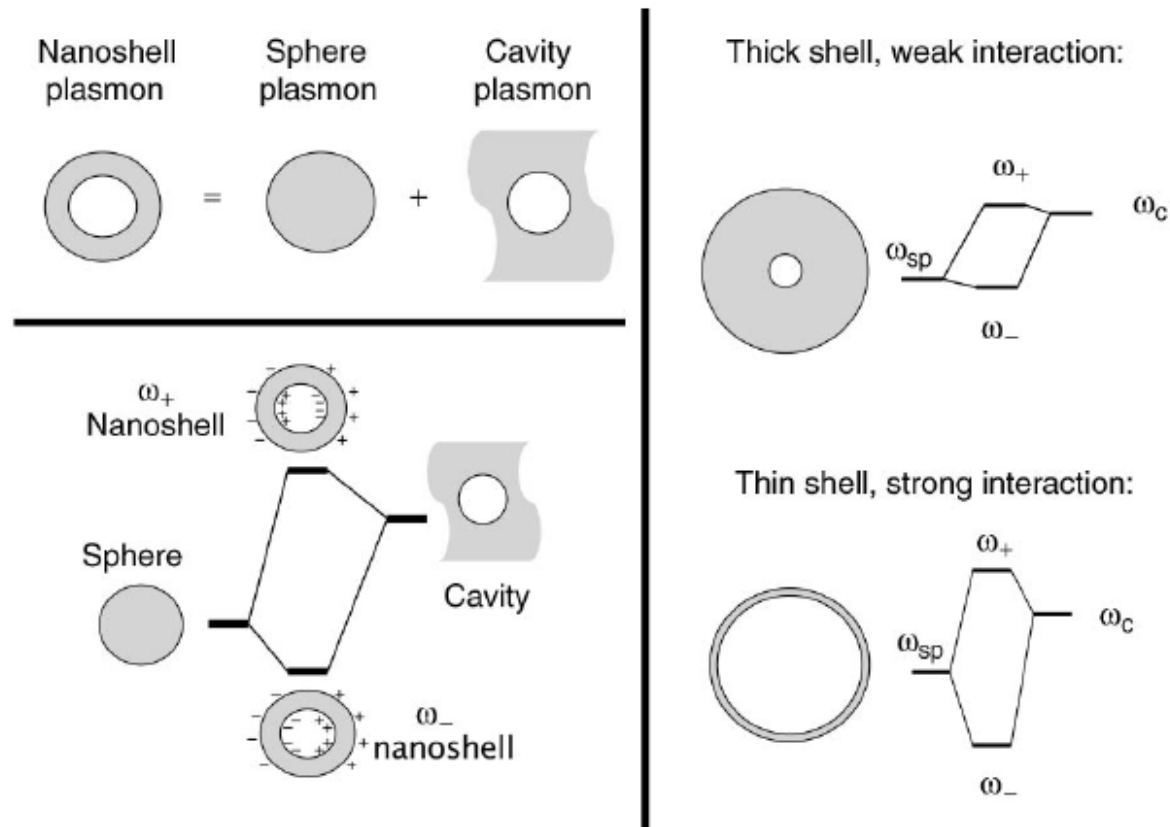


Figure 2. Plasmon hybridization and the sphere-cavity model for nanoshells: the interaction between a sphere (resonance frequency, ω_{sp}) and a cavity plasmon (resonance frequency, ω_c) is tuned by varying the thickness of the shell layer of the nanoparticle. Two hybrid plasmon resonances, the ω_- “bright,” or “bonding,” plasmon and the ω_+ “dark,” or “anti-bonding,” plasmon resonances are formed. The lower-energy plasmon couples most strongly to the optical field.

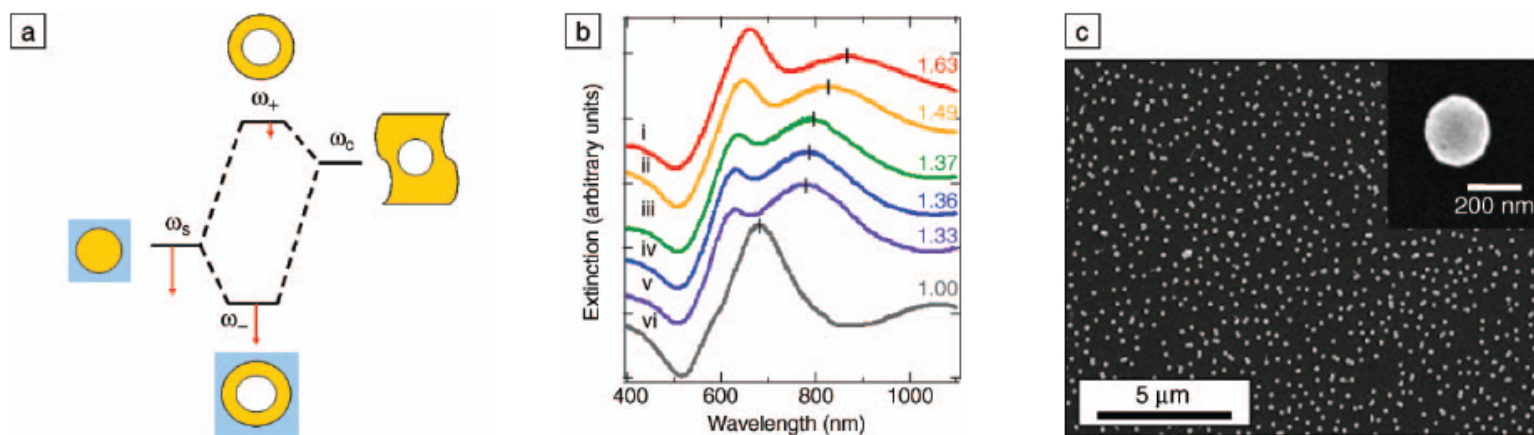


Figure 5. (a) Plasmon hybridization picture applied to surface plasmon resonance sensing with nanoshells: the low-energy “bonding” plasmon, ω_- , is sensitized to changes in its dielectric environment. The blue background schematically denotes the embedding medium for the nanoparticle. (b) Experimental curves showing plasmon resonance shifts for nanoshell-coated films in various media: (i) carbon disulfide, (ii) toluene, (iii) hexane, (iv) ethanol, (v) H_2O , and (vi) air. The index of refraction for each embedding medium is noted on the far right of the spectra. Spectra are offset for clarity. (c) Scanning electron micrograph of nanoshells deposited onto a poly(vinyl pyridine) functionalized glass surface, as used to acquire data in (b). Inset: individual nanoshell.

Preparation of $\text{Fe}_3\text{O}_4@\text{Ag}/\text{Au}$

1. *To the magnetic nanoparticle suspension obtained from commercial company, add 50 ml of a solution of Au (III) salt or Ag (I) salt at concentration of 0.01–1% mmol/L , shaking for 30 minutes, allowing Au (III) or Ag (I) ion to absorb on the surface of magnetic nanoparticle sufficiently,*
2. *Then adding 15–40 ml of reducing agent, such as hydroxylamine hydrochloride at concentration of 40 mmol/L, reacting for 5–40 minutes.*
3. *Further adding 1–10 ml of a solution of Au (III) salt or Ag (I) salt at concentration of 0.01–1%, shaking for 10 minutes, coating a reduced layer of gold or silver on the surface of the magnetic nanoparticle, forming super-paramagnetic composite particles having core/shell structure, separating magnetically, washing repeatedly with distilled water.*

Synthesis of Quantum Dots

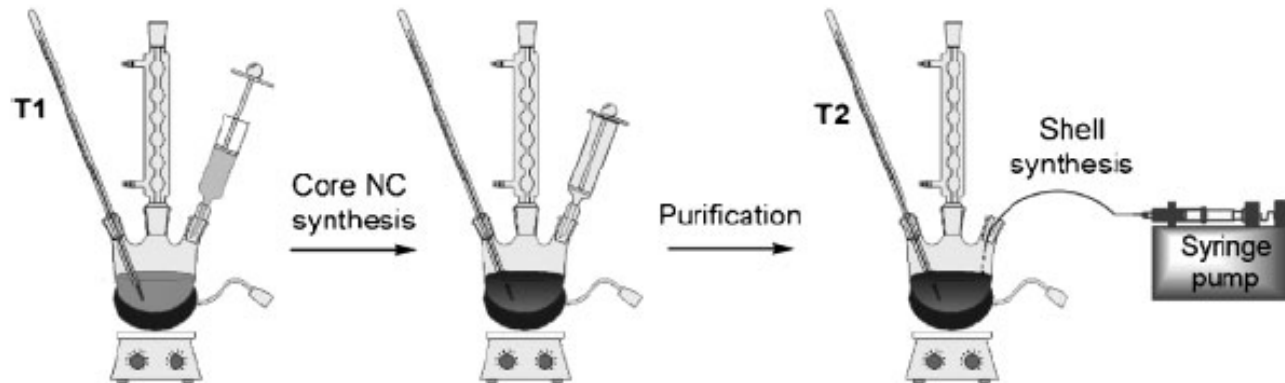
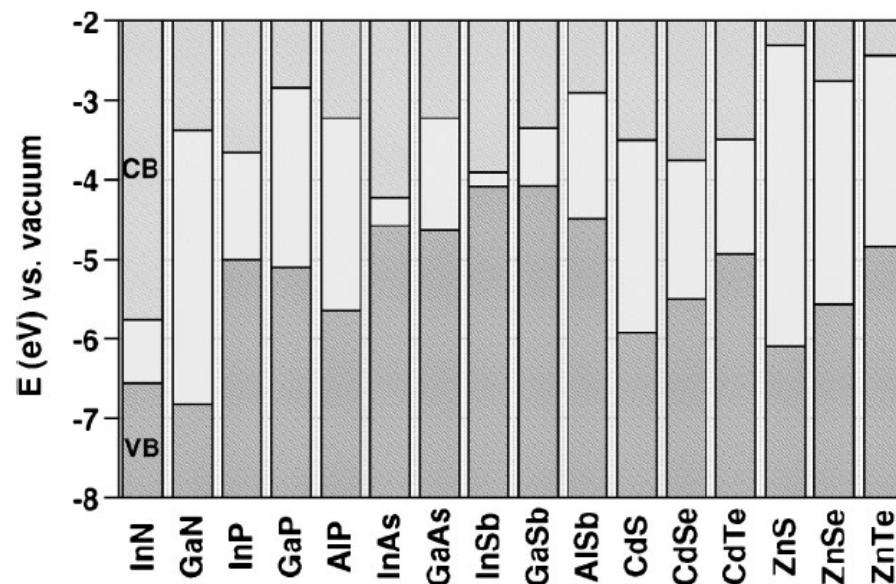


Figure 2. Two-step synthesis of core/shell nanocrystals.



Scheme 1. Electronic energy levels of selected III–V and II–VI semiconductors using the valence-band offsets from Reference [12] (VB: valence band, CB: conduction band).

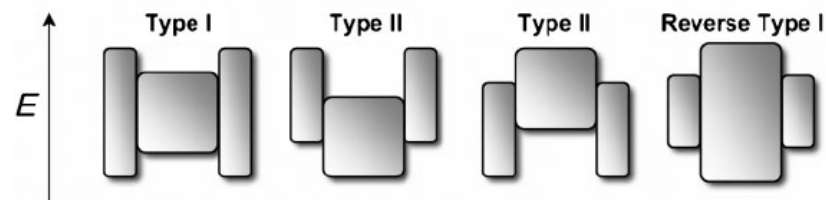
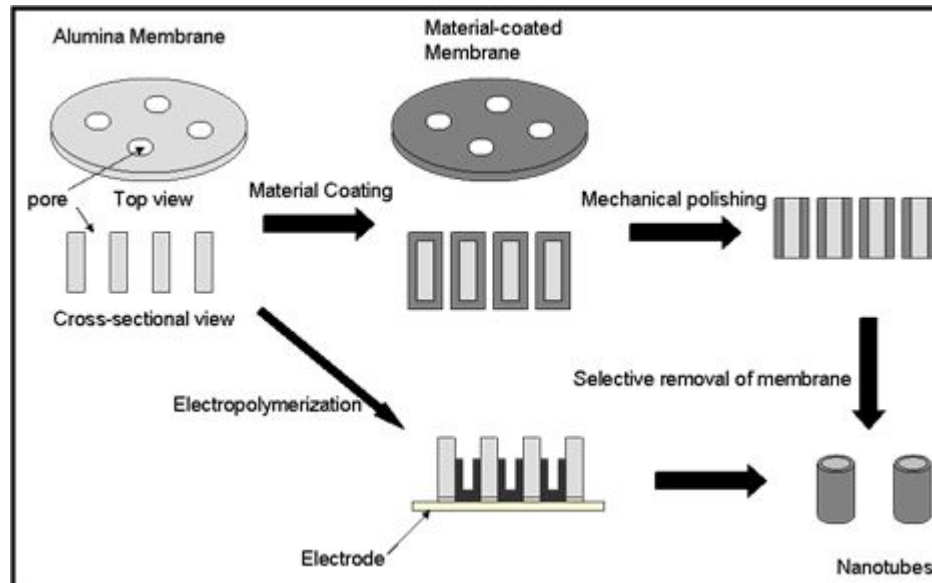


Figure 1. Schematic representation of the energy-level alignment in different core/shell systems realized with semiconductor NCs to date. The upper and lower edges of the rectangles correspond to the positions of the conduction- and valence-band edge of the core (center) and shell materials, respectively.

Parameter	Type I	Inverse Type I	Type II	Inverse Type II
Band gap	The band gap of the core is smaller than the band gap of the shell, as well as the band gap of the core falls within the band gap of the shell [18–20]	The band gap of the core is greater than the band gap of the shell, as well as the band gap of the shell falls within band gap of the core [21]	Valence band edge of the core is within the band gap of the shell or conduction band edge of the shell is within the band gap of the core [22,23]	Conduction band edge of the core is within the band gap of the shell or valence band edge of the shell is within the band gap of the core [24]
Excited electrons/holes positions	Excited electrons and holes are completely confined in the core region [25]	The excited electrons and holes are completely or partially confined in the shell based on the thickness of the shell.	One charge carrier either excited electron or hole is confined to the core, while the other is mostly confined to the shell	One of the excited electrons or the holes are delocalized in the core/shell structure, and the other one is confined within the core.
Quantum yield (QY)	Higher QY and long-term stability [25,26]	Lower QY and poor stability	Lower QY and poor stability [27]	Relatively higher QY and fair stability
Stokes shift	Small	Significantly large [21]	Large [28]	Large and tunable via controlling the size of the core and thickness of the shell
Average absorption range	(400–500) nm [29]	(400–500) nm [30,31]	(600–800) nm [23,32]	(300–1600) nm [33]
Average emission range	(430–600) nm [34]	(400–700) nm [34]	(700–1000) nm [34]	(700–1000) nm [34]
Limitations	The shell can trap charge carriers which leads to reduced fluorescence QY	Both the excited electrons and holes may leak to the surface	One of the excited electrons or hole leak to the surface	The excited electron or hole can be absorbed leading to reduced excited decay time one carrier is mostly confined to the core, while the other is mostly confined to the shell
Construct/materials	<ul style="list-style-type: none"> • CdSe/ZnS • CdSe/CdS • CdS/ZnS 	<ul style="list-style-type: none"> • CdS/HgS • CdS/CdSe • ZnSe/CdSe 	<ul style="list-style-type: none"> • CdTe/CdSe • CdSe/ZnTe • CdSe/ZnSe 	<ul style="list-style-type: none"> • InP/CdS • PbS/CdS

Template Synthesis



Porous Materials

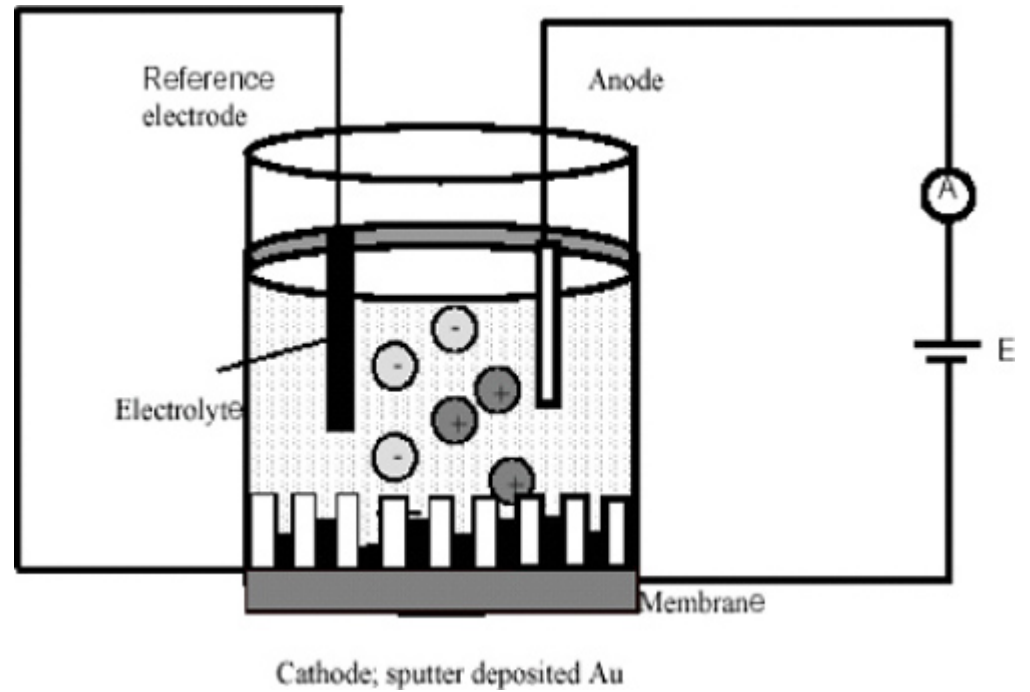
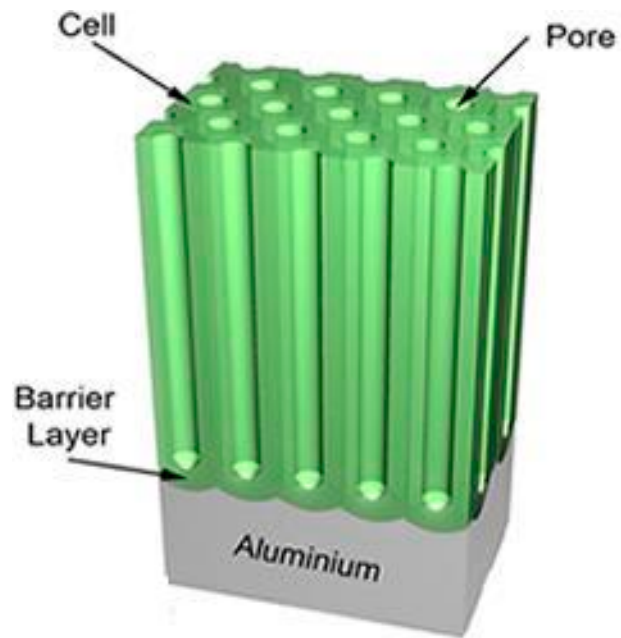
- AAO
- MCM-41

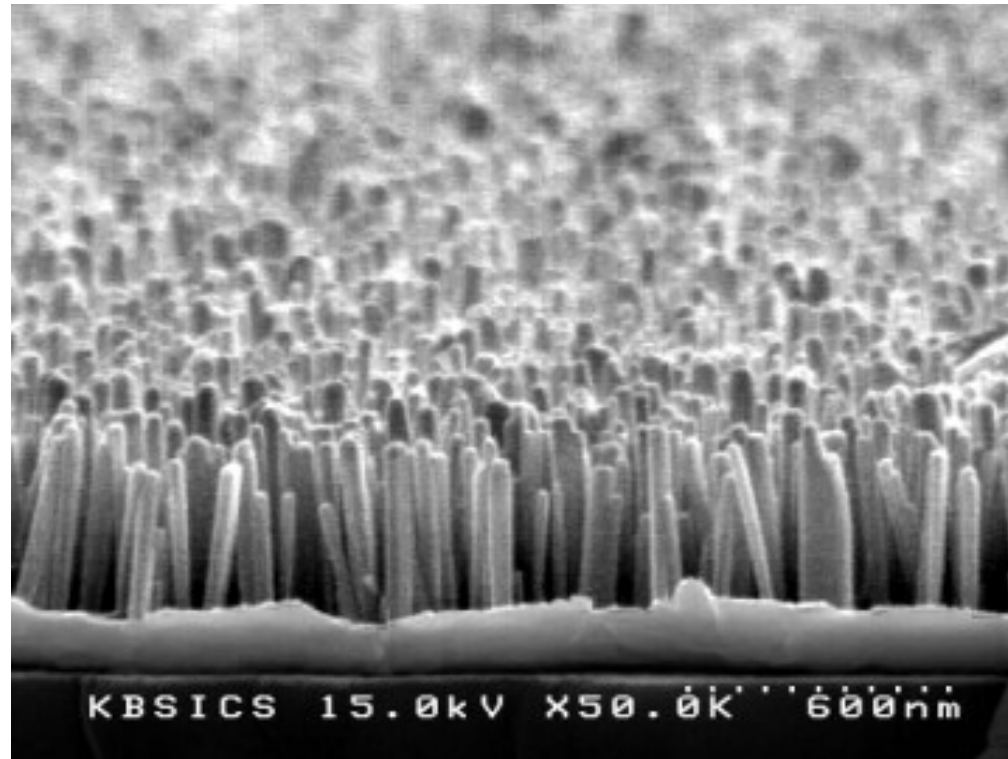
Mobil Crystalline Materials, or MCM-41

Santa Barbara Amorphous type material, or SBA-15

- Micro: $< 2\text{nm}$
- Meso:
- Macro: $> 50\text{nm}$

AAO





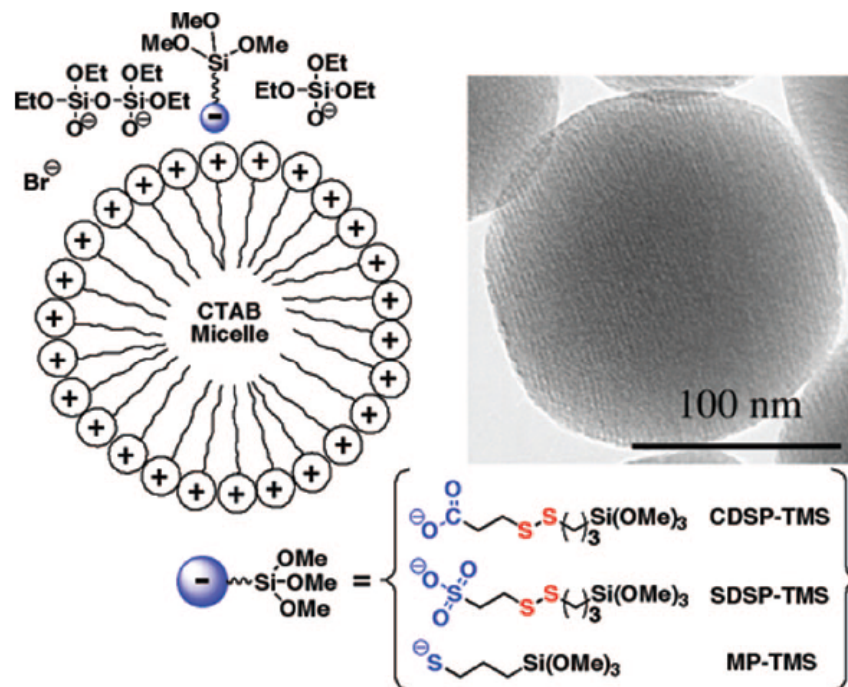


FIGURE 3. Schematic representation of the use of anionic organoalkoxysilanes for controlling the functionalization of the MSN materials. The MCM-41-type mesoporous channels are illustrated by the parallel stripes shown in the transmission electron microscopy (TEM) micrograph of the MSN-SH material. Reproduced with permission from ref 15. Copyright 2005, Royal Society of Chemistry.

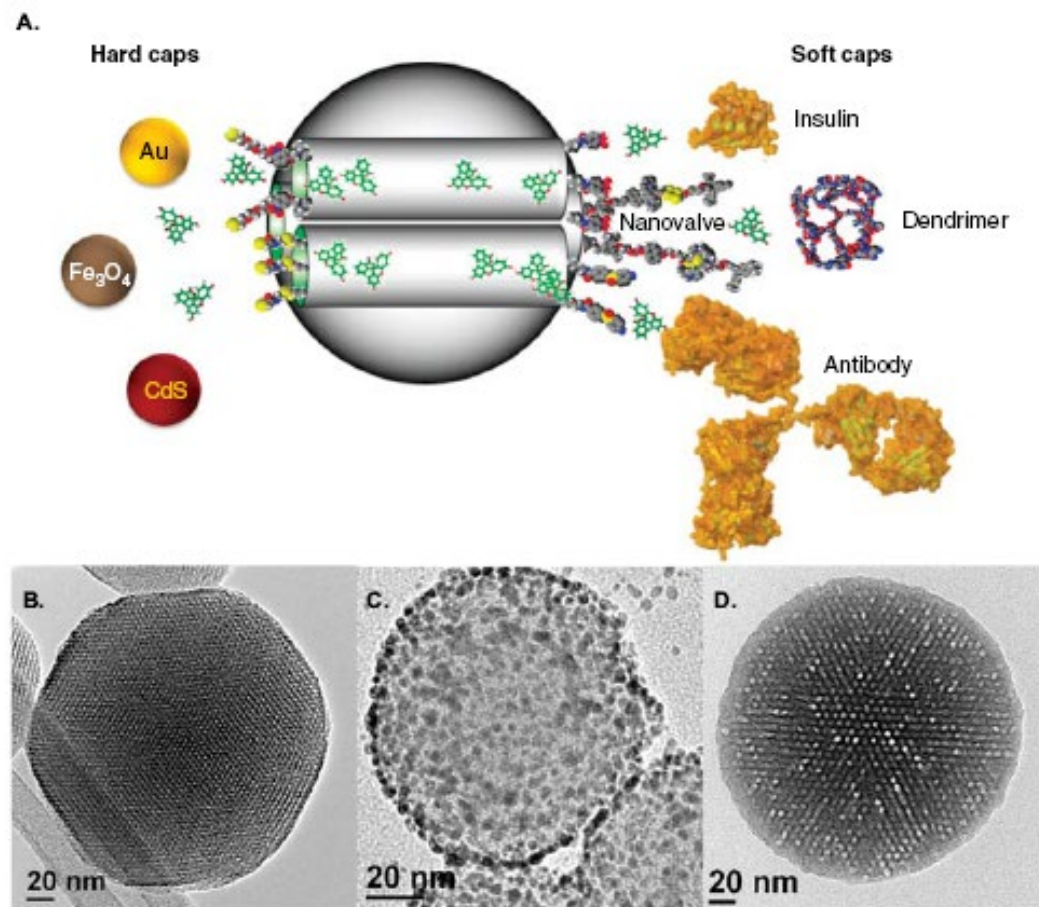


Figure 1. A. Schematic representation of a MSN loaded with drugs and capped with hard caps and soft caps highlighted in this review. Transmission electron microscopy images of (B) a MSN along the axis of the mesopores, (C) capped with hard (Au NP) and (D) with soft (polymer) caps.

MSN: Mesoporous silica nanoparticle.

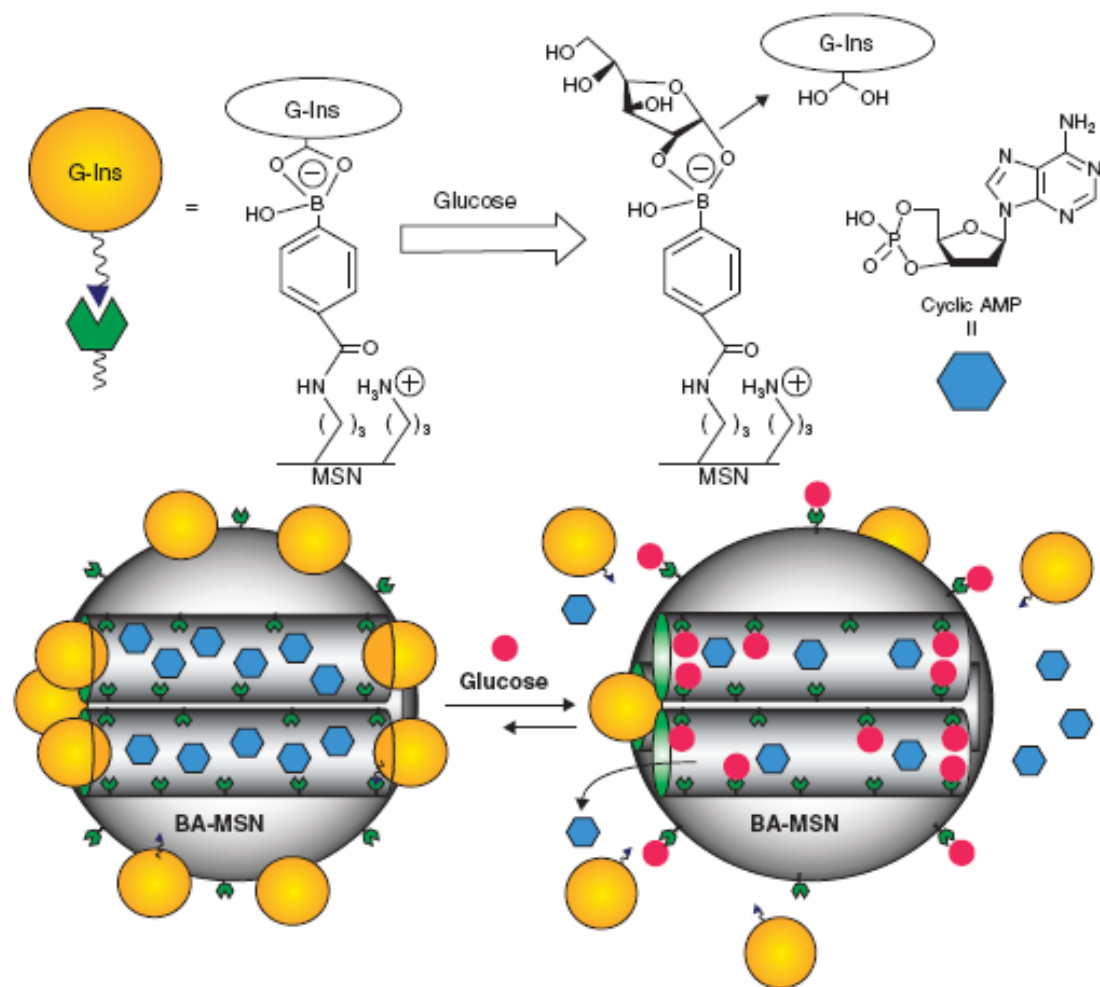
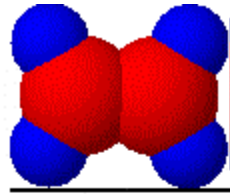


Figure 5. Schematic representation of the glucose-responsive MSN-based double delivery system for controlled release of bioactive G-Ins and cyclic AMP. The controlled release mechanism was achieved by means of the displacement reaction between blood glucose and G-Ins based on reversible boronic acid-diol complexation. High glucose concentration triggers the G-Ins uncapping and the release of cyclic AMP sequentially to diminish the higher than normal level of blood glucose.

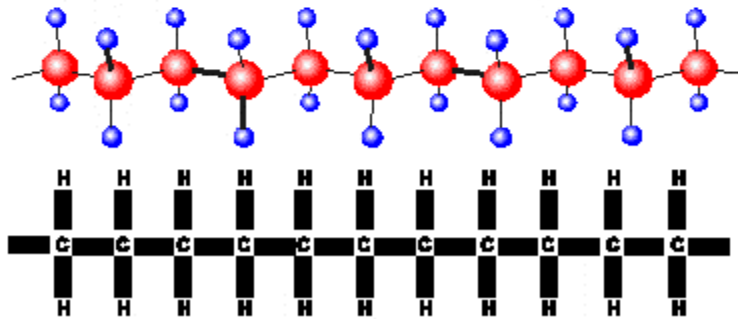
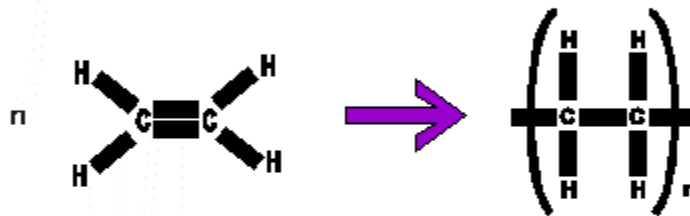
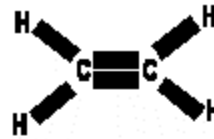
Reproduced with permission from [19].

G-Ins: G-insulin; MSN: Mesoporous silica nanoparticle.

Polymer



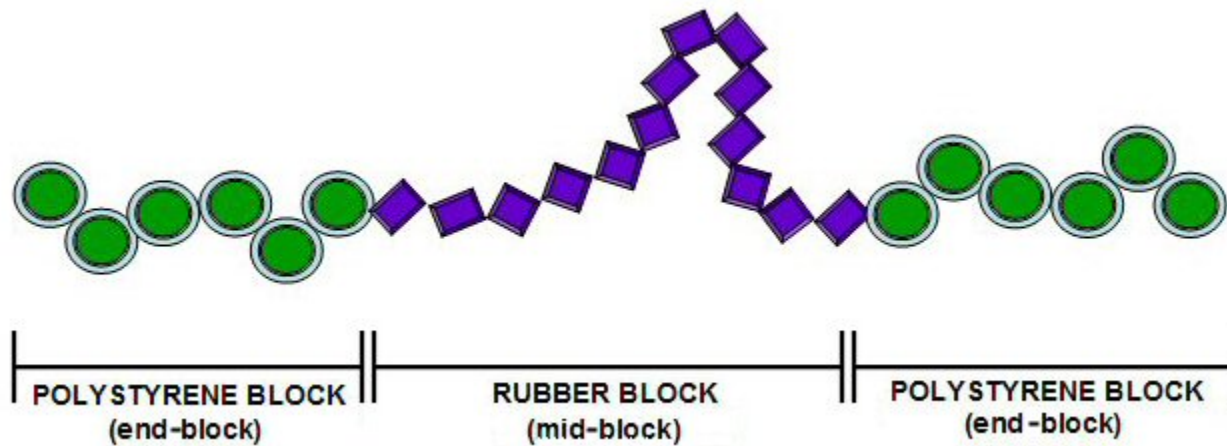
a monomer ethene



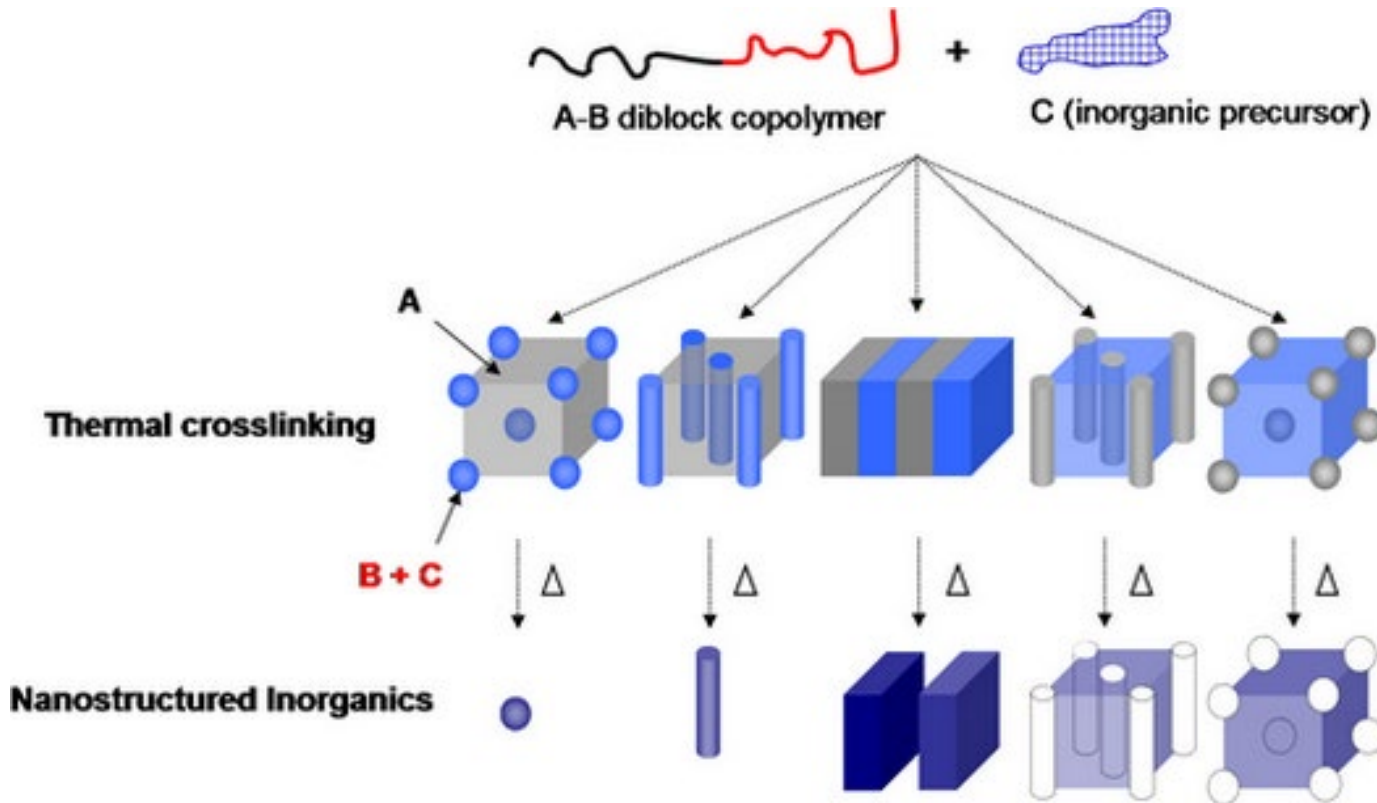
a polymer

poly(ethene)

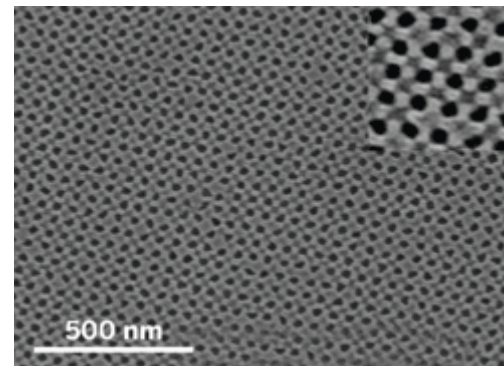
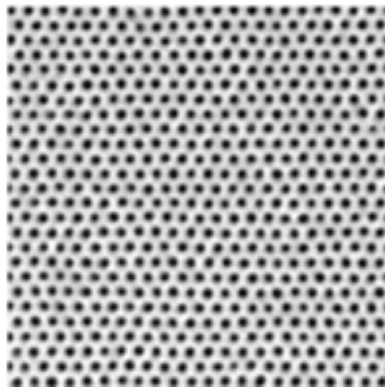
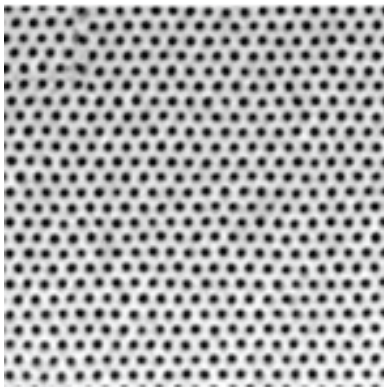
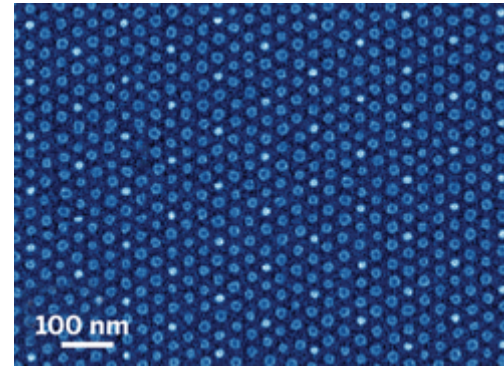
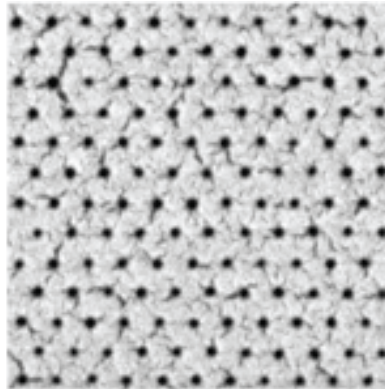
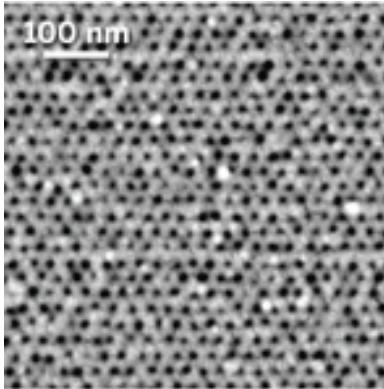
Block copolymer



Phase Segregation



Self-Assembled Block-copolymer



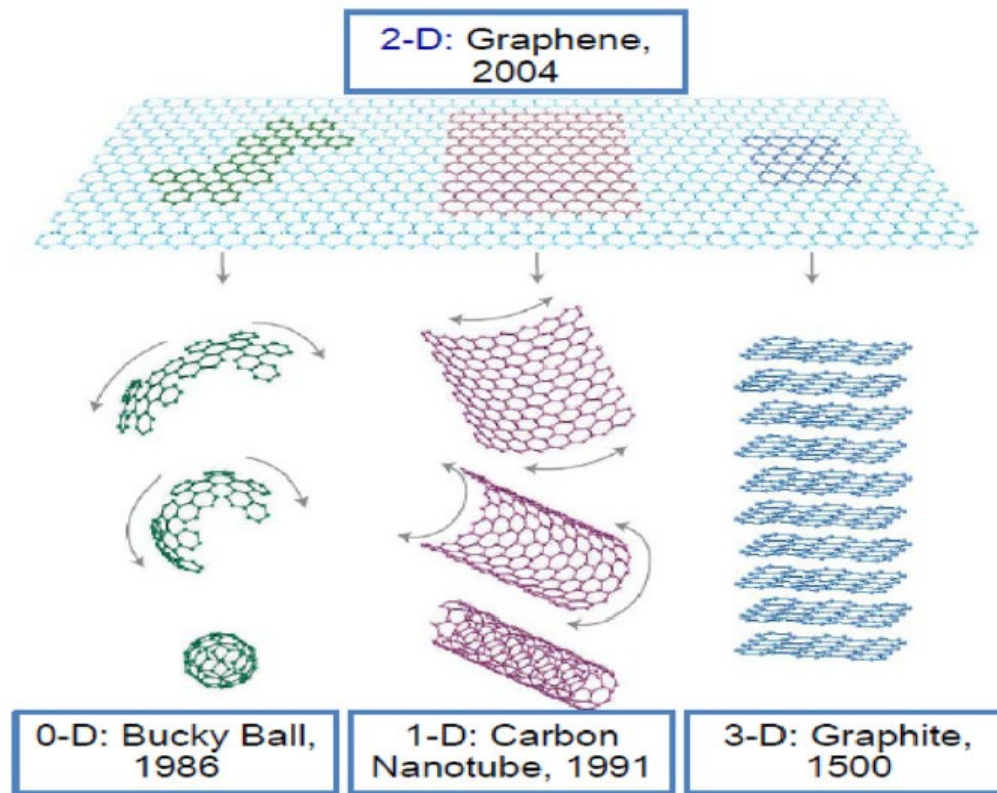


Fig. 1 Mother of all graphene forms. Graphene is a 2D building material for carbon material of all other dimensionalities. It can be wrapped up into 0D buckyballs, rolled into 1D nanotubes or stacked into 3D graphite [23]

CNT

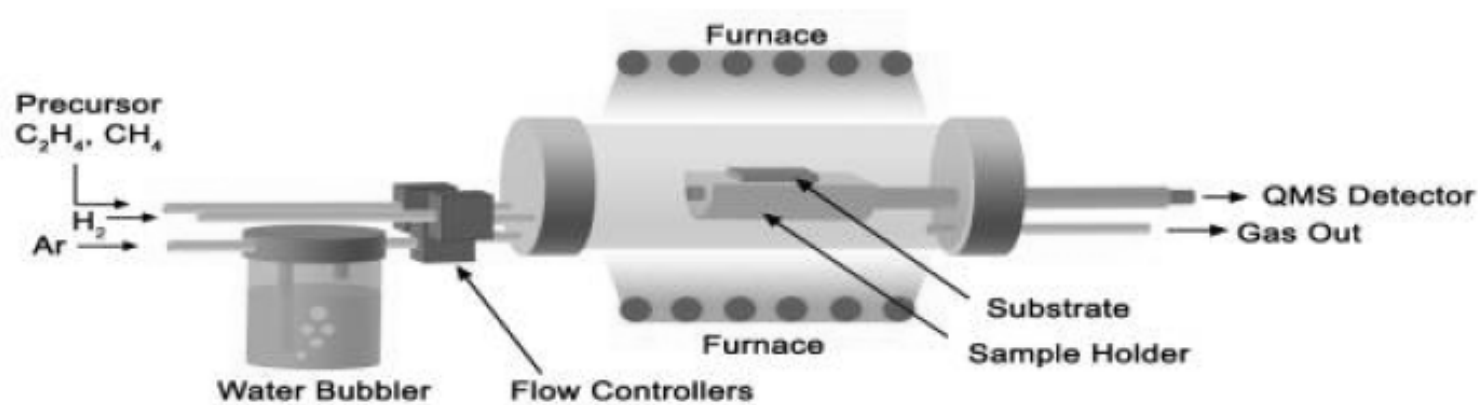
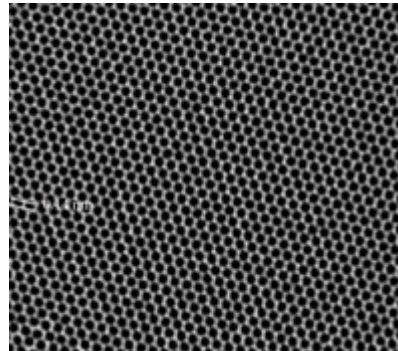
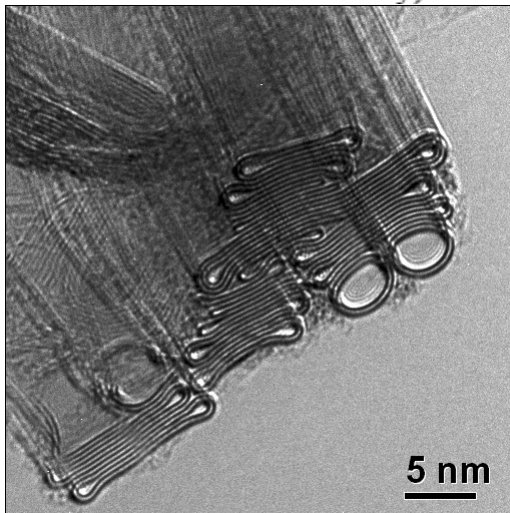


Fig. 1. Schematic of a CVD reactor for carbon nanotube growth. (Sketch by S. Yarmolenko from NCA&T State University)



Graphene

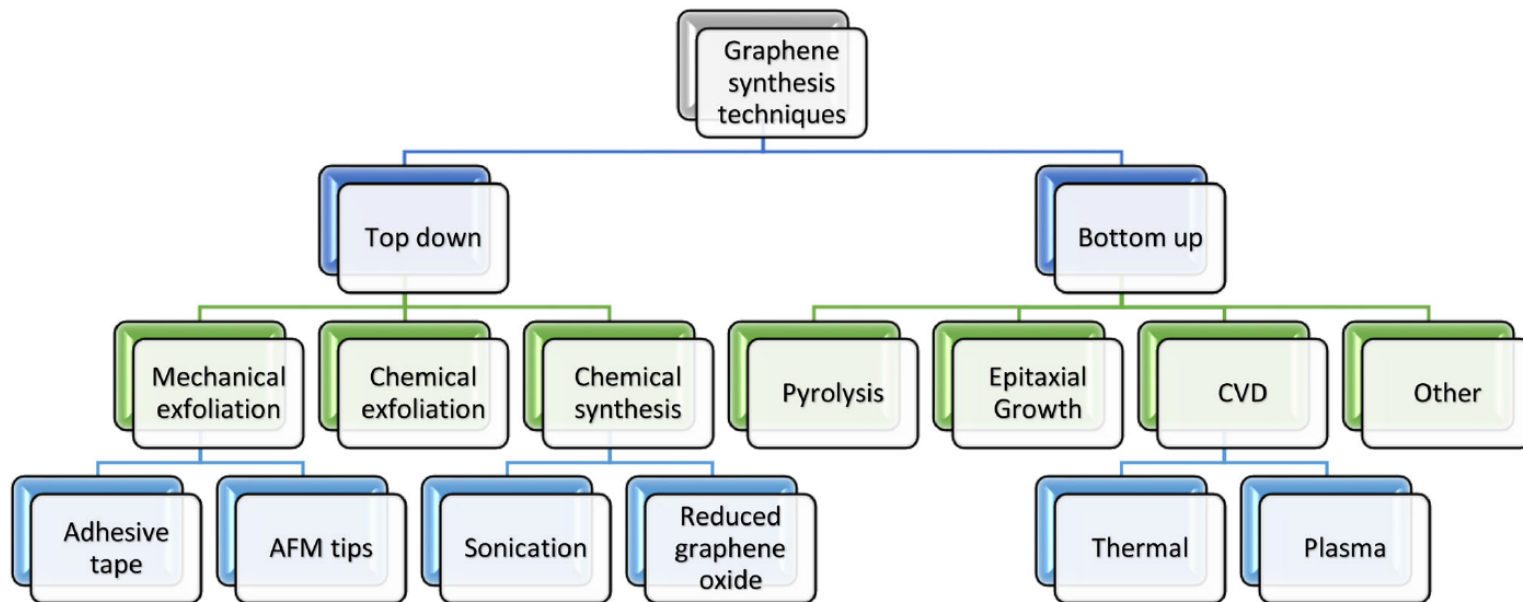
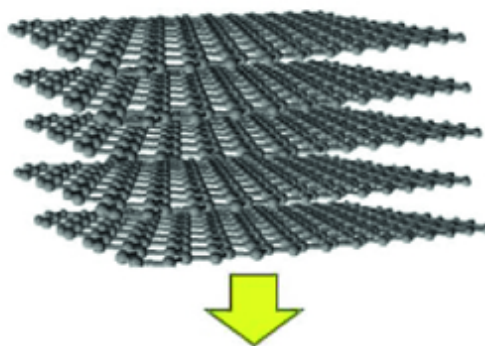
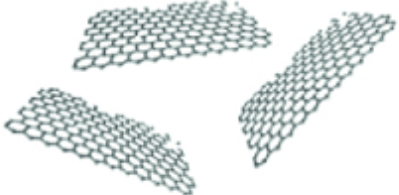


Fig. 2 A process flow chart of Graphene synthesis

Top-down

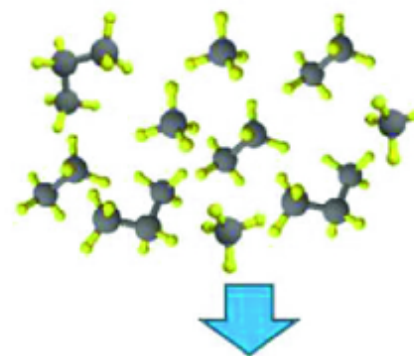
Source: Graphite

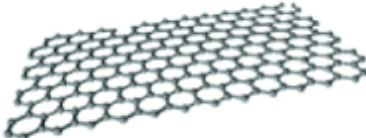


Mechanical exfoliation	Liquid phase and exfoliation	
Scotch tape, AFM tip.	Exfoliation of GIC	Reduction of GO
 <p>Graphene Size: nm~ μm</p>		
Low cost High quality	Low cost High Productivity Low defect	Low cost High Productivity Easy dispersion

Bottom-up

Source: CH₄, C₂H₆, C₃H₈ gas/ SiC

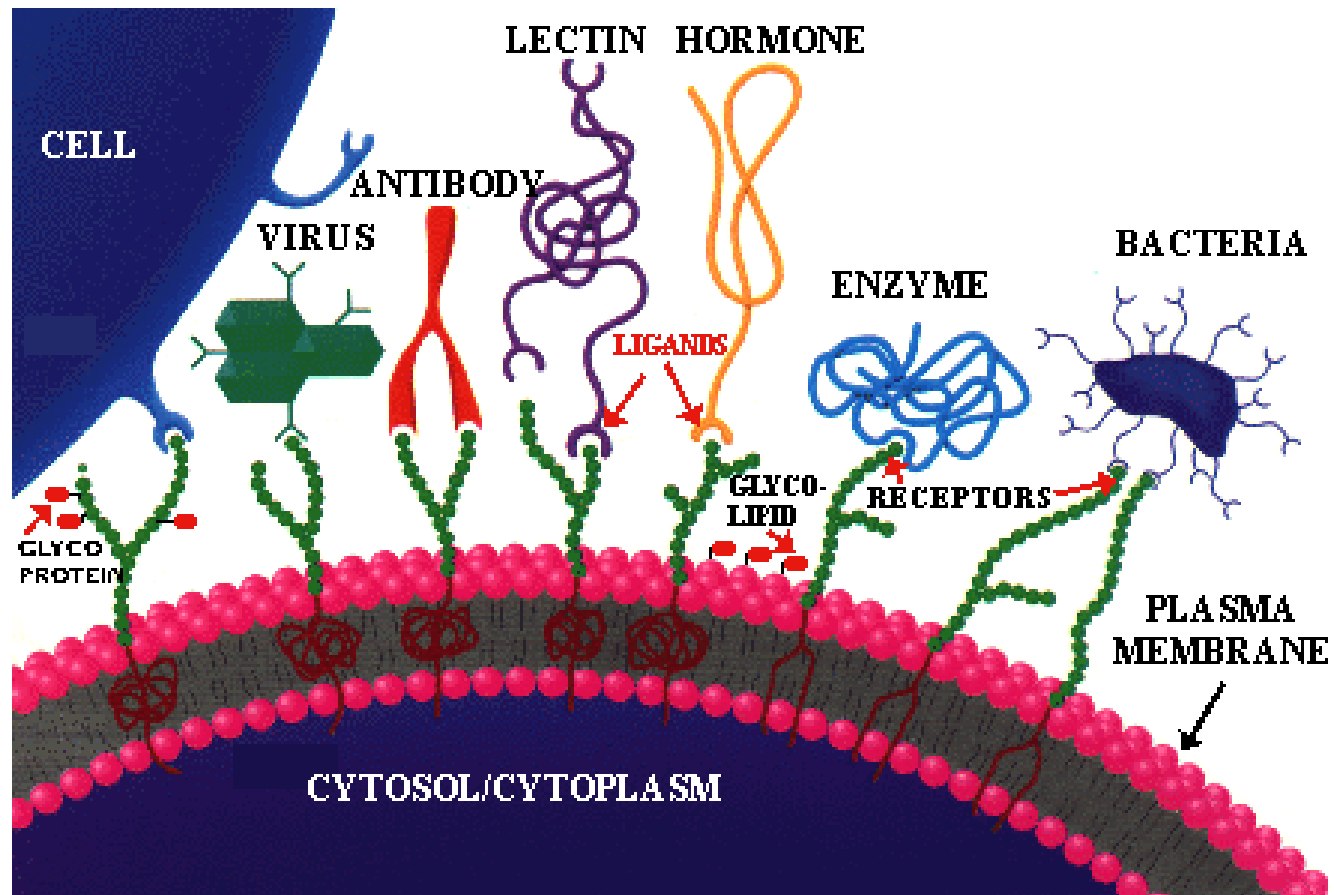


Epitaxial growth	CVD
Annealing of SiC wafer	Dissolving CH ₄ gas to Ni or Cu/ fast cooling
 <p>Graphene Size: wafer size</p>	
High transparency High conductivity Flexibility	

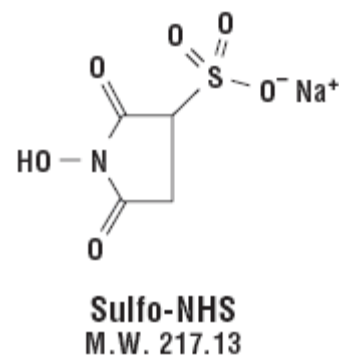
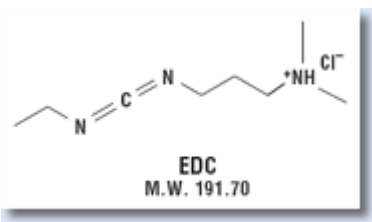
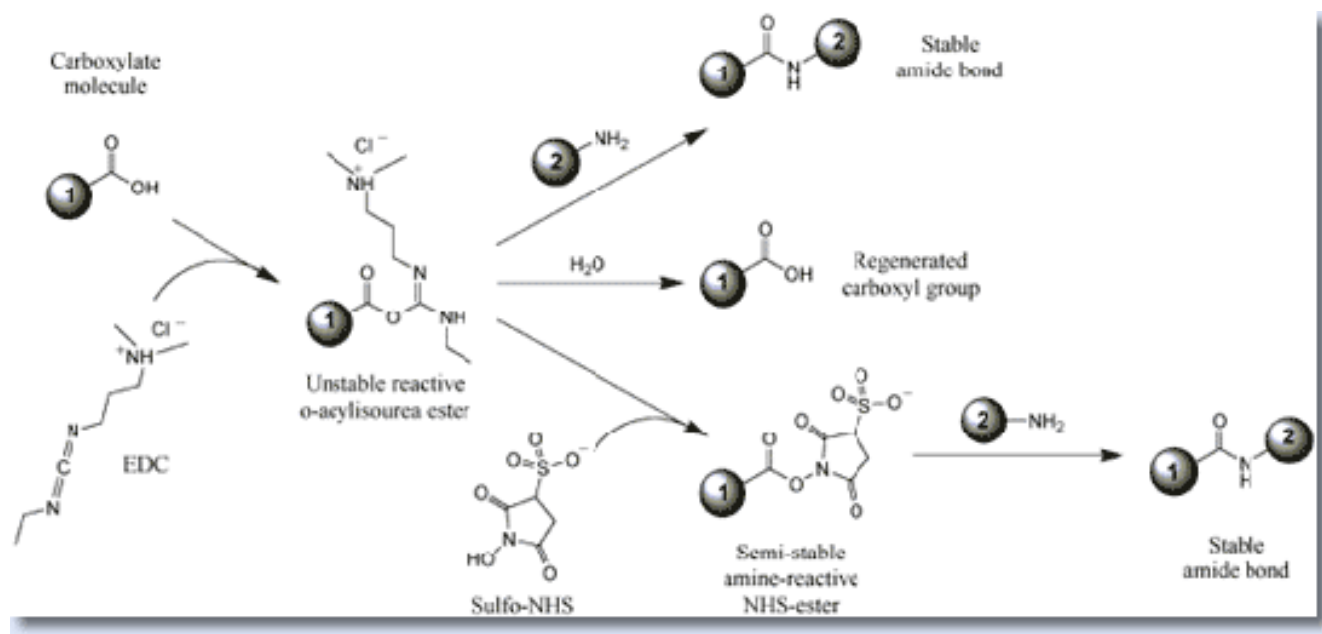
Surface Functionalization

- Recognition
 - Molecular Recognition
 - Protein
 - DNA
 - Saccharide
- Reporting/Detection
 - Dye
 - Quantum dots
 - SPR
 - SERS/LSPR
- Separation
 - Gel/Chromatography
 - Magnetic
- Surfaces
 - Gold and silver
 - Silicon oxide (glass)
 - Quantum dots
 - Polymer

Molecular Recognition

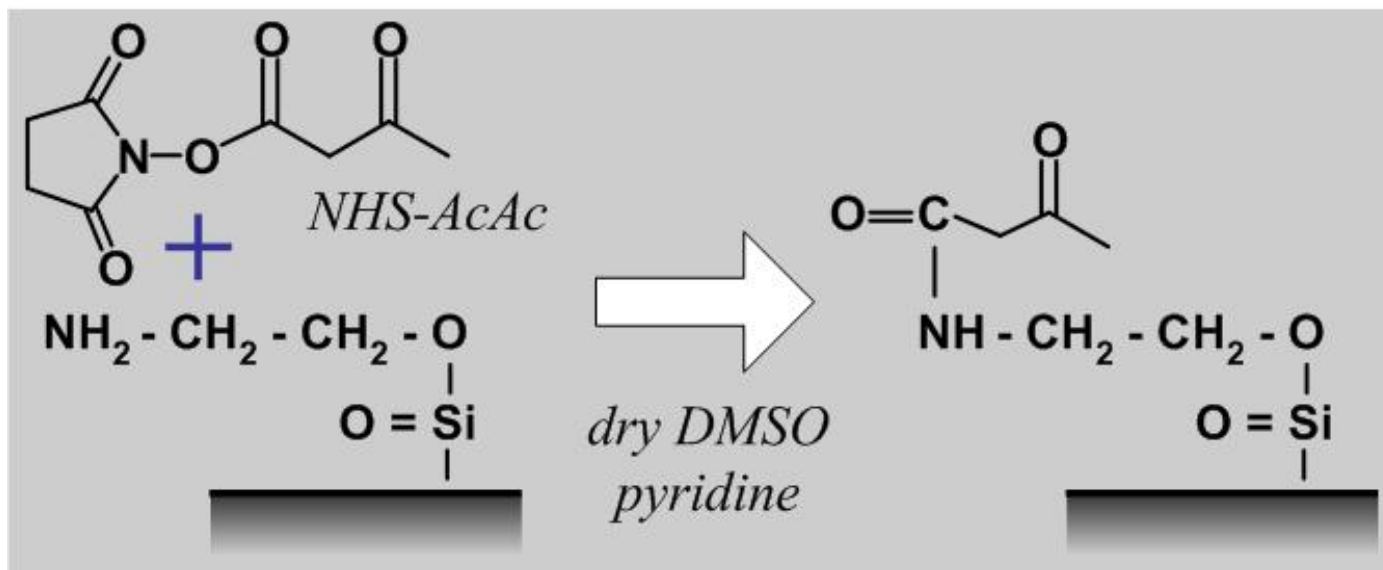


Carboxyl Presenting Surfaces

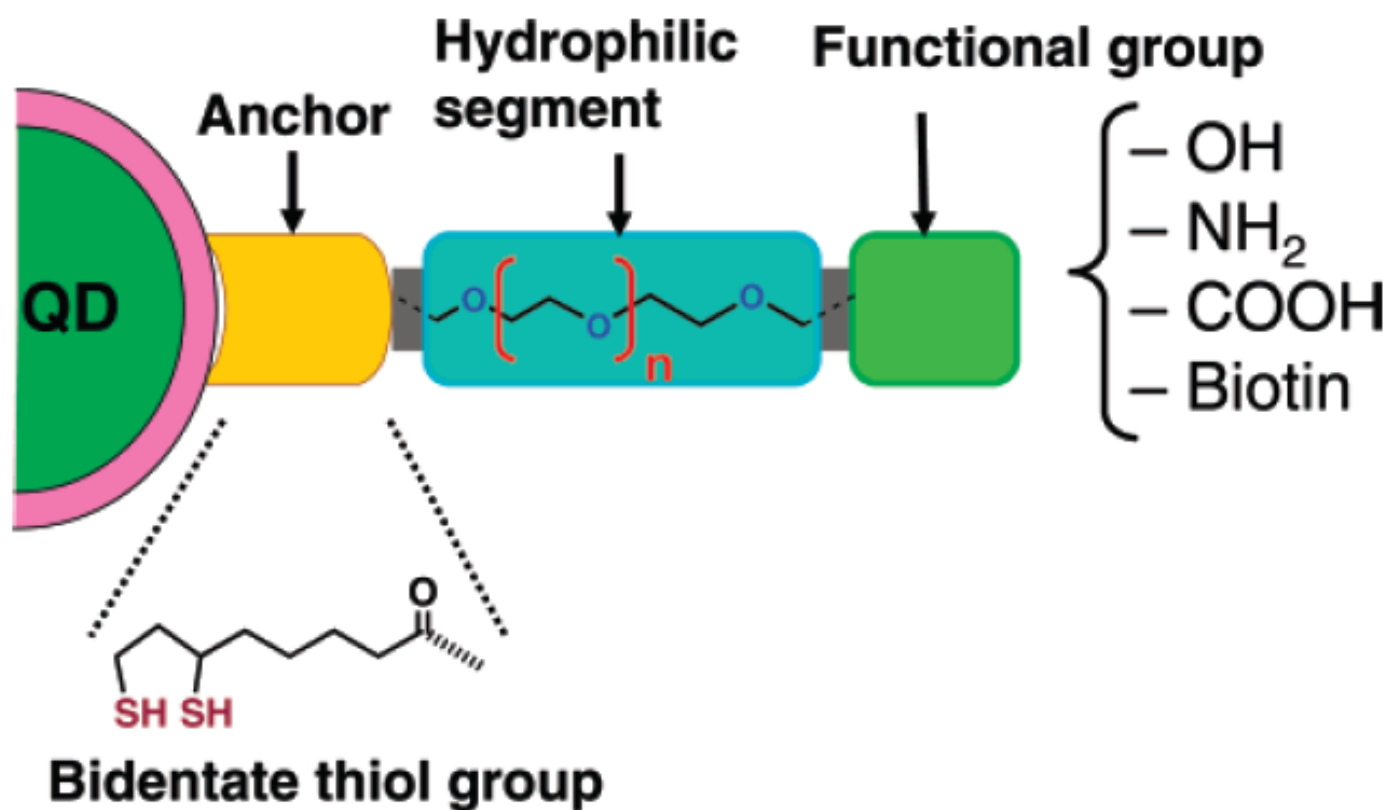


EDC (1-Ethyl-3-[3-dimethylaminopropyl]carbodiimide Hydrochloride)

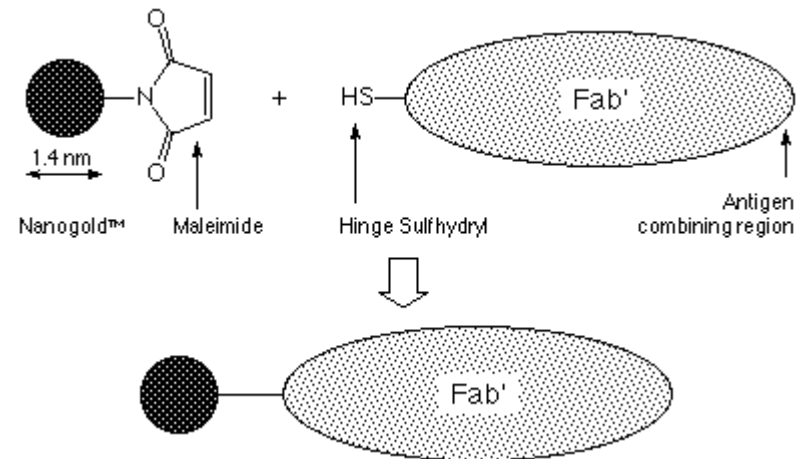
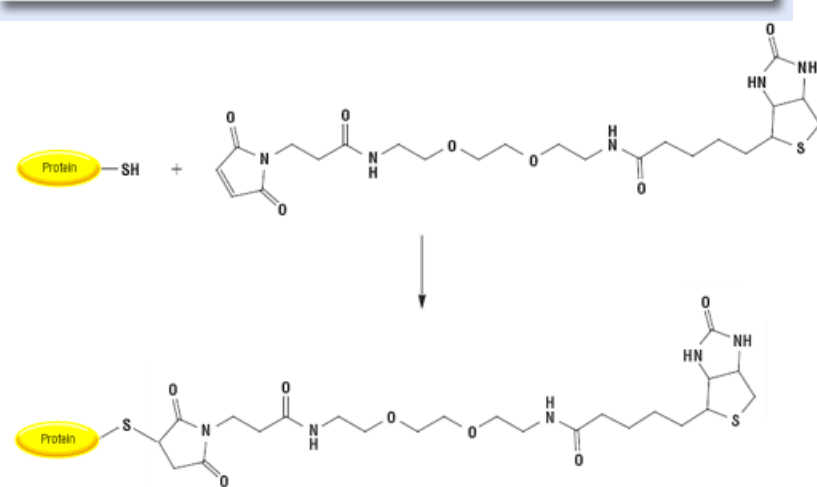
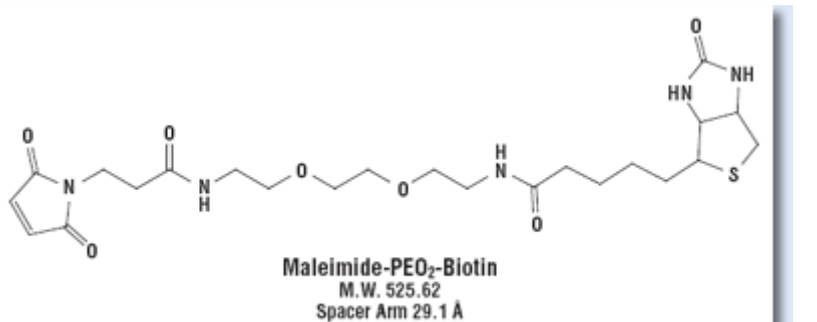
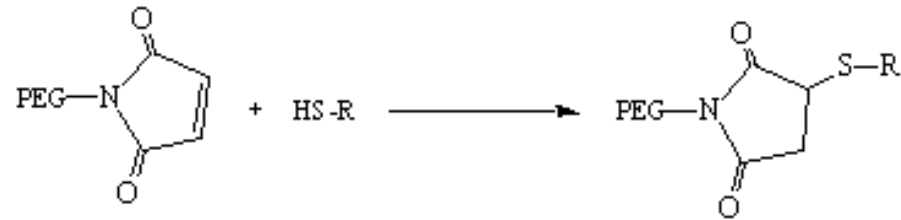
Amine Presenting Surface



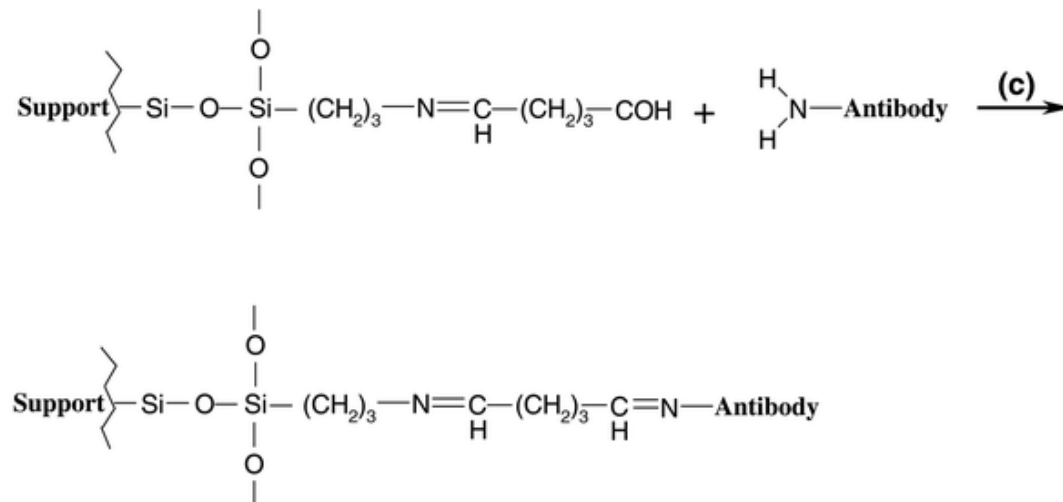
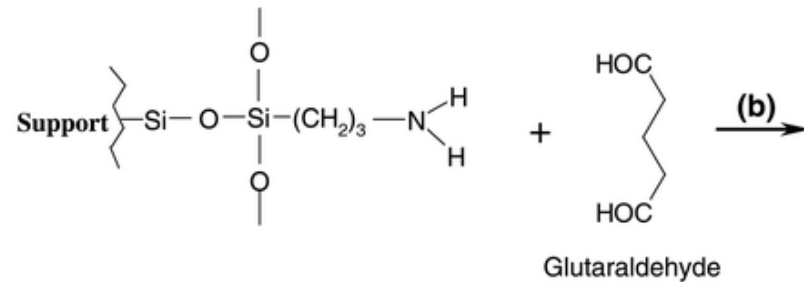
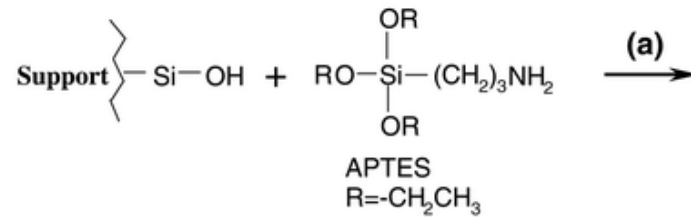
Scheme 1. Modular Design of Hydrophilic Ligands with Terminal Functional Groups Used in This Study



Sulfhydryl Labeling



Silica Modification



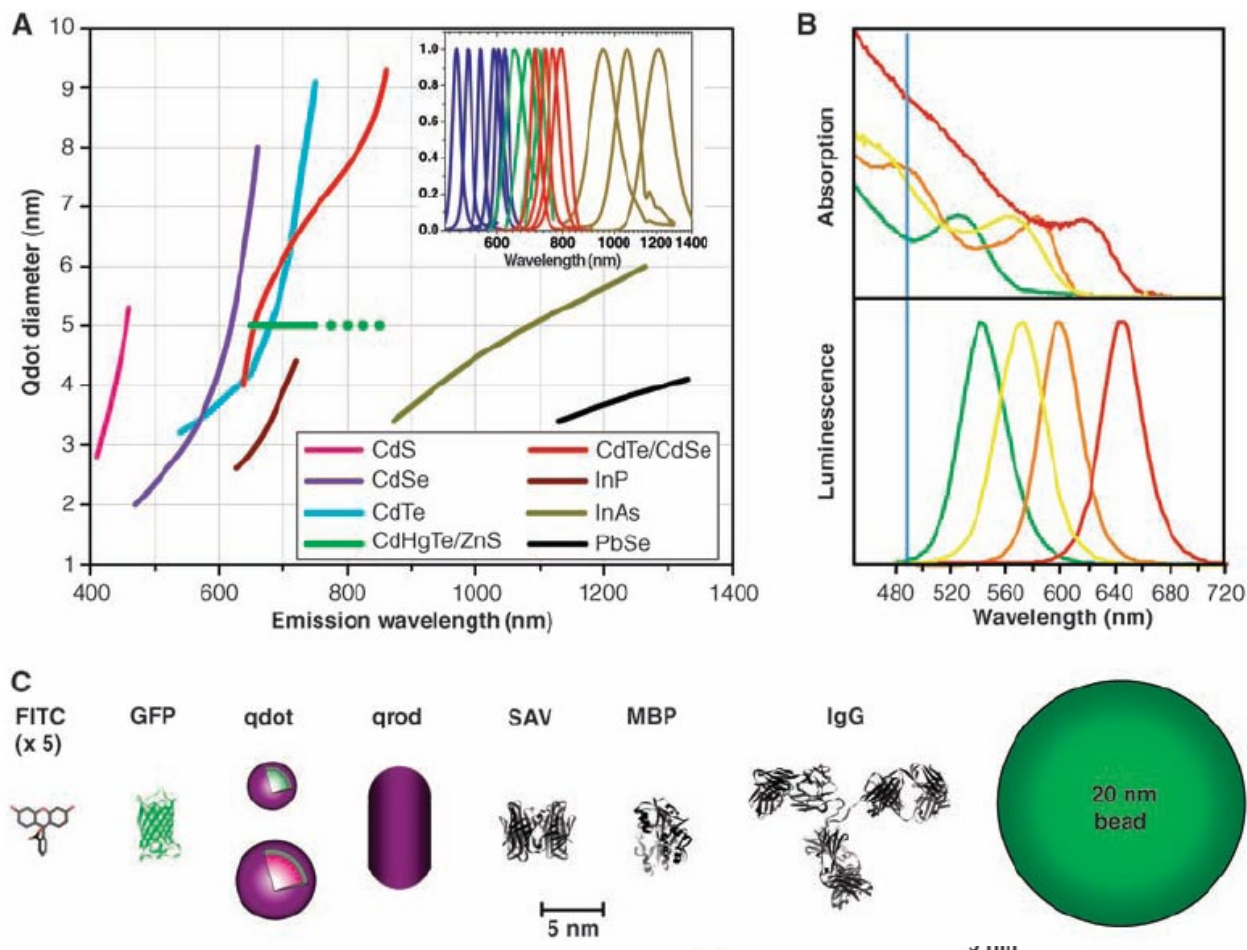
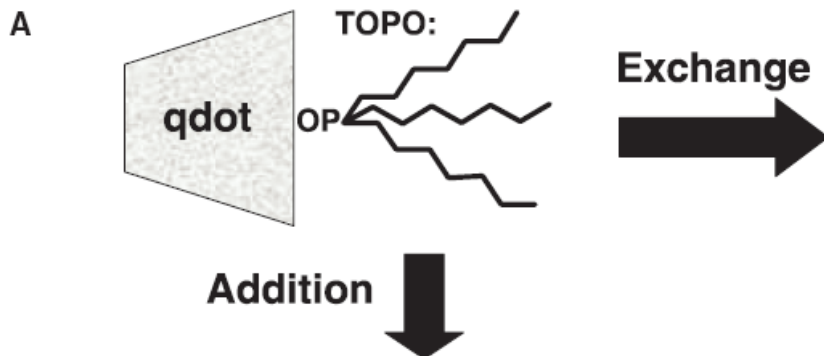
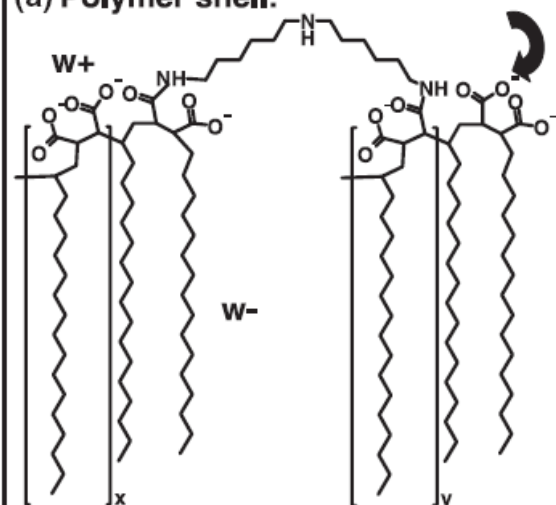


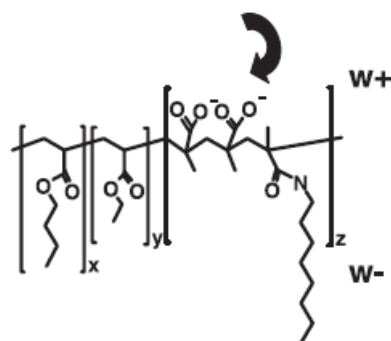
Fig. 1. (A) Emission maxima and sizes of quantum dots of different composition. Quantum dots can be synthesized from various types of semiconductor materials (II-VI: CdS, CdSe, CdTe...; III-V: InP, InAs...; IV-VI: PbSe...) characterized by different bulk band gap energies. The curves represent experimental data from the literature on the dependence of peak emission wavelength on qdot diameter. The range of emission wavelength is 400 to 1350 nm, with size varying from 2 to 9.5 nm (organic passivation/solubilization layer not included). All spectra are typically around 30 to 50 nm (full width at half maximum). Inset: Representative emission spectra for some materials. Data are from (12, 18, 27, 76–82). Data for CdHgTe/ZnS have been extrapolated to the maximum emission wavelength obtained in our group. (B) Absorption (upper curves) and emission (lower curves) spectra of four CdSe/ZnS qdot samples. The blue vertical line indicates the 488-nm line of an argon-ion laser, which can be used to efficiently excite all four types of qdots simultaneously. [Adapted from (28)] (C) Size comparison of qdots and comparable objects. FITC, fluorescein isothiocyanate; GFP, green fluorescent protein; qdot, green (4 nm, top) and red (6.5 nm, bottom) CdSe/ZnS qdot; qrod, rod-shaped qdot (size from Quantum Dot Corp.'s Web site). Three proteins—streptavidin (SAV), maltose binding protein (MBP), and immunoglobulin G (IgG)—have been used for further functionalization of qdots (see text) and add to the final size of the qdot, in conjunction with the solubilization chemistry (Fig. 2).



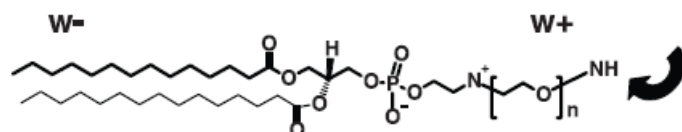
(a) Polymer shell:



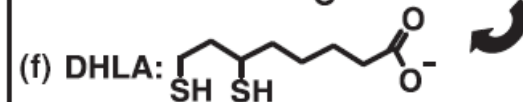
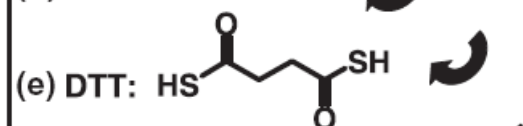
(b) Triblock copolymer:



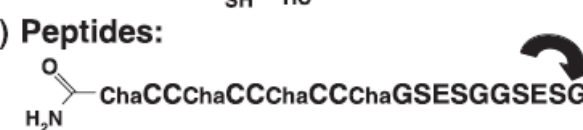
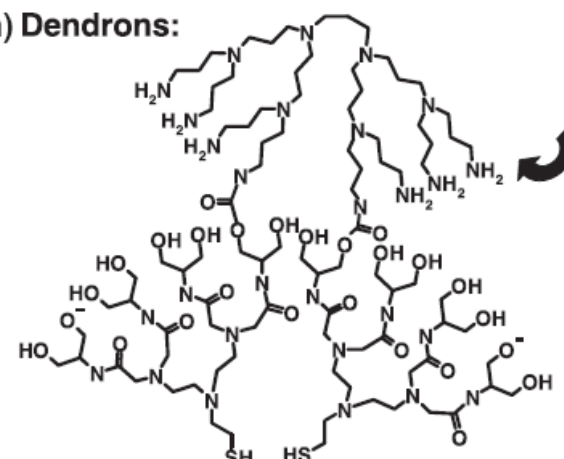
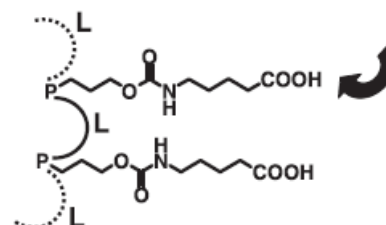
(c) Phospholipids:

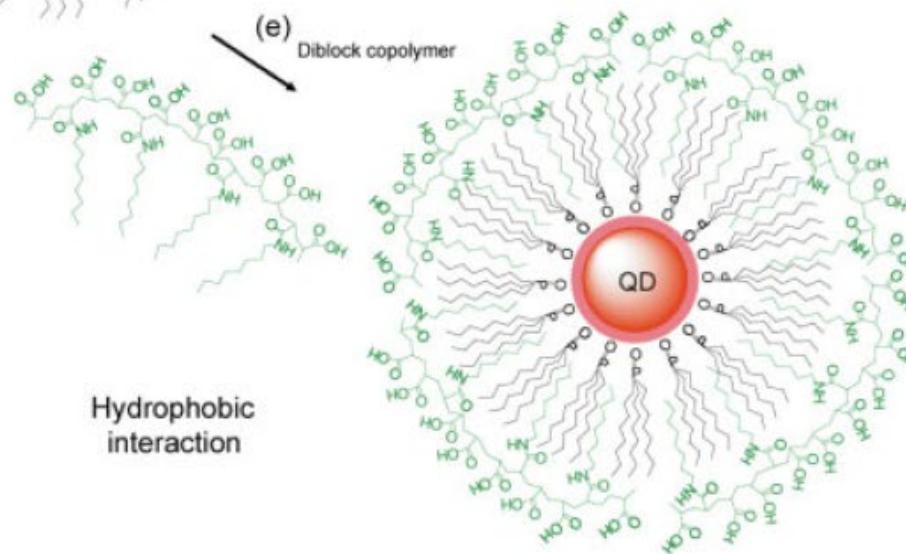
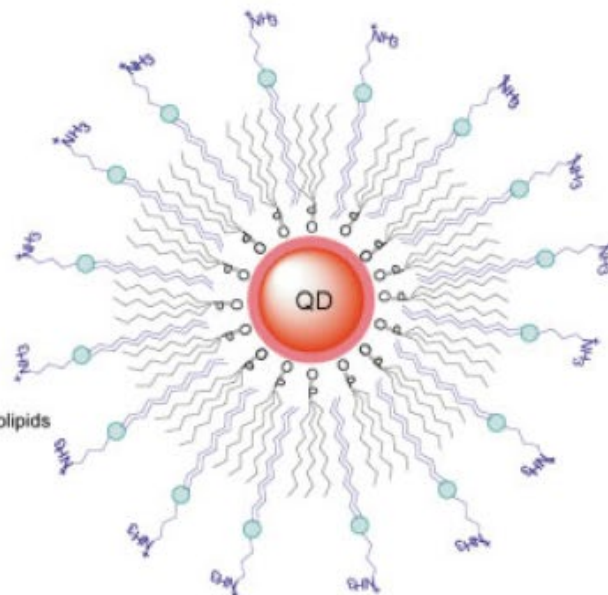
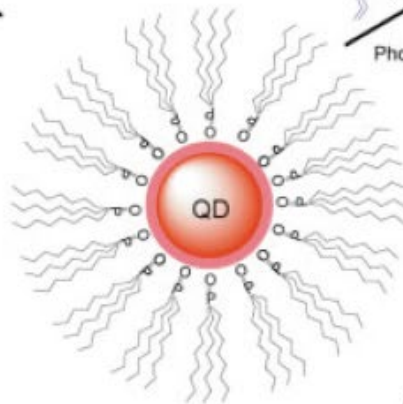
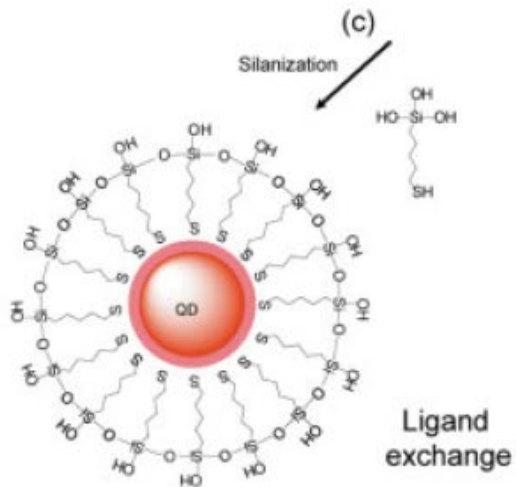
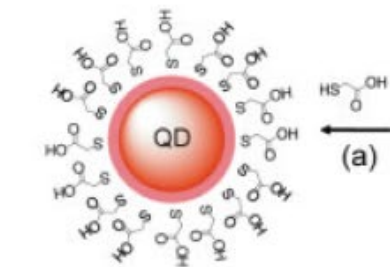
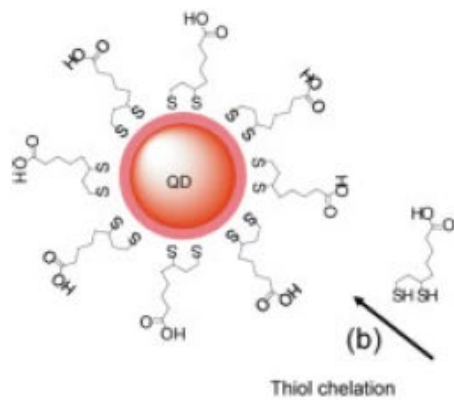


(d) MAA: HS-COOH



(g) Oligomeric phosphine:





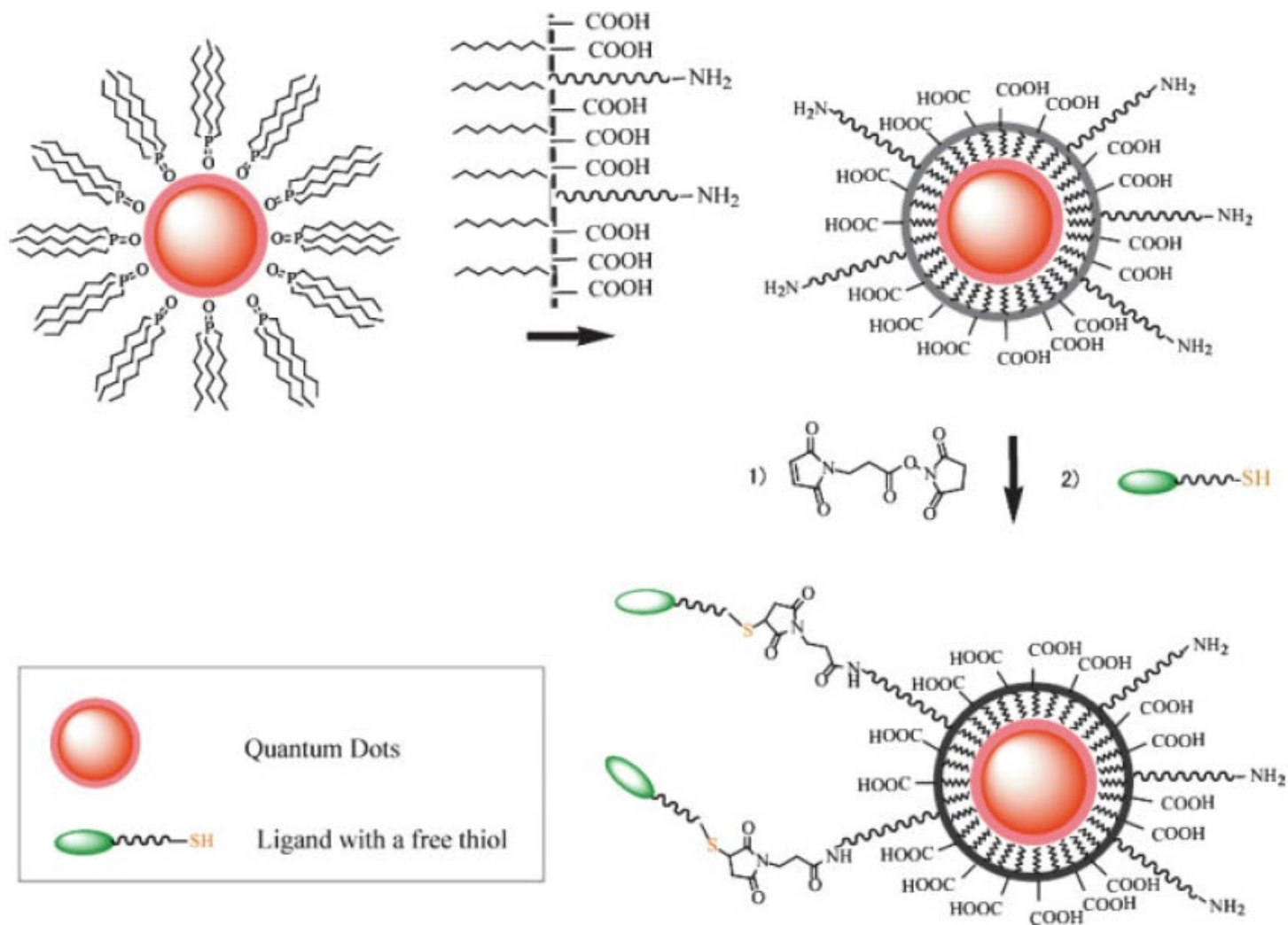


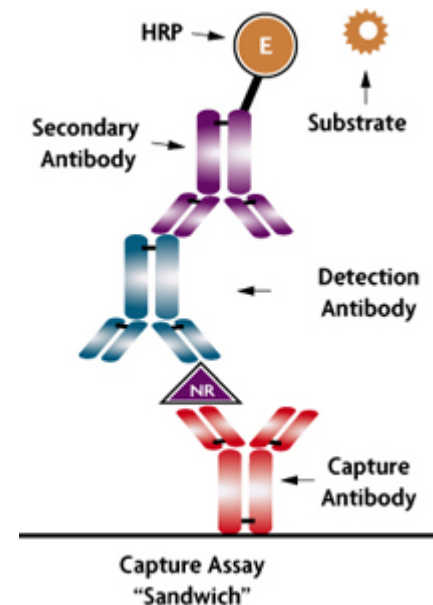
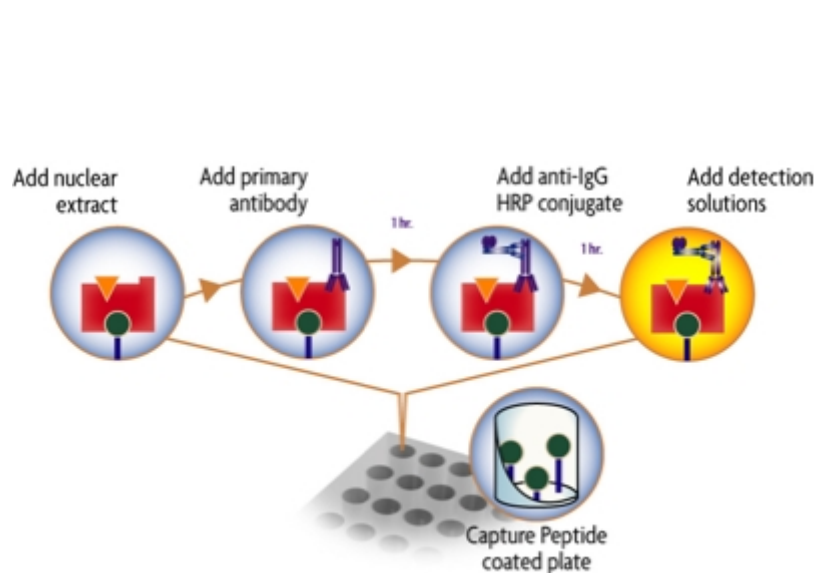
FIGURE 3 Maleimide functionalized QDs for conjugating thiol-containing ligands. TOPO stabilized QDs are coated with a primary amine functionalized tri-block amphiphilic copolymer for producing water-soluble QDs, which facilitate further conjugation to ligands with free thiols through bi-functional cross-linkers.

Nanomaterials for Biodiagnostic

- Nucleic Acid
 - Genetic information for identification
 - Diseases, bacterium, virus, pathogen
 - PCR with molecular fluorophore, State of the Art
 - Expansive, Non-portable, Non-multiplexing
- Proteins
 - Cancers and diseases, unusual high concentration of marker
 - ELISA (\sim pM) with molecular fluorophore
 - No PCR version

ELISA (Enzyme-Linked Immunosorbent Assay)

is a biochemical technique used mainly in immunology to detect the presence of an antibody or an antigen in a sample. It utilizes two antibodies, one of which is specific to the antigen and the other of which is coupled to an enzyme. This second antibody gives the assay its "enzyme-linked" name, and will cause a chromogenic or fluorogenic substrate to produce a signal.



Why Nanomaterials?

- Molecular fluorophores
 - Limited spectral response
 - photostability
- Nanomaterials
 - Small size (1-100 nm)
 - Chemically tailorable physical properties
 - Unusual target binding properties
 - Structure robustness

Nanomaterial Detection

- Optical
- Electrical and electrochemical
- Magnetic
- Nanowire and Nanotubes
- Nanofabrication

Colorimetric Detection of DNA

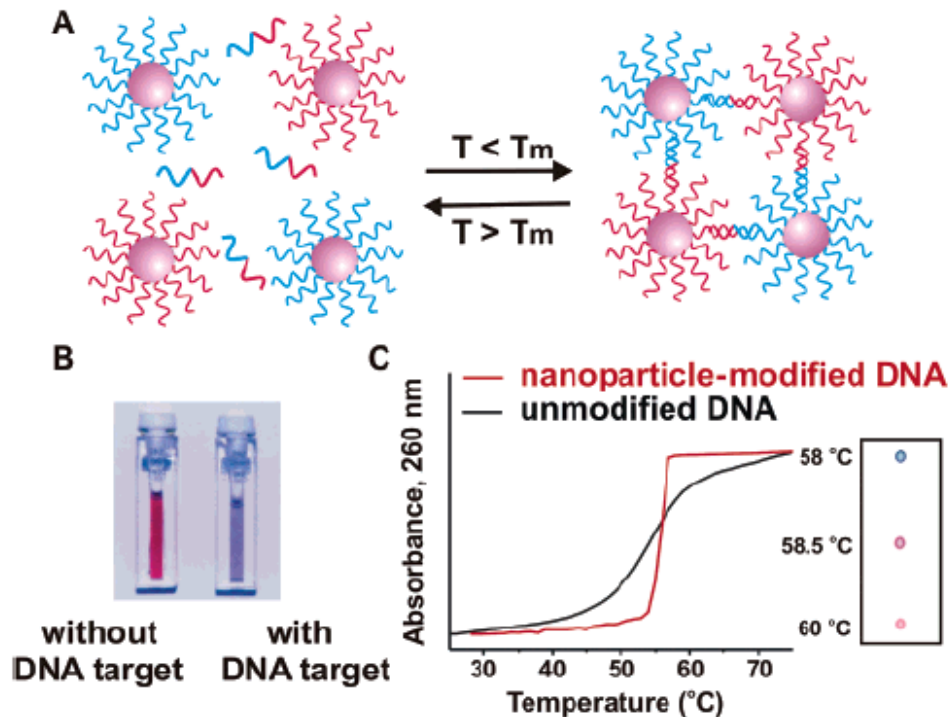


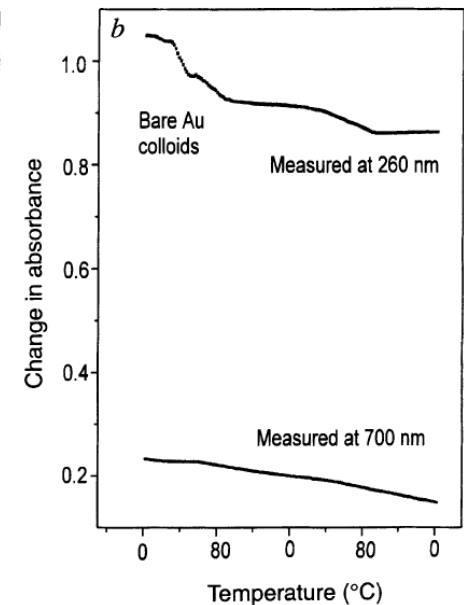
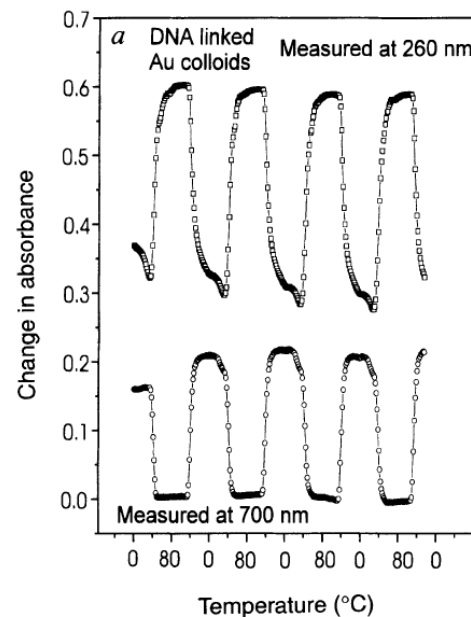
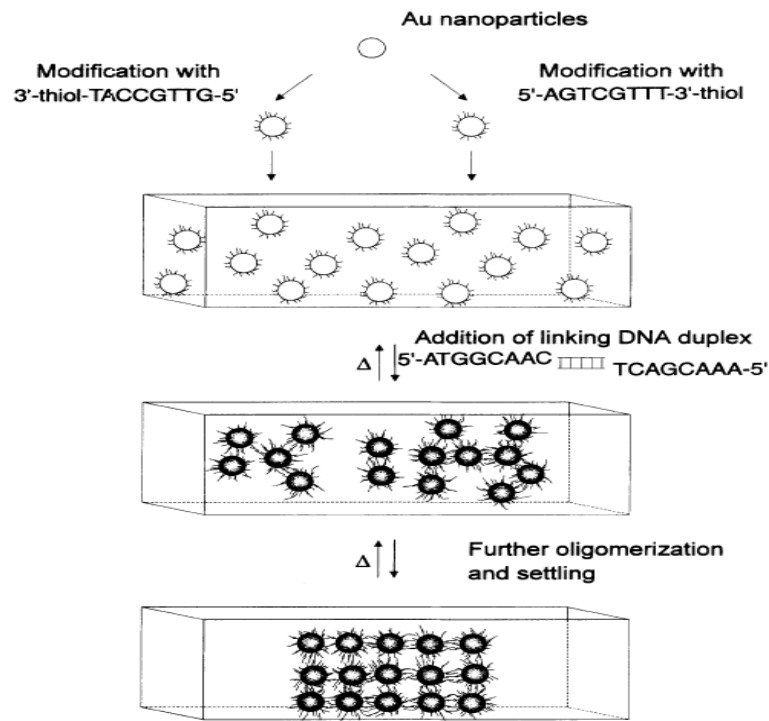
Figure 2. In the presence of complementary target DNA, oligonucleotide-functionalized gold nanoparticles will aggregate (A), resulting in a change of solution color from red to blue (B). The aggregation process can be monitored using UV-vis spectroscopy or simply by spotting the solution on a silica support (C). (Reprinted with permission from *Science* (<http://www.aaas.org>), ref 29. Copyright 1997 American Association for the Advancement of Science.)

A DNA-based method for rationally assembling nanoparticles into macroscopic materials

Chad A. Mirkin, Robert L. Letsinger, Robert C. Mucic & James J. Storhoff



FIG. 2 Cuvettes with the Au colloids and the four DNA strands responsible for the assembly process. Left cuvette, at 80 °C with DNA-modified colloids in the unhybridized state; centre, after cooling to room temperature but before the precipitate settles; and right, after the polymeric precipitate settles to the bottom of the cuvette. Heating either of these cool solutions results in the reformation of the DNA-modified colloids in the unhybridized state (shown in the left cuvette).



Selective Colorimetric Detection of Polynucleotides Based on the Distance-Dependent Optical Properties of Gold Nanoparticles

Robert Elghanian, James J. Storhoff, Robert C. Mucic, Robert L. Letsinger,* Chad A. Mirkin*

SCIENCE • VOL. 277 • 22 AUGUST 1997

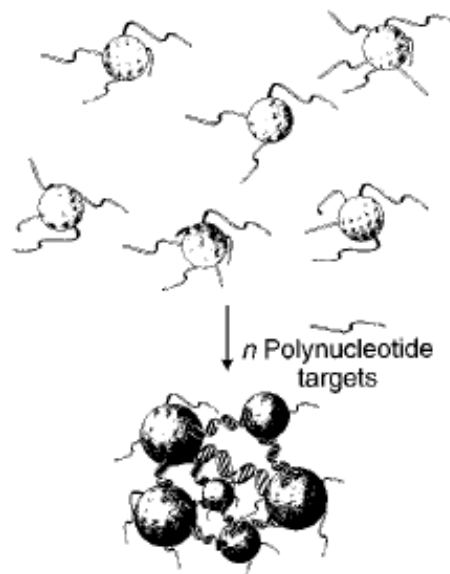


Fig. 1. Schematic representation of the concept for generating aggregates signaling hybridization of nanoparticle-oligonucleotide conjugates with oligonucleotide target molecules. The nanoparticles and the oligonucleotide interconnects are not drawn to scale, and the number of oligomers per particle is believed to be much larger than depicted.

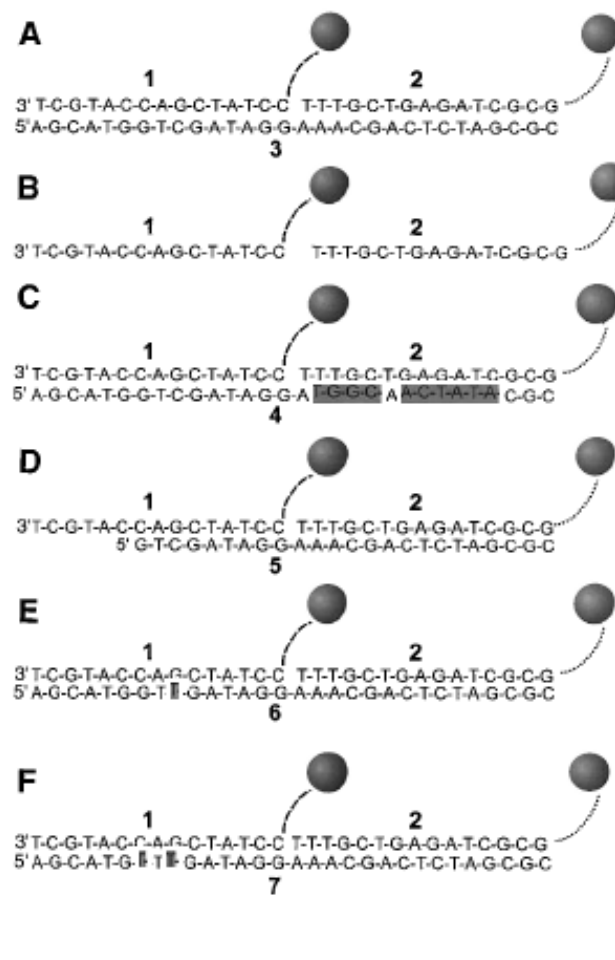


Fig. 2. Mercaptoalkyloligonucleotide-modified 13-nm Au particles and polynucleotide targets used for examining the selectivity of the nanoparticle-based colorimetric polynucleotide detection system. (A) Complementary target; (B) probes without the target; (C) a half-complementary target; (D) a 6-bp deletion; (E) a 1-bp mismatch; and (F) a 2-bp mismatch. For the sake of clarity, only two particles are shown; in reality a polymeric aggregate with many particles is formed. Dashed lines represent flexible spacer portions of the mercaptoalkyloligonucleotide strands bound to the nanoparticles; note that these spacers, because of their noncomplementary nature, do not participate in hybridization. The full sequences for the two probes, 1 and 2, which bind to targets 3 through 7, are

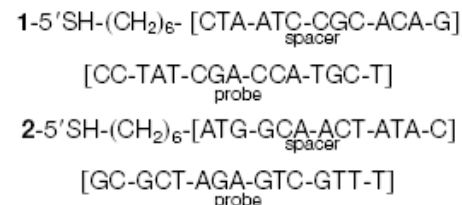
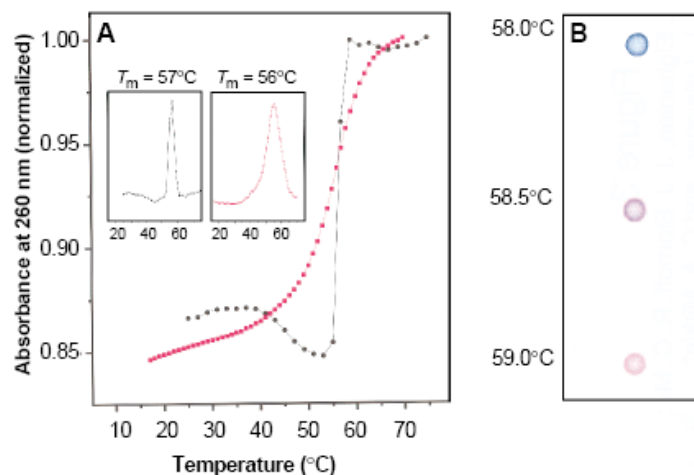


Fig. 3. (A) Comparison of the thermal dissociation curves for complexes of mercaptoalkyloligonucleotide-modified Au nanoparticles (black circles) and mercaptoalkyloligonucleotides without Au nanoparticles (red squares) with the complementary target, **3**, in hybridization buffer (0.1 M NaCl, 10 mM phosphate buffer, pH 7.0). For the first set (black circles), a mixture of 150 μ l of each colloid conjugate and 3 μ l of the target oligonucleotide in hybridization buffer (0.1 M

NaCl, 10 mM phosphate, pH 7.0) was frozen at the temperature of dry ice, kept for 5 min, thawed over a period of 15 min, and diluted to 1.0 ml with buffer (final target concentration, 0.02 μ M). The absorbance was measured at 1-min intervals with a temperature increase of 1°C per minute. The increase in absorption at 260 nm (A_{260}) was \sim 0.3 absorption units (AU). In the absence of the oligonucleotide targets, the absorbance of the nanoparticles did not increase with increasing temperature. For the second set, the mercaptoalkyloligonucleotides and complementary target (each 0.33 μ M) were equilibrated at room temperature in 1 ml of buffer, and the changes in absorbance with temperature were monitored as before. The increase in A_{260} was 0.08 AU. (**Insets**) Derivative curves for each set (15). (**B**) Spot test showing T_c (thermal transition associated with the color change) for the Au nanoparticle probes hybridized with complementary target. A solution prepared from 150 μ l of each probe and 3 μ l of the target (0.06 μ M final target concentration) was frozen for 5 min, allowed to thaw for 10 min, transferred to a 1-ml cuvette, and warmed at 58°C for 5 min in the thermally regulated cuvette chamber of the spectrophotometer. Samples (3 μ l) were transferred to a C₁₈ reverse phase plate with an Eppendorf pipette as the temperature of the solution was increased incrementally 0.5°C at 5-min intervals.



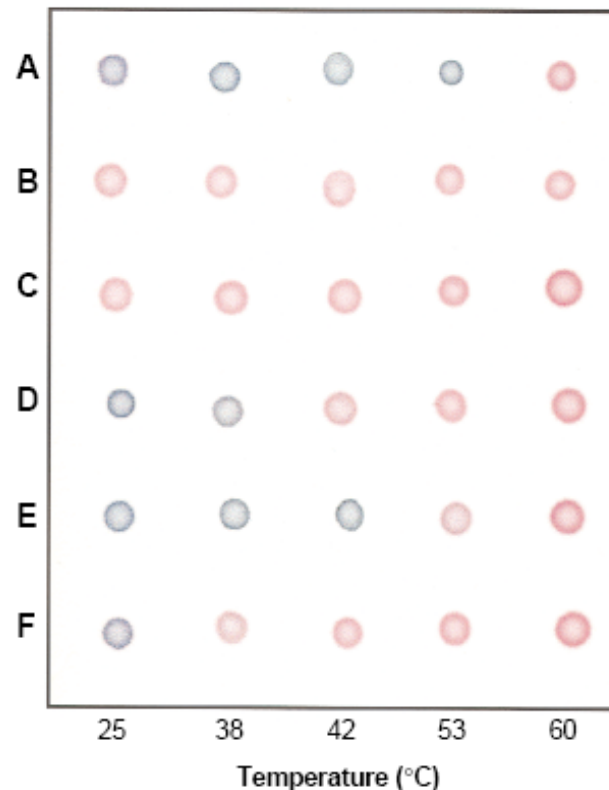
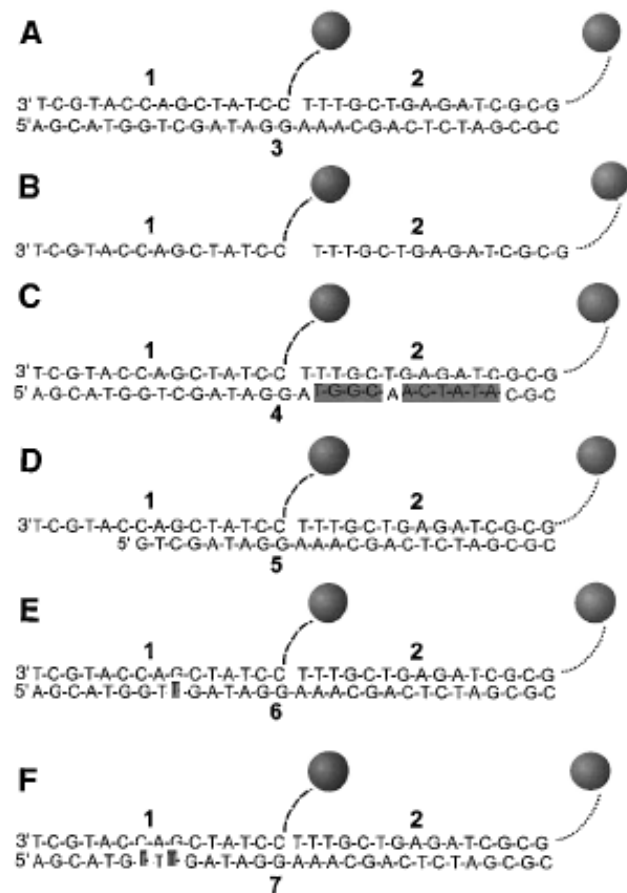


Fig. 4. Selective polynucleotide detection for the target probes shown in Fig. 2: **(A)** complementary target; **(B)** no target; **(C)** complementary to one probe; **(D)** a 6-bp deletion; **(E)** a 1-bp mismatch; and **(F)** a 2-bp mismatch. Nanoparticle aggregates were prepared in a 600- μ l thin-walled Eppendorf tube by addition of 1 μ l of a 6.6 μ M oligonucleotide target to a mixture containing 50 μ l of each probe (0.06 μ M final target concentration). The mixture was frozen (5 min) in a bath of dry ice and isopropyl alcohol and allowed to warm to room temperature. Samples were then transferred to a temperature-controlled water bath, and 3- μ l aliquots were removed at the indicated temperatures and spotted on a C₁₈ reverse phase plate.

Colloidal Au-Enhanced Surface Plasmon Resonance for Ultrasensitive Detection of DNA Hybridization

Lin He, Michael D. Musick, Sheila R. Nicewarner, Frank G. Salinas, Stephen J. Benkovic, Michael J. Natan, and Christine D. Keating*

Scheme 1. SPR Surface Assembly

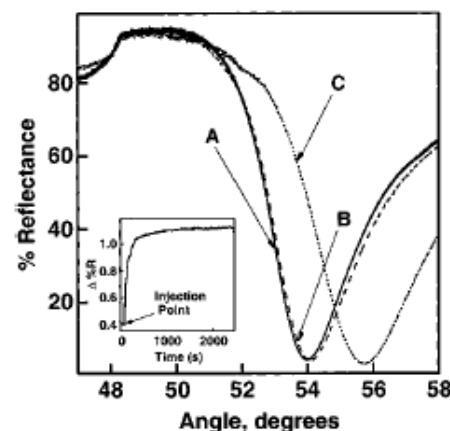
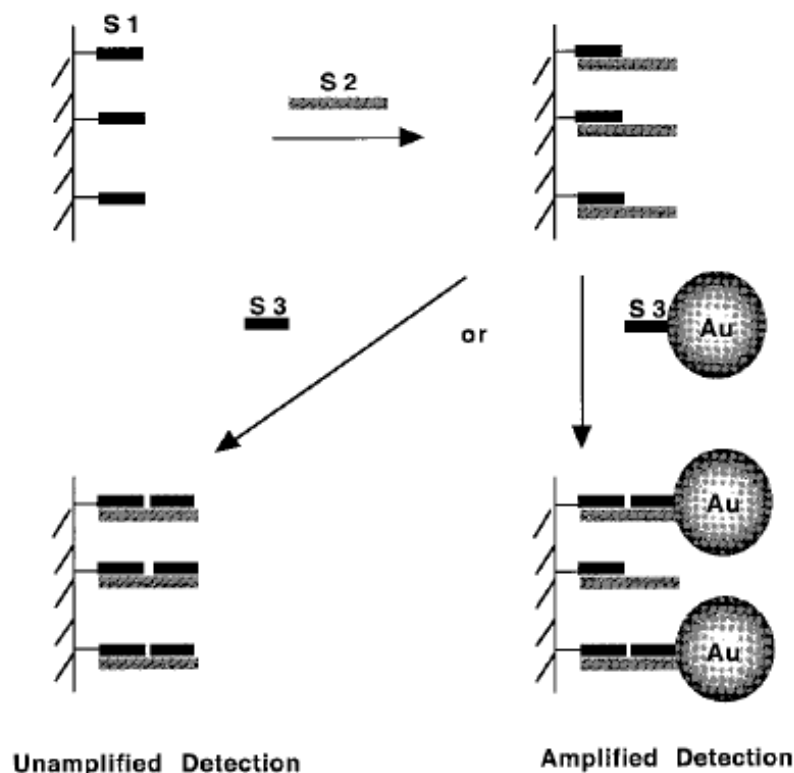


Figure 1. SPR curves of surfaces prepared in sequential steps as illustrated in Scheme 1: a MHA-coated Au film modified with a 12-mer oligonucleotide S1(A), after hybridization with its complementary 24-mer target S2 (B), and followed by introduction of S3: Au conjugate (C) to the surface. Inset: surface plasmon reflectance changes at 53.2° for the oligonucleotide-coated Au film measured during a 60-min exposure to S3: Au conjugates.

Scheme 2. SPR Surface Assembly in the Digestion Experiment

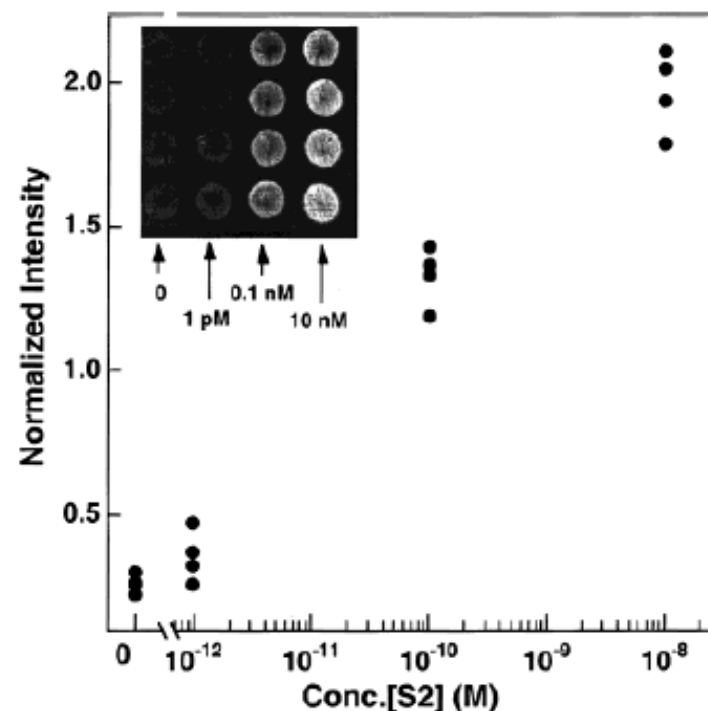
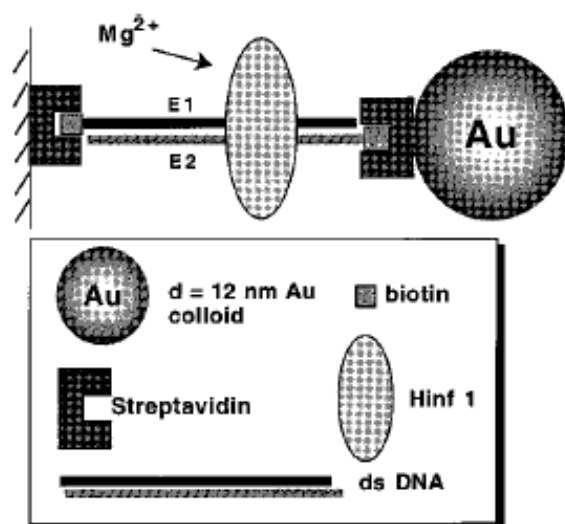


Figure 5. Plot of normalized intensity of SPR reflectance as a function of logarithmic concentration of the analyte 24-mer oligo (S2). Each spot represents one data point at the corresponding concentration. CCD parameters: exposure time = 0.3 s, 16 bit resolution, spot size = 4.5 mm in diameter. Inset: a 2-D SPR image of a Au surface derivatized with 20 μ L of buffer blank, 1 pM, 0.1 nM, and 10 nM S2 oligos (from left to right, respectively).

Self-Assembled Nanoparticle Probes for Recognition and Detection of Biomolecules

Dustin J. Maxwell, Jason R. Taylor, and Shuming Nie^{*,†}

9606 ■ J. AM. CHEM. SOC. 2002, 124, 9606–9612

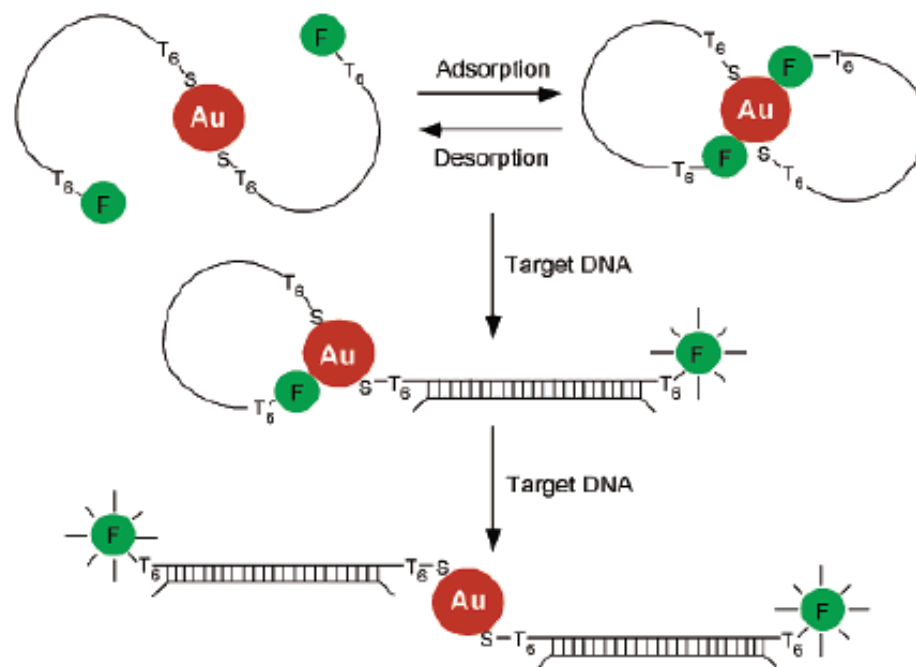


Figure 1. Nanoparticle-based probes and their operating principles. Two oligonucleotide molecules (oligos) are shown to self-assemble into a constrained conformation on each gold particle (2.5 nm diameter). A T₆ spacer (six thymines) is inserted at both the 3'- and 5'-ends to reduce steric hindrance. Single-stranded DNA is represented by a single line and double-stranded DNA by a cross-linked double line. In the assembled (closed) state, the fluorophore is quenched by the nanoparticle. Upon target binding, the constrained conformation opens, the fluorophore leaves the surface because of the structural rigidity of the hybridized DNA (double-stranded), and fluorescence is restored. In the open state, the fluorophore is separated from the particle surface by about 10 nm. See text for detailed explanation. Au, gold particle; F, fluorophore; S, sulfur atom.

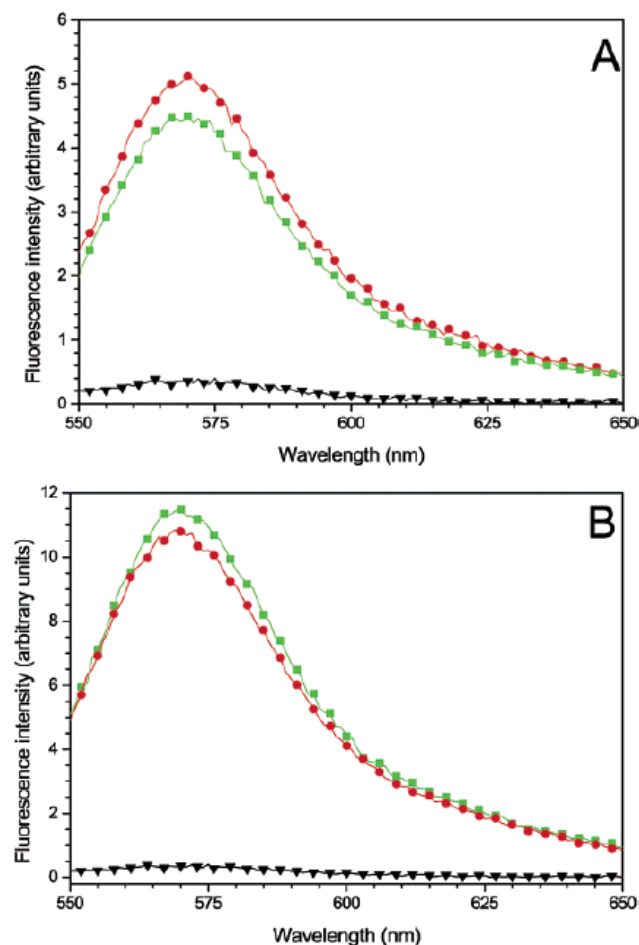


Figure 5. Fluorescence responses and the lack of sequence recognition abilities observed for nonthiolated nanoparticle probes. (A) Fluorescence spectra of nonthiolated probes generated by a complementary target (red curve), a noncomplementary target (green curve), and no target (black curve). These probes are considered nonfunctional because they do not recognize specific DNA sequences. (B) Fluorescence signals obtained from the supernatant solution when the probes were treated with a complementary target (red curve) or a noncomplementary target (green curve). The result revealed that the oligos were released into solution by nonspecific adsorption of the target on the particle surface. With a thiol group, this release was not observed (little or no signal in solution, black curve in B). The nonfunctional probes were prepared in the same way as the functional probes, except that the 3'-end thiol group was deleted. The intensity differences for the red and green curves were within experimental errors and had no particular significance.

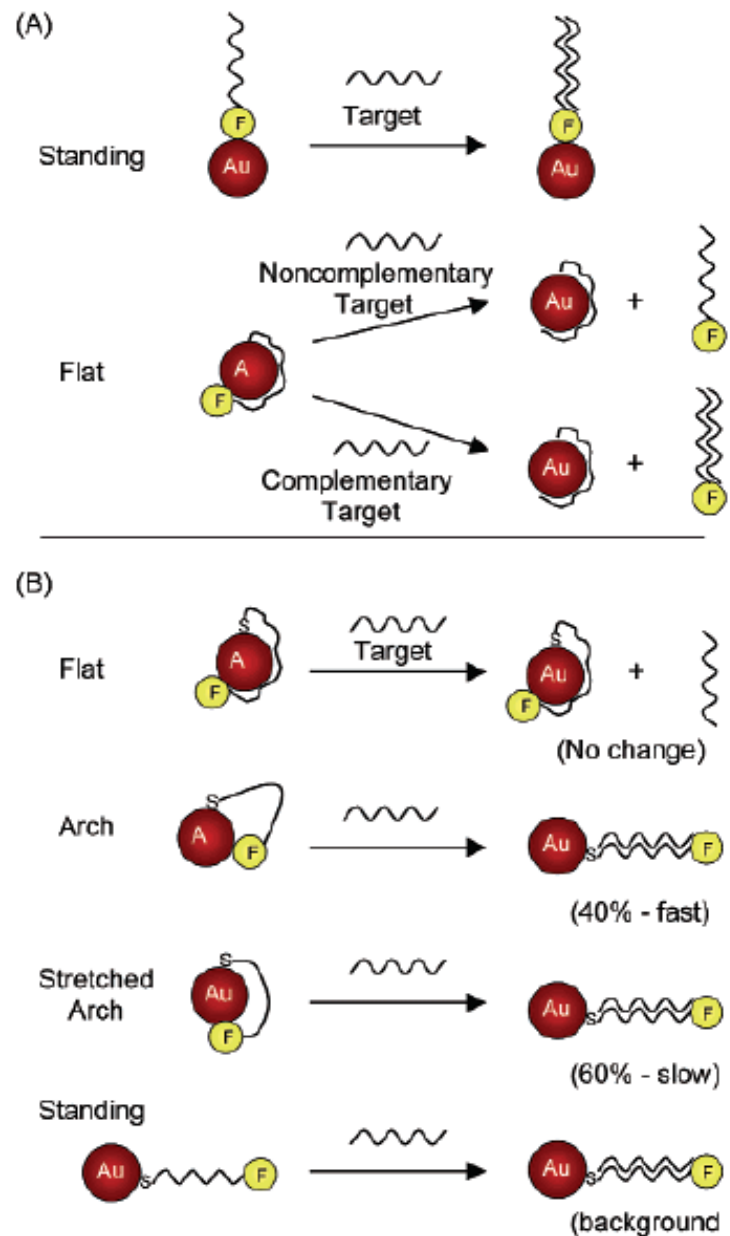
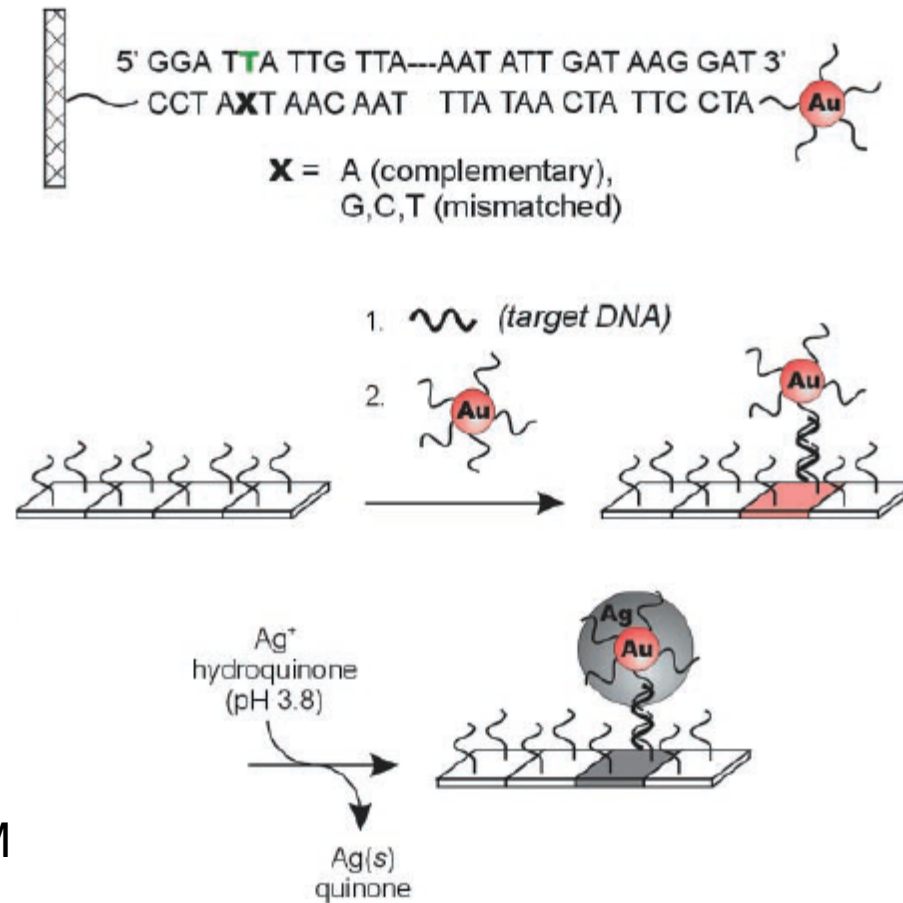


Figure 6. Schematic illustration of possible configurations for (a) nonthiolated and (b) thiolated oligonucleotides adsorbed on colloidal gold nanocrystals. Detailed discussion in text.

Scanometric DNA Array Detection with Nanoparticle Probes

SCIENCE VOL 289 8 SEPTEMBER 2000

T. Andrew Taton,^{1,2} Chad A. Mirkin,^{1,2*} Robert L. Letsinger^{1*}



50 fM => 0.2 fM

Fig. 1. Images of 7 mm by 13 mm, oligonucleotide-functionalized, float glass slides, obtained with a flatbed scanner. (A) Slide before hybridization of target and nanoparticle probe. (B) A slide identical to (A) after hybridization with oligonucleotide target (10 nM) and then nanoparticle probes (5 nM in particles). The pink color derives from the Au nanoparticle probes. (C) A slide identical to (B) after exposure to silver amplification solution for 5 min. (D) Slide before hybridization of target and nanoparticle probe. (E) A slide identical to (D) after hybridization with target (100 pM) and then nanoparticle probe (5 nM). The extinction of the submonolayer of nanoparticles is too low to be observed visually or with a flatbed scanner. (F) A slide identical to (E) after exposure to silver amplification solution for 5 min. Slide (F) is lighter than slide (C), indicating a lower concentration of target. (G) A control slide exposed to 5 nM nanoparticle probe and then exposed to silver amplification solution for 5 min. No darkening of the slide is observed. (H) Graph of 8-bit gray scale values as a function of target concentration. The gray scale values were taken from flatbed scanner images of oligonucleotide-functionalized glass surfaces that had been exposed to varying concentrations of oligonucleotide target, labeled with 5 nM oligonucleotide probe and immersed in silver amplification solution. For any given amplification time, the grayscale range is limited by surface saturation at high grayscale values and the sensitivity of the scanner at low values. Therefore, the dynamic range of this system can be adjusted by means of hybridization and amplification conditions (that is, lower target concentrations require longer amplification periods). Squares: 18-base capture-target overlap (5), 8× PBS hybridization buffer [1.2 M NaCl and 10 mM NaH₂PO₄/Na₂HPO₄ buffer (pH 7)], 15 min amplification time. Circles: 12-base capture-target overlap, 8× PBS hybridization buffer, 10 min amplification time. Triangles: 12-base capture-target overlap, 2× PBS hybridization buffer [0.3 M NaCl, 10 mM NaH₂PO₄/Na₂HPO₄ buffer (pH 7)], 5 min amplification time. The lowest target concentration that can be effectively distinguished from the background baseline is 50 fM.

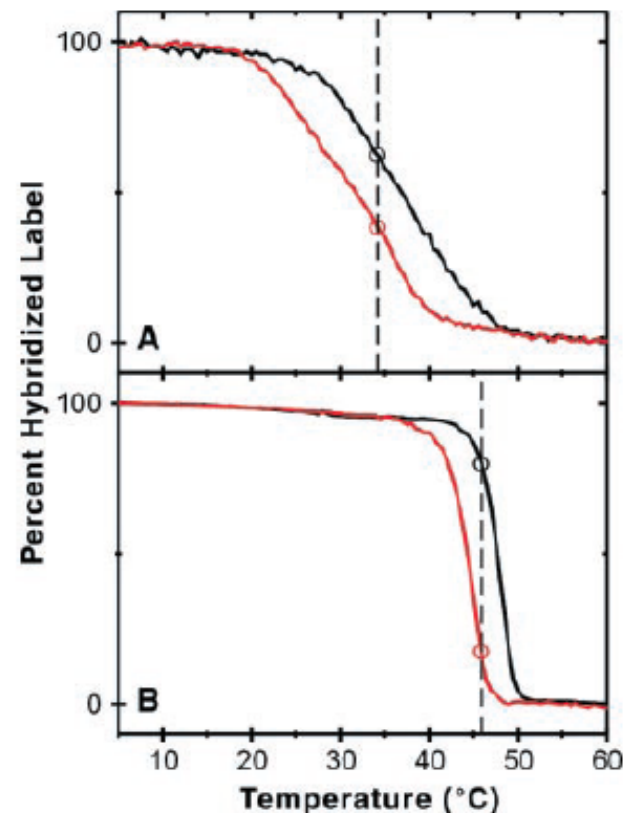
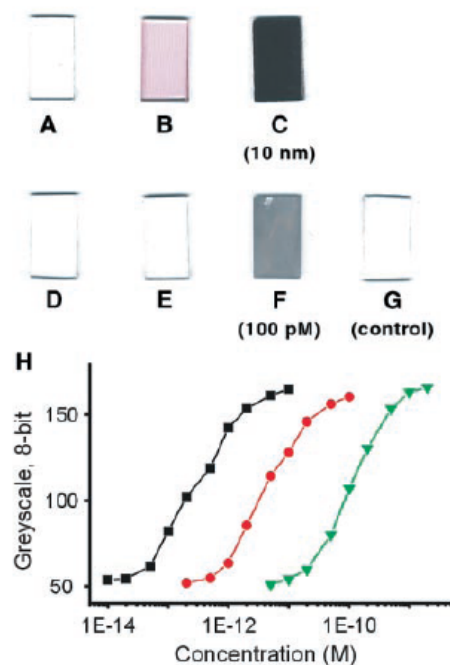
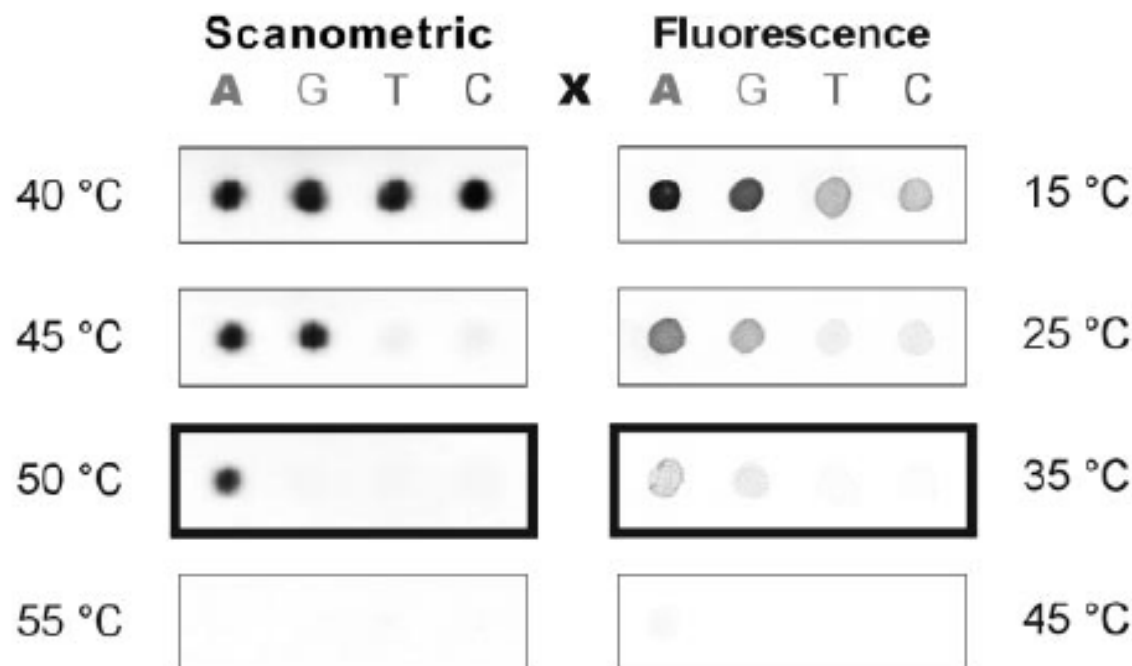


Fig. 3. (Left) Nanoparticle-labeled arrays developed at different stringency temperatures. Model oligonucleotide arrays (with the capture sequences shown in Scheme 1) were treated with oligonucleotide target and nanoparticle probes, followed by a 2-min buffer wash at the temperatures shown and subsequent silver amplification (13). Images were obtained

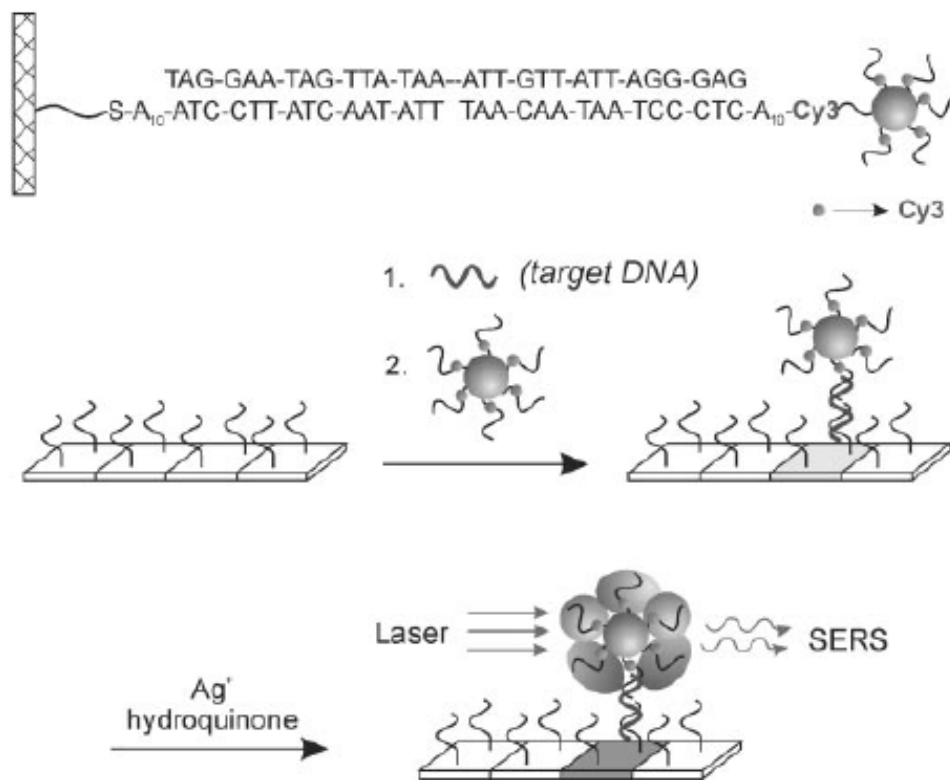
with an Epson Expression 636 (600 dots per inch) flatbed scanner (Epson America, Long Beach, California). The darkened border indicates the array that showed optimum selectivity for the perfectly complementary target; at this temperature, the ratio of background-subtracted, 8-bit gray scale values for elements A:G:T:C, obtained from histogram averages in Adobe Photoshop (Adobe Systems, San Jose, California), is 96:9:7:6. **(Right)** Fluorophore-labeled arrays washed at different stringency temperatures. Model oligonucleotide arrays identical to those shown at left were treated with oligonucleotide target and Cy3-labeled oligonucleotide probes, followed by a 2-min buffer wash at the temperatures shown. Images were obtained with a ScanArray Confocal Microarray Scanner (GSI Lumonics, Billerica, Massachusetts). The darkened border indicates the array that showed the highest selectivity for the perfectly complementary target, as calculated by the QuantArray Analysis software package (GSI Lumonics); at this temperature, the intensity ratio (in percent, with the intensity of the X = A element at 15°C set to 100%) for elements A:G:T:C is 18:7:1:1.



Nanoparticles with Raman Spectroscopic Fingerprints for DNA and RNA Detection

YunWei Charles Cao, Rongchao Jin, Chad A. Mirkin*

30 AUGUST 2002 VOL 297 SCIENCE



1 fM

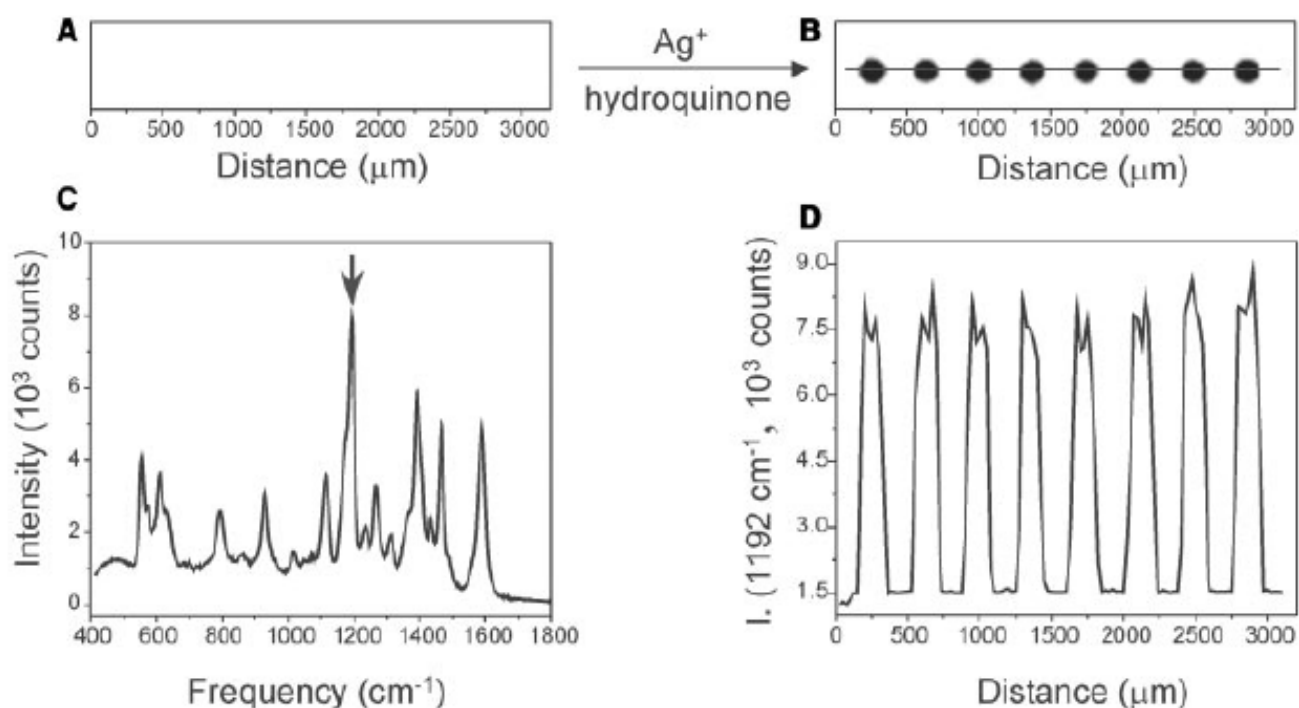


Fig. 1. Flatbed scanner images of microarrays hybridized with nanoparticles (**A**) before and (**B**) after Ag enhancing. (**C**) A typical Raman spectrum acquired from one of the Ag spots. (**D**) A profile of Raman intensity at 1192 cm^{-1} as a function of position on the chip; the laser beam from the Raman instrument is moved over the chip from left to right as defined by the line in (**B**).

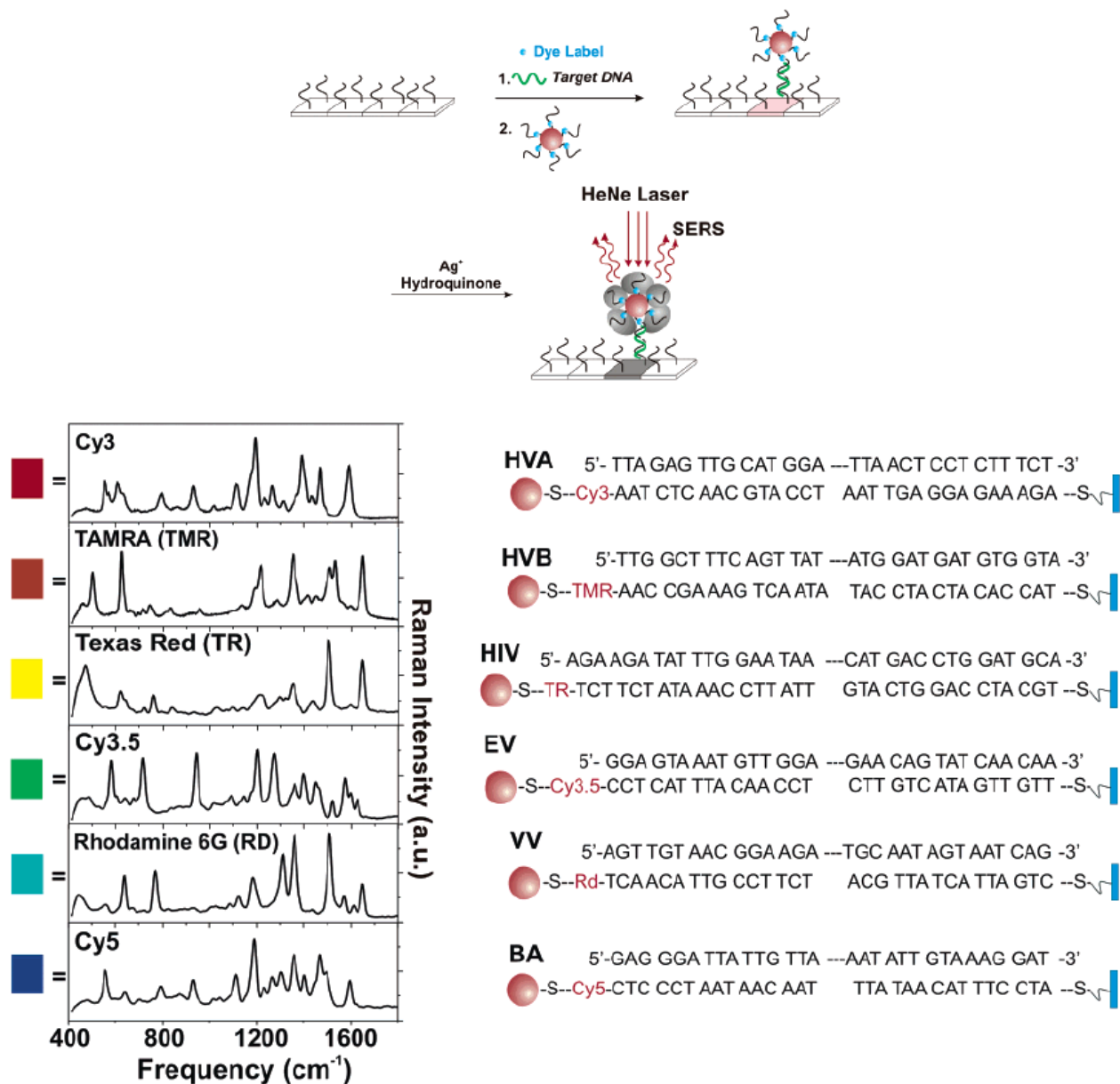


Figure 5. If Raman dyes (blue spheres) are attached to the labeling probe in the scanometric assay, the targets can be encoded and detected via the Raman signal of their labels. (Reprinted with permission from *Science* (<http://www.aaas.org>), ref 68. Copyright 2002 American Association for the Advancement of Science.)

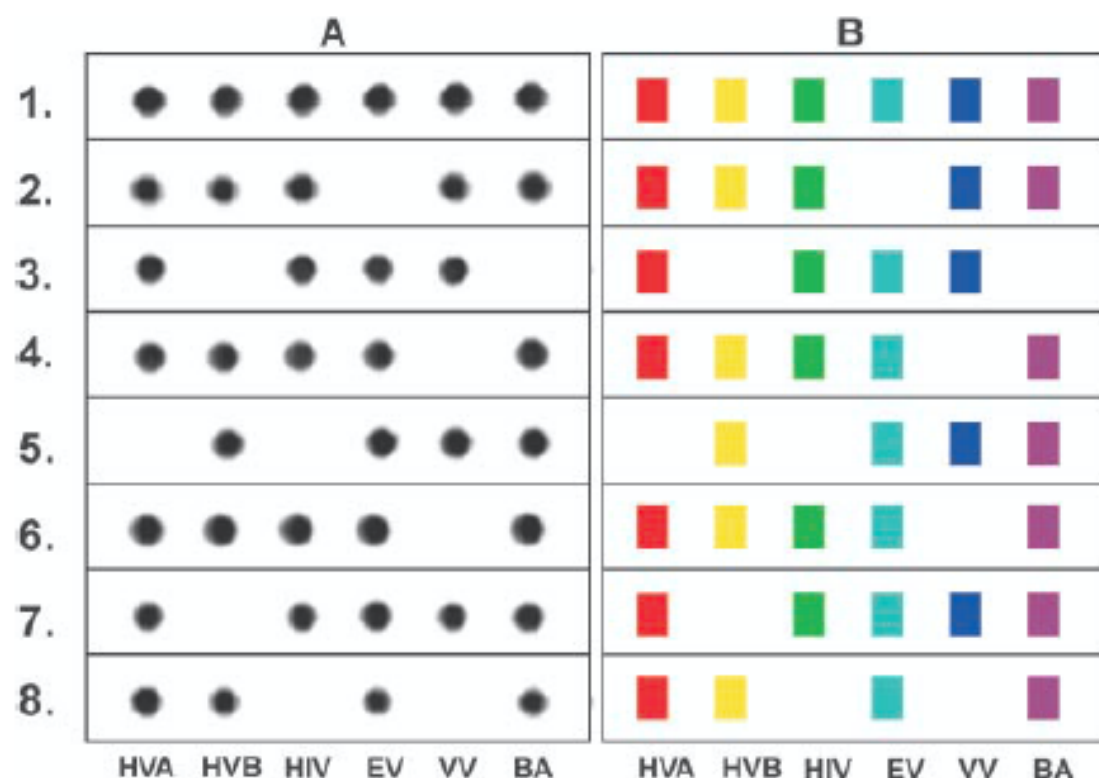


Fig. 3. (A) Flatbed scanner images of Ag-enhanced microarrays and (B) corresponding Raman spectra. The colored boxes correlate with the color-coded Raman spectra in Fig. 2. No false-positives or false-negatives were observed.

Bio-Bar-Code-Based DNA Detection with PCR-like Sensitivity

Jwa-Min Nam, Savka I. Stoeva, and Chad A. Mirkin*

J. AM. CHEM. SOC. 2004, 126, 5932–5933

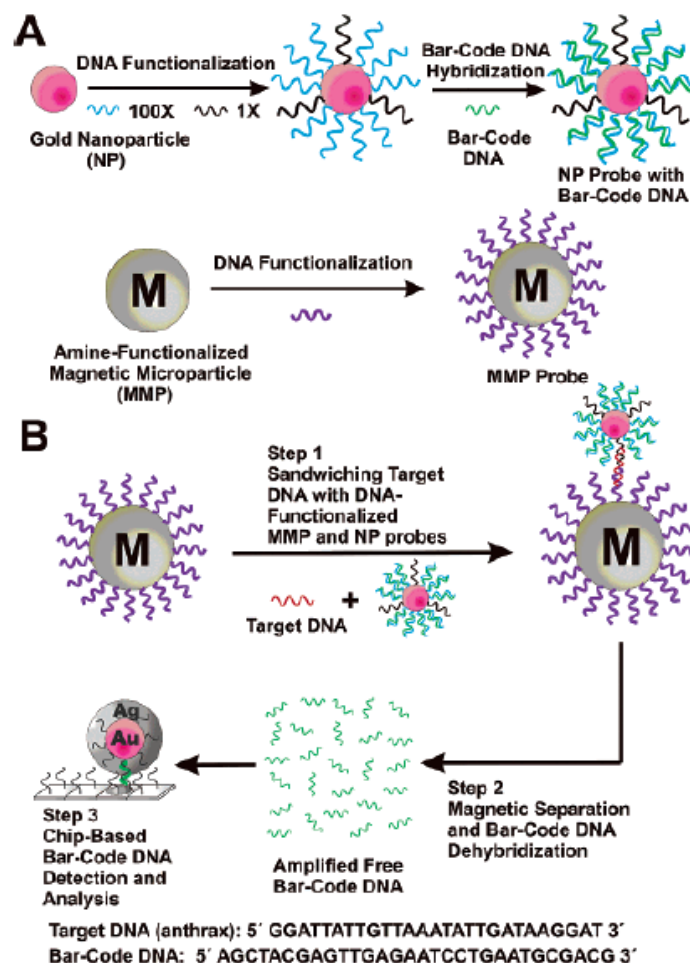


Figure 1. The DNA-BCA assay. (A) Nanoparticle and magnetic micro-particle probe preparation. (B) Nanoparticle-based PCR-less DNA amplification scheme.

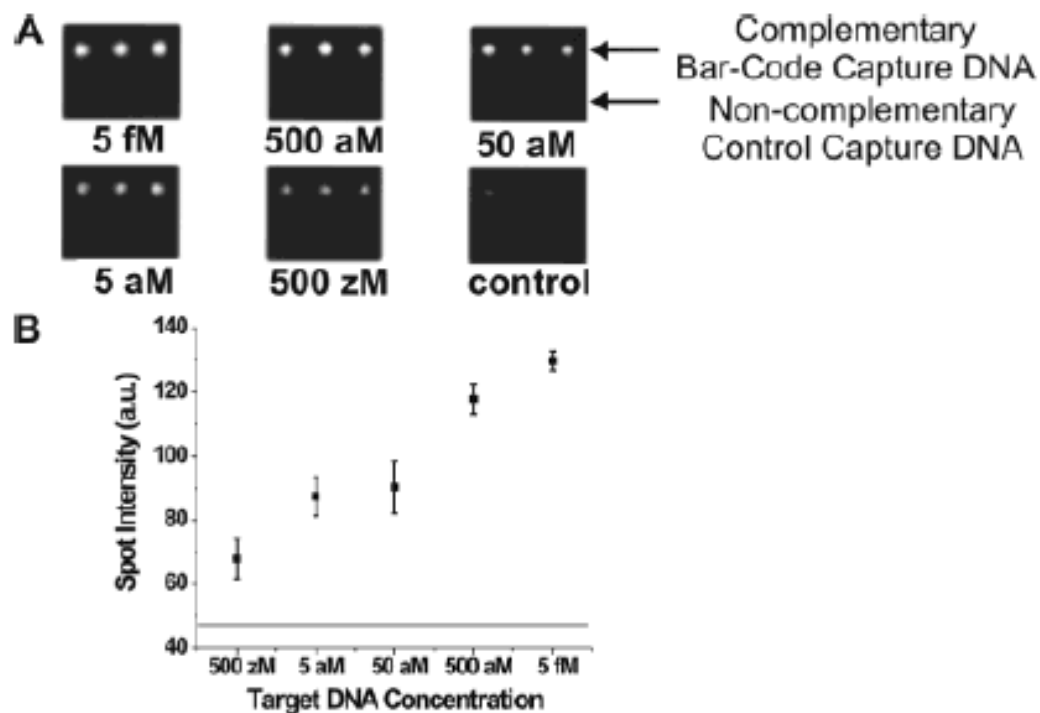


Figure 2. Amplified anthrax bar-code DNA detection with the Verigene ID system. (A) Anthrax bar-code DNA detection with 30 nm NP probes. (B) Quantitative data of spot intensities with 30 nm NP probes (Adobe Photoshop, Adobe Systems, Inc., San Jose, CA). The horizontal line represents control signal intensity (47 ± 2).

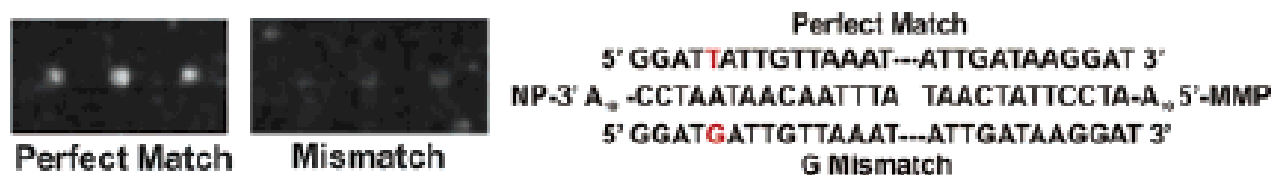


Figure 3. Single base mismatch experiment.

Nanoparticle-Based Bio-Bar Codes for the Ultrasensitive Detection of Proteins

26 SEPTEMBER 2003 VOL 301 SCIENCE

Jwa-Min Nam,* C. Shad Thaxton,* Chad A. Mirkin†

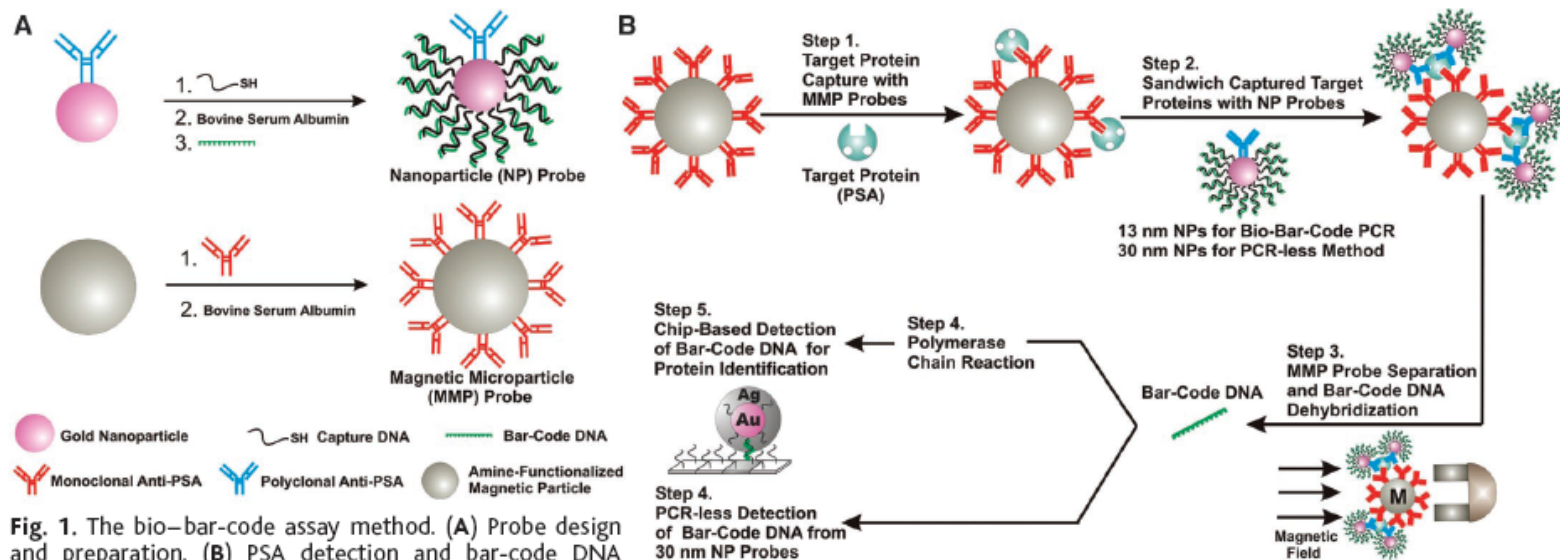


Fig. 1. The bio-bar-code assay method. (A) Probe design and preparation. (B) PSA detection and bar-code DNA amplification and identification. In a typical PSA-detection experiment, an aqueous dispersion of MMP probes functionalized with mAbs to PSA (50 μ l of 3 mg/ml magnetic probe solution) was mixed with an aqueous solution of free PSA (10 μ l of PSA) and stirred at 37°C for 30 min (Step 1). A 1.5-ml tube containing the assay solution was placed in a BioMag microcentrifuge tube separator (Polysciences, Incorporated, Warrington, PA) at room temperature. After 15 s, the MMP-PSA hybrids were concentrated on the wall of the tube. The supernatant (solution of unbound PSA molecules) was removed, and the MMPs were resuspended in 50 μ l of 0.1 M phosphate-buffered saline (PBS) (repeated twice). The NP probes (for 13-nm NP probes, 50 μ l at 1 nM; for 30-nm NP probes, 50 μ l at 200 pM), functionalized with polyclonal Abs to PSA and hybridized bar-code DNA strands, were then added to the assay solution. The NPs reacted with the PSA immobilized on the MMPs and provided DNA strands for signal amplification and protein identification (Step 2). This solution was vigorously stirred at 37°C for 30 min. The MMPs were then washed with 0.1 M PBS with the magnetic separator to isolate the mag-

netic particles. This step was repeated four times, each time for 1 min, to remove everything but the MMPs (along with the PSA-bound NP probes). After the final wash step, the MMP probes were resuspended in NANOpure water (50 μ l) for 2 min to dehybridize bar-code DNA strands from the nanoparticle probe surface. Dehybridized bar-code DNA was then easily separated and collected from the probes with the use of the magnetic separator (Step 3). For bar-code DNA amplification (Step 4), isolated bar-code DNA was added to a PCR reaction mixture (20- μ l final volume) containing the appropriate primers, and the solution was then thermally cycled (20). The bar-code DNA amplicon was stained with ethidium bromide and mixed with gel-loading dye (20). Gel electrophoresis or scanometric DNA detection (24) was then performed to determine whether amplification had taken place. Primer amplification was ruled out with appropriate control experiments (20). Notice that the number of bound NP probes for each PSA is unknown and will depend upon target protein concentration.

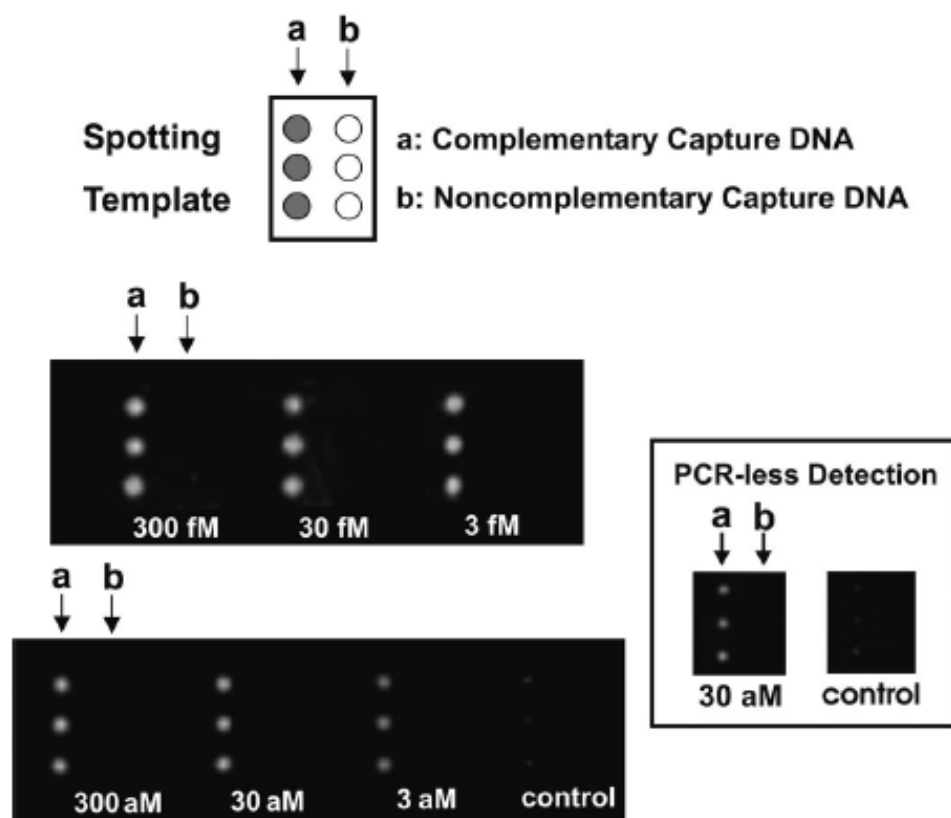


Fig. 2. Scanometric detection of PSA-specific bar-code DNA. PSA concentration (sample volume of 10 μ l) was varied from 300 fM to 3 aM and a negative control sample where no PSA was added (control) is shown. For all seven samples, 2 μ l of antidi-nitrophenyl (10 pM) and 2 μ l of β -galactosidase (10 pM) were added as background proteins. Also shown is PCR-less detection of PSA (30 aM and control) with 30 nm NP probes (inset). Chips were imaged with the Verigene ID system (20).

Table 1. Detection Limits of Nucleic Acid Assays^a

	assay	ss DNA	PCR products	genomic DNA
nanostructure-based methods	colorimetric ²⁹ (cross-linked Au nanoparticles)	~10 nM		
	colorimetric ³⁶ (non-cross-linked Au nanoparticles)	60 nM		
	magnetic relaxation ⁹⁷ (iron oxide nanoparticles)	20 pM		
	electrochemical ⁹⁶ (nanoparticles)	270 pM		
	scanometric ^{35,66,67} (Au nanoparticles with Ag amplification)	50 fM	100 aM ^b	200 fM
	Raman spectroscopy ⁶⁸ (Au nanoparticles with Ag amplification)	~1 fM		
	electrical ⁹³ (Au nanoparticles with Ag amplification)	500 fM		
	electrical ⁹⁹ (Si nanowire)	10 fM		
	electrical ¹⁰³ (carbon nanotube)	54 aM		
	resonant light-scattering ^{61–66} (metal nanoparticles)	170 fM ^b		33 fM
	fluorescence ⁵⁶ (ZnS and CdSe quantum dots)	2 nM		
	surface plasmon resonance ⁴¹ (Au nanoparticles)	10 pM		
	quartz crystal microbalance ⁹⁴ (Au nanoparticles)	~1 fM		
	laser diffraction ⁴² (Au nanoparticles)	~50 fM		
	fluorescence ⁴⁵ (fluorescent nanoparticles)	~1 fM		
	bio-bar-code amplification ⁷¹ (Au nanoparticles with Ag amplification)	500 zM		
other non-enzymatic based methods	fluorescence ³⁵ (molecular fluorophores)		~600 fM ^b	
	fluorescence (dendrimer amplification) ¹³⁴		2.5 μ g	
	electrochemical amplification ¹³⁶ (electroactive reporter molecules)	100 aM		

^a Detection limits can vary based on target length and sequence; therefore, it is difficult to compare assays without testing them using identical targets and conditions. ^b Values taken from ref 34.

Table 2. Detection Limits of Protein Assays

	assay	target	protein in saline	protein in serum
nanostructure-based methods	optical ⁷² (Au nanoshells)	rabbit IgG	0.88 ng/mL (~4.4 pM) ^a	0.88 ng/mL (~4.4 pM) ^a
	optical ⁷⁴ (Au nanoparticles)	IgE and IgG1	~20 nM	
	magnetic relaxation ⁹⁸ (iron oxide nanoparticles)	adenovirus (ADV) and herpes simplex virus (HSV)	100 ADV/ 100 μ L	50 HSV/ 100 μ L
	scanometric ⁷⁹ (Au nanoparticles with Ag amplification)	mouse IgG	200 pM	
	Raman ⁸² (Au nanoparticles with Raman labels)	prostate-specific antigen		30 fM
	surface plasmon resonance ^{83,84} (triangular Ag particles on surfaces)	streptavidin(S A) and anti-biotin (AB)	~1 pM SA and ~700 pM AB	
	electrical ¹¹⁰ (single-walled carbon nanotubes)	10E3 antibody to U1A RNA splicing factor	~1 nM	
	electrical ²⁰ (Si nanowires) bio-bar-code amplification ⁷⁵ (Au nanoparticles with Ag amplification)	streptavidin prostate-specific antigen	10 pM 30 aM (3 aM) ^b	(30 aM) ^b
molecular fluorophore methods	enzyme-linked immunosorbent assay	various	pM range	pM range
electrochemical methods	electrochemical amplification ¹³⁷ (oligonucleotide reporter molecules)	IgG	13 fM	
enzyme-based amplification methods	immuno-PCR ⁷⁶	bovine serum albumin	2 fM	
	rolling circle amplification ⁷⁷	prostate-specific antigen	3 fM	

^a Reported in ng/mL; authors converted to molar concentration for ease of comparison. ^b These values are the lower limits when PCR is used to amplify the bar-code DNA prior to scanometric detection of bar codes.

Surface Plasmon

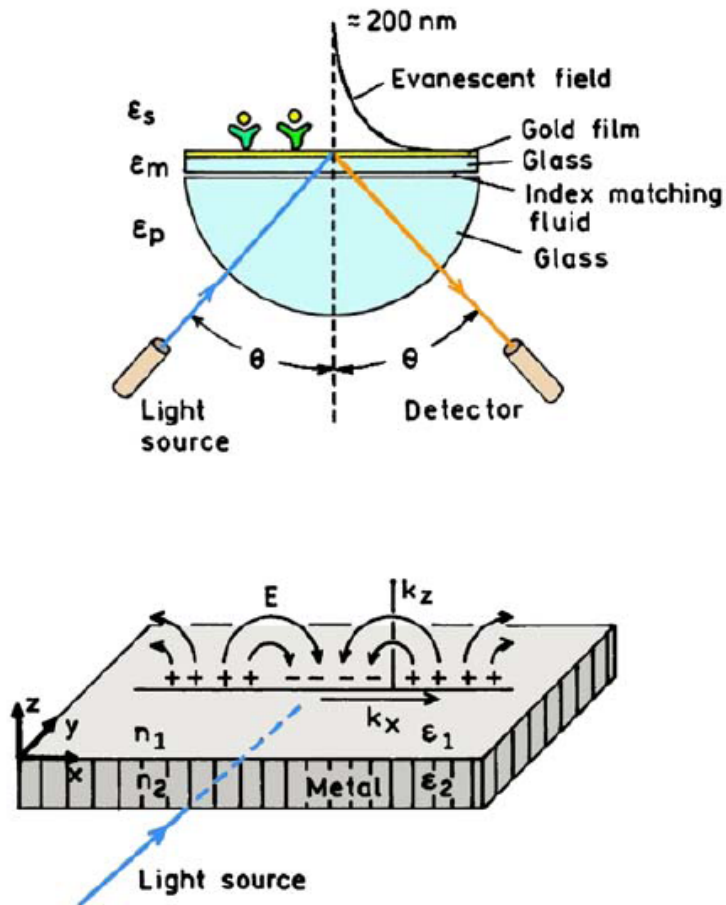
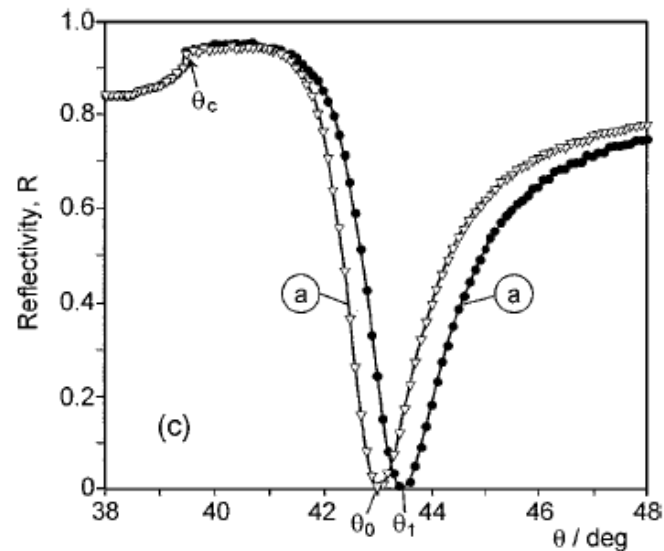
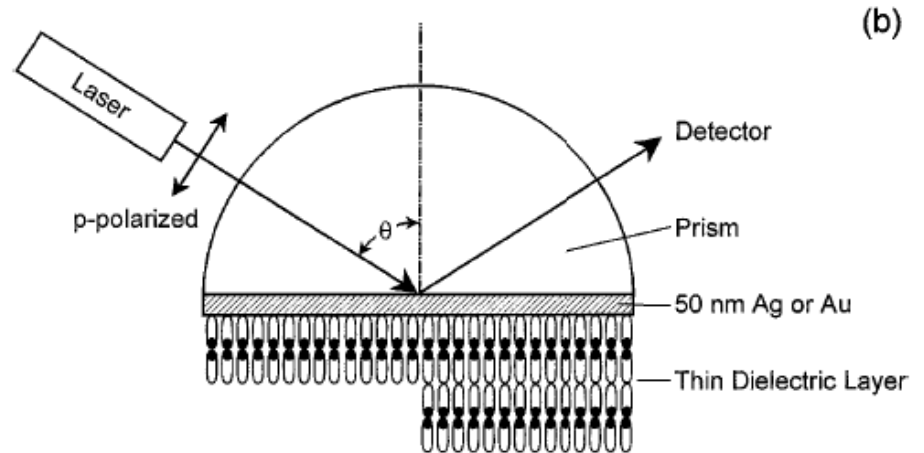
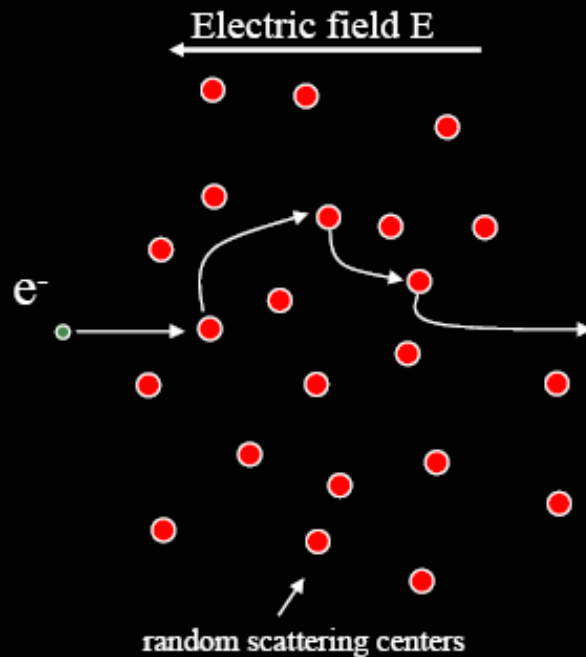


Figure 3. Schematics of an SPR experiment (top) and of the light-induced surface plasmons (bottom).



Drift: Drude model



$$F = ma$$

$$eE = m \frac{\partial v}{\partial t}$$

$$v_{avg} = \underbrace{\frac{e\tau}{m}}_{\mu} E$$

$$j = ne v_{avg} = \underbrace{\frac{ne^2\tau}{m}}_{\sigma} E$$

$$m \frac{\partial}{\partial t} \langle \vec{v} \rangle = q \vec{E} - \gamma \langle \vec{v} \rangle$$

$$\sigma(\omega) = \frac{\sigma_0}{1 + i\omega\tau}$$

AC Dielectric Response

$$\epsilon_m = 1 - \frac{\omega_p^2}{\omega^2} \quad \text{Plasma frequency}$$

polarizability of a small metal sphere with dielectric function $\epsilon(\lambda)$

$$\alpha = R^3 \frac{\epsilon - 1}{\epsilon + 2}.$$

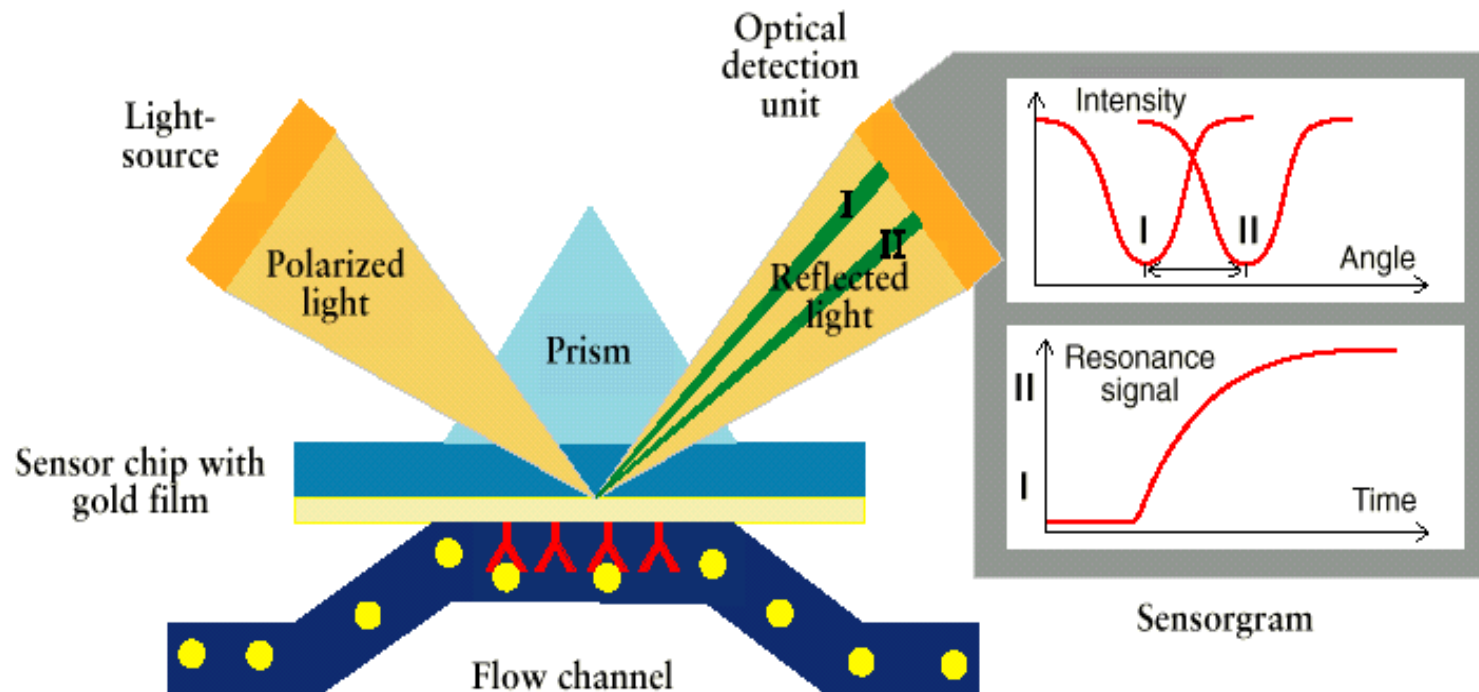
$$\epsilon = \epsilon_b + 1 - \frac{\omega_p^2}{\omega^2 + i\omega\gamma},$$

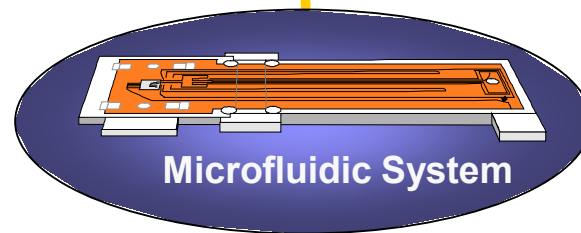
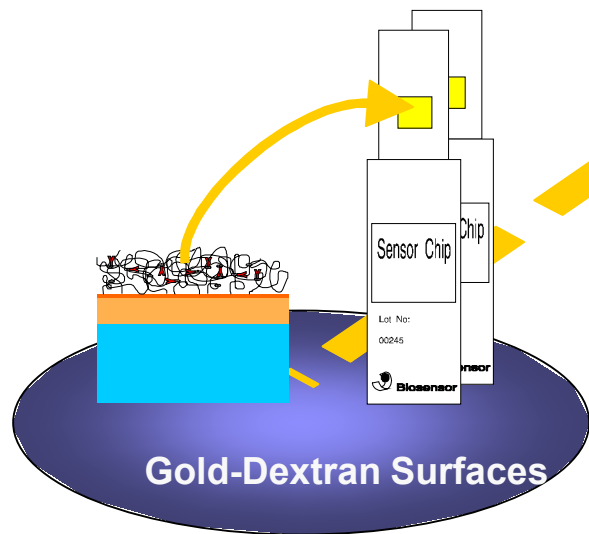
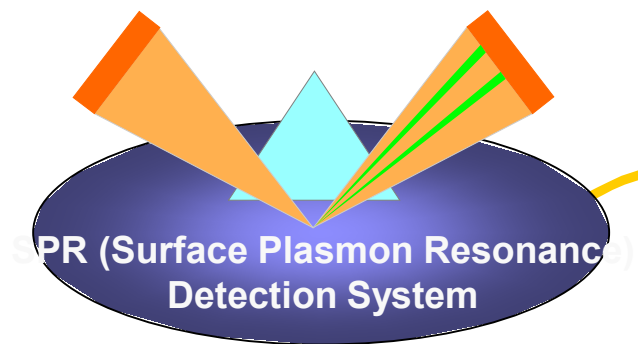
$$\alpha = \frac{R^3(\epsilon_b\omega^2 - \omega_p^2) + i\omega\gamma\epsilon_b}{[(\epsilon_b + 3)\omega^2 - \omega_p^2] + i\omega\gamma(\epsilon_b + 3)}.$$

$$\omega_R = \frac{\omega_p}{\sqrt{\epsilon_b + 3}} \quad \gamma(\epsilon_b + 3).$$

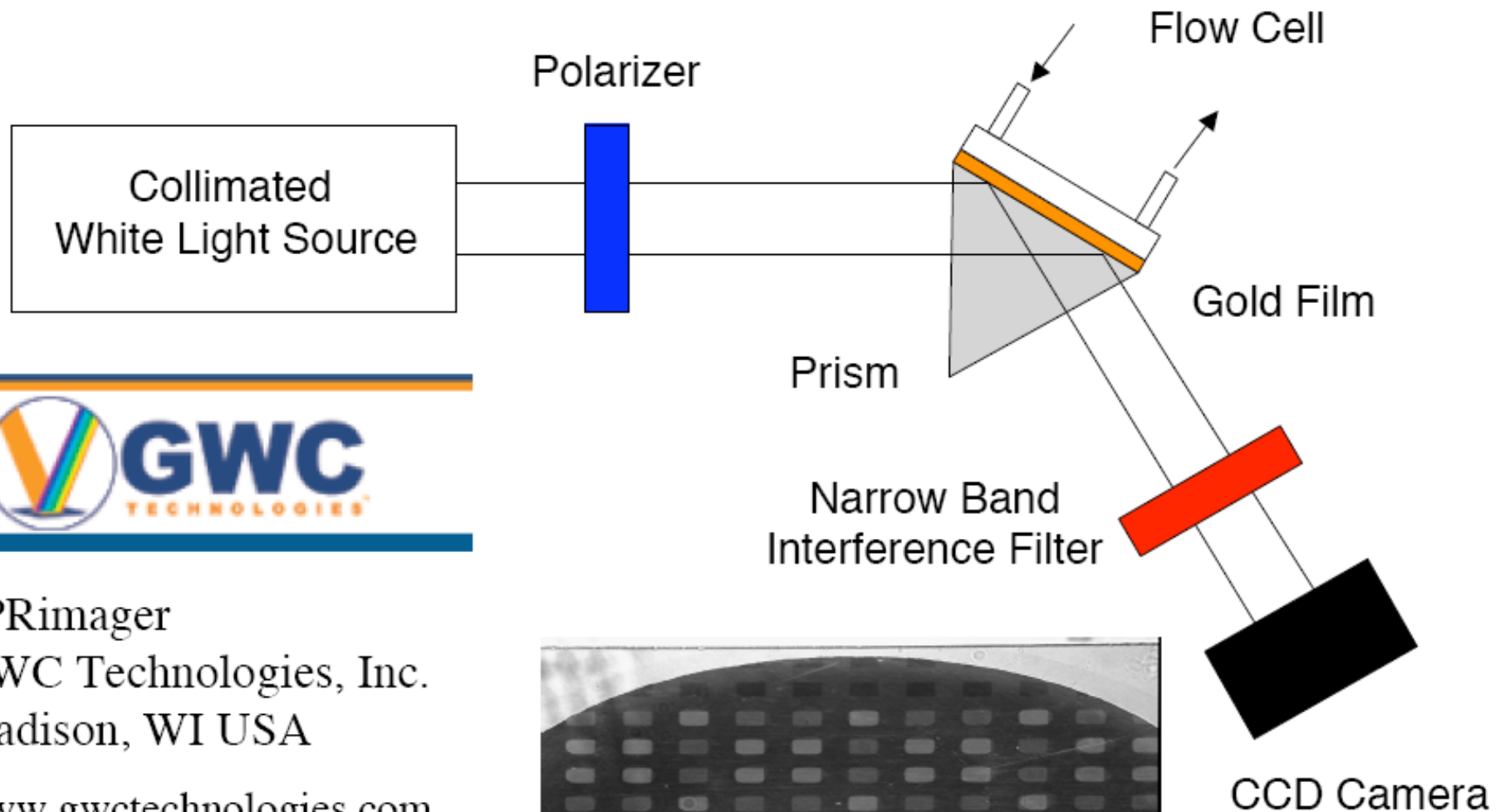
Biomolecular Binding in Real Time

Principle of Detection - SPR (Surface Plasmon Resonance)



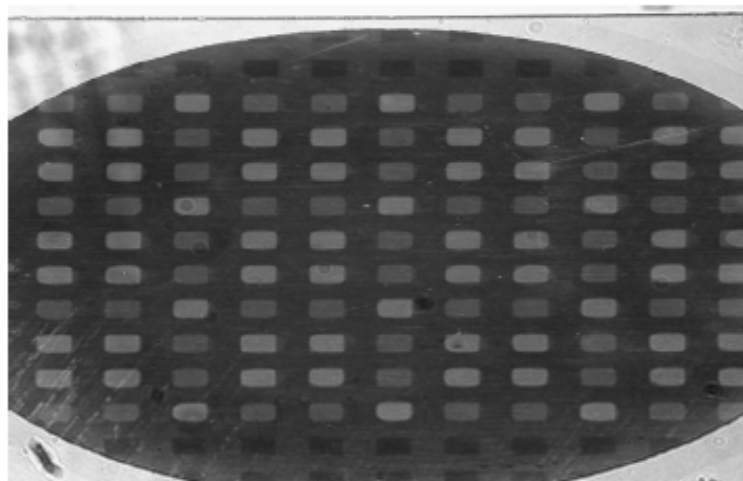


SPR Imaging Apparatus



SPRImager
GWC Technologies, Inc.
Madison, WI USA
www.gwctechnologies.com

Raw Image



Localized Plasmon

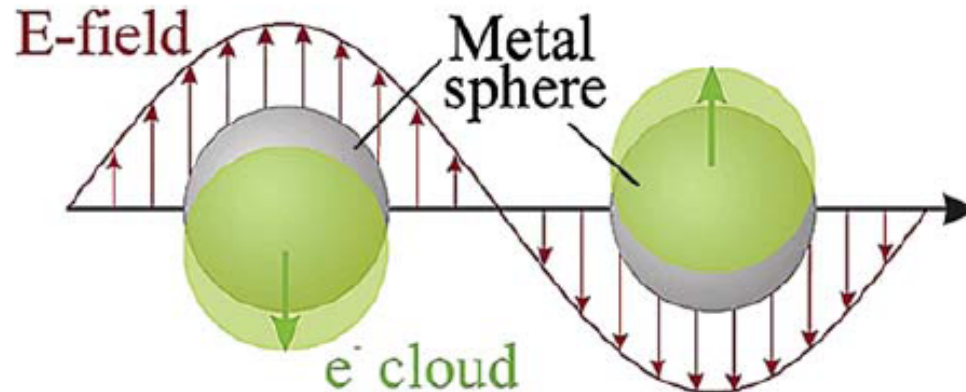
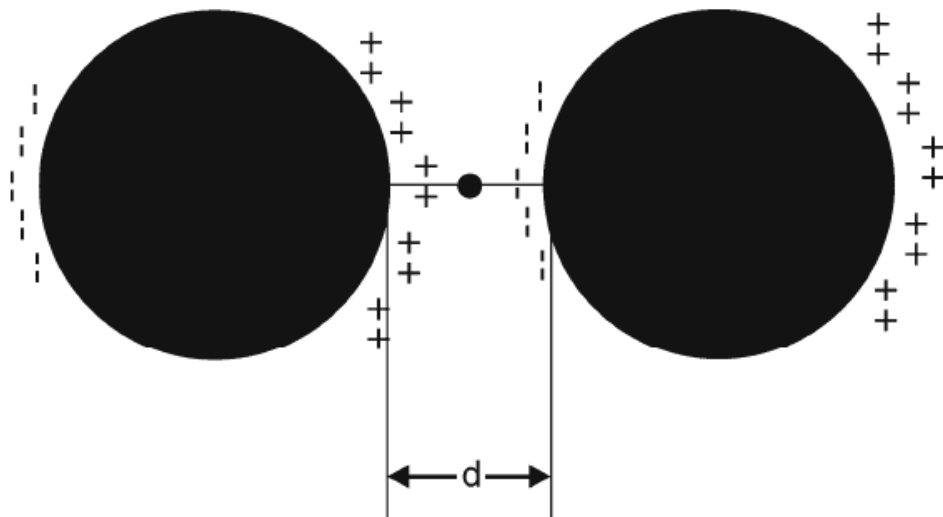
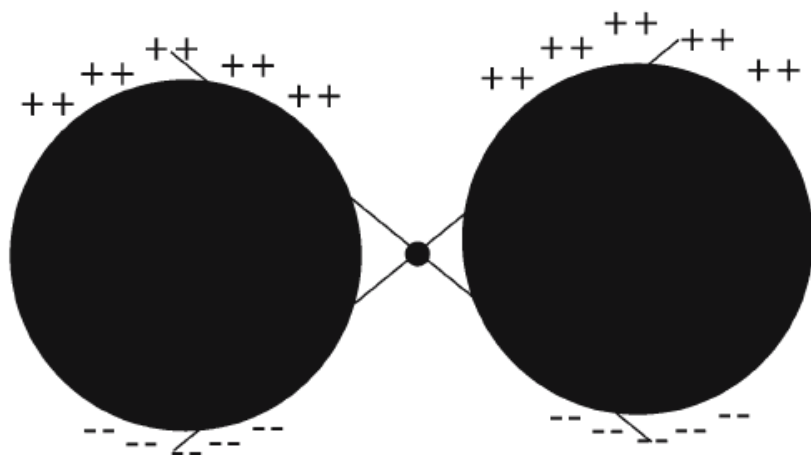


Figure 6. Schematic of plasmon oscillation for a sphere. From [39].



field enhancement

$E_s = gE_0$, where E_0 is the magnitude of the incident field

$$E_R \propto \alpha_R E_s \propto \alpha_R g E_0$$

$$E_{\text{SERS}} \propto \alpha_R g g' E_0$$

$$I_{\text{SERS}} \propto |\alpha_R|^2 |g g'|^2 I_0$$

$$g \cong g'$$

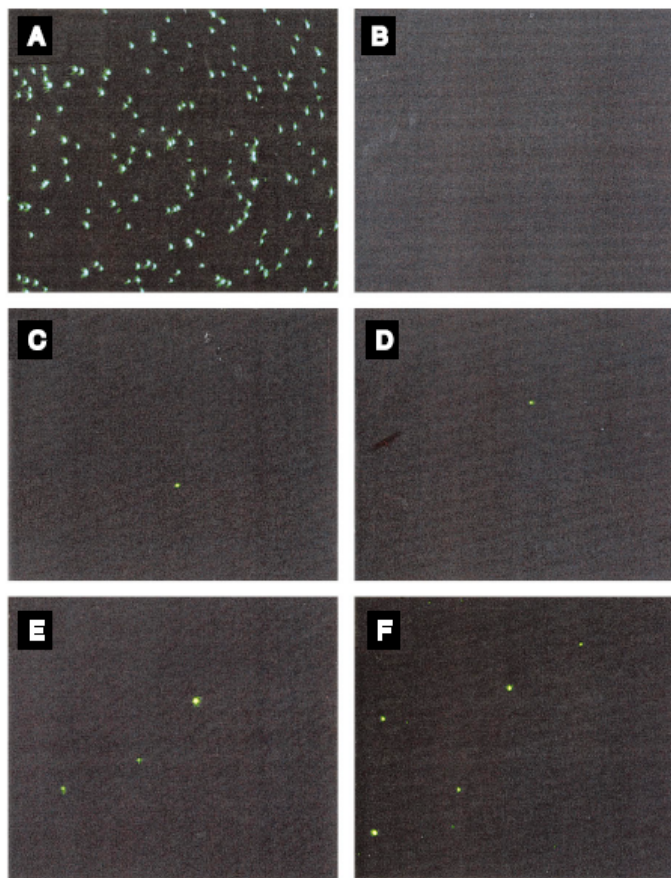
$$|E_L|^4 = |g|^4.$$

Probing Single Molecules and Single Nanoparticles by Surface-Enhanced Raman Scattering

SCIENCE • VOL. 275 • 21 FEBRUARY 1997

Shuming Nie* and Steven R. Emory

Fig. 1. Single Ag nanoparticles imaged with evanescent-wave excitation. Total internal reflection of the laser beam at the glass-liquid interface was used to reduce the laser scattering background. The instrument setup for evanescent-wave microscopy was adapted from Funatsu *et al.* (11). The images were directly recorded on color photographic film (ASA-1600) with a 30-s exposure by a Nikon 35-mm camera attached to the microscope. (A) Unfiltered photograph showing scattered laser light from all particles immobilized on a polylysine-coated surface. (B) Filtered photographs taken from a blank Ag colloid sample (incubated with 1 mM NaCl and no R6G analyte molecules). (C) and (D) Filtered photographs taken from a Ag colloid sample incubated with 2×10^{-11} M R6G. These images were selected to show at least one Raman scattering particle. Different areas of the cover slip were



rapidly screened, and most fields of view did not contain visible particles. (E) Filtered photograph taken from Ag colloid incubated with 2×10^{-10} M R6G. (F) Filtered photograph taken from Ag colloid incubated with 2×10^{-9} M R6G. A high-performance bandpass filter was used to remove the scattered laser light and to pass Stokes-shifted Raman signals from 540 to 580 nm (920 to 2200 cm^{-1}). Continuous-wave excitation at 514.5 nm was provided by an Ar ion laser. The total laser power at the sample was 10 mW. Note the color differences between the scattered laser light in (A) and the red-shifted light in (C) through (F).

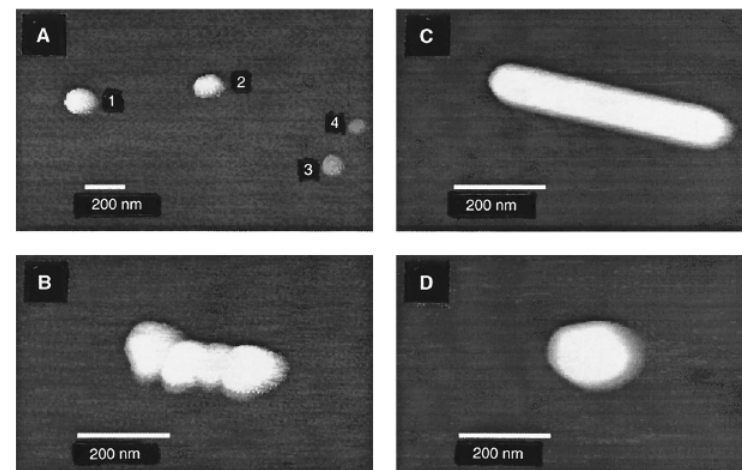
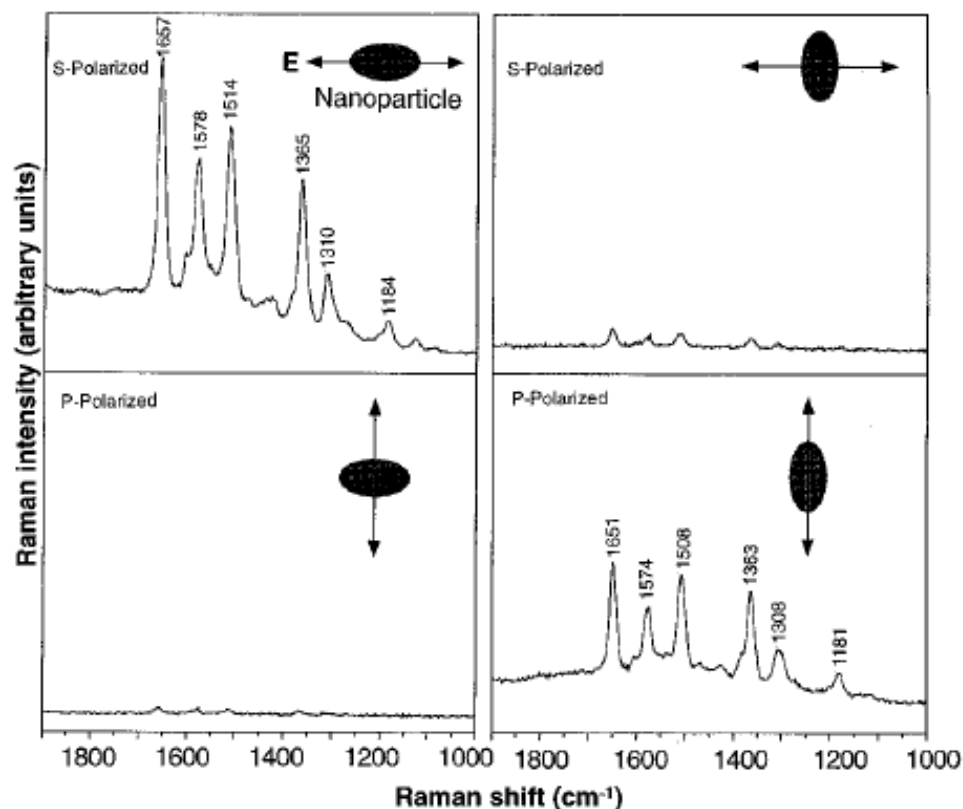


Fig. 2. Tapping-mode AFM images of screened Ag nanoparticles. (A) Large area survey image showing four single nanoparticles. Particles 1 and 2 were highly efficient for Raman enhancement, but particles 3 and 4 (smaller in size) were not. (B) Close-up image of a hot aggregate containing four linearly arranged particles. (C) Close-up image of a rod-shaped hot particle. (D) Close-up image of a faceted hot particle.

Fig. 3. Surface-enhanced Raman spectra of R6G obtained with a linearly polarized confocal laser beam from two Ag nanoparticles. The R6G concentration was 2×10^{-11} M, corresponding to an average of 0.1 analyte molecule per particle. The direction of laser polarization and the expected particle orientation are shown schematically for each spectrum. Laser wavelength, 514.5 nm; laser power, 250 nW; laser focal radius, ~ 250 nm; integration time, 30 s. All spectra were plotted on the same intensity scale in arbitrary units of the CCD detector readout signal.



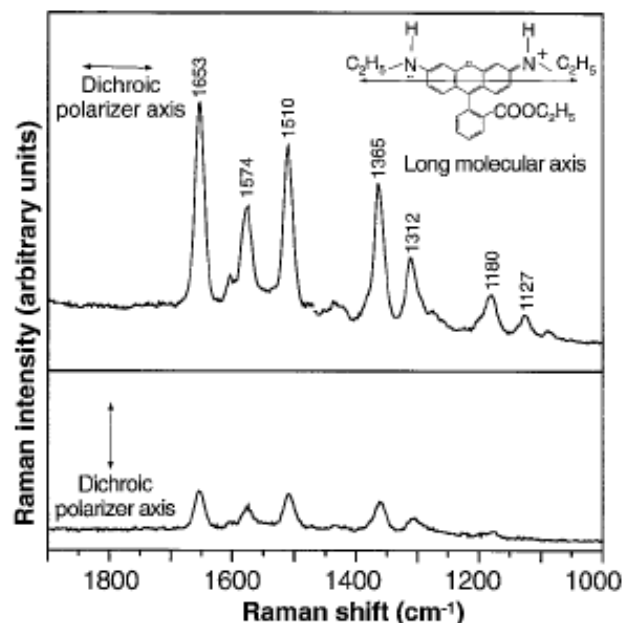


Fig. 4. Emission-polarized surface-enhanced Raman signals of R6G observed from a single Ag nanoparticle with a polarization-scrambled confocal laser beam. A dichroic sheet polarizer was rotated 90° to select Raman scattering signals polarized parallel (upper spectrum) or perpendicular (lower spectrum) to the long molecular axis of R6G. (**Inserts**) Structure of R6G, the electronic transition dipole (along the long axis when excited at 514.5 nm), and the dichroic polarizer orientations. Other conditions as in Fig. 3.

troscopic signatures of adsorbed molecules. For single rhodamine 6G molecules adsorbed on the selected nanoparticles, the intrinsic Raman enhancement factors were on the order of 10^{14} to 10^{15} , much larger than the ensemble-averaged values derived from conventional measurements. This enormous enhancement leads to vibrational Raman signals that are more intense and more stable than single-molecule fluorescence.

Electromagnetic contributions to single-molecule sensitivity in surface-enhanced Raman scattering

PRE 62 4318

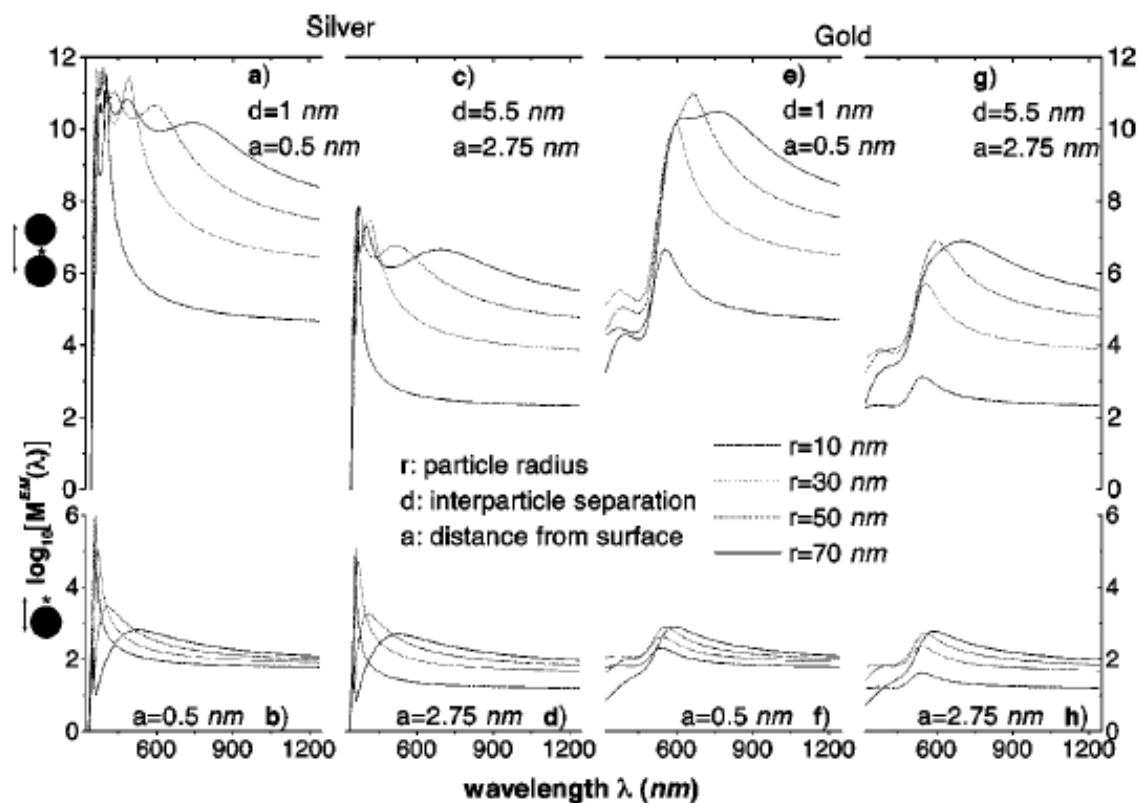




FIG. 3. (Color) EM-enhancement factor M^{EM} at a cross section through six different silver particle configurations. The wavelength of the incident field is $\lambda = 514.5$ nm with vertical polarization. The left-hand column illustrates the EM enhancement for dimer configurations of two spheres (top) and two polygons (bottom) with a separation of 1 nm. The middle column shows the same situation, but with a separation distance of 5.5 nm. The right-hand column shows the case of an isolated single particle. All particles share a common largest dimension of 90 nm. Note that the color scale from dark blue to dark red is logarithmic, covering the interval $10^0 < M^{EM} < 10^8$. Regions with enhancement outside this interval are shown in dark blue and dark red, respectively.

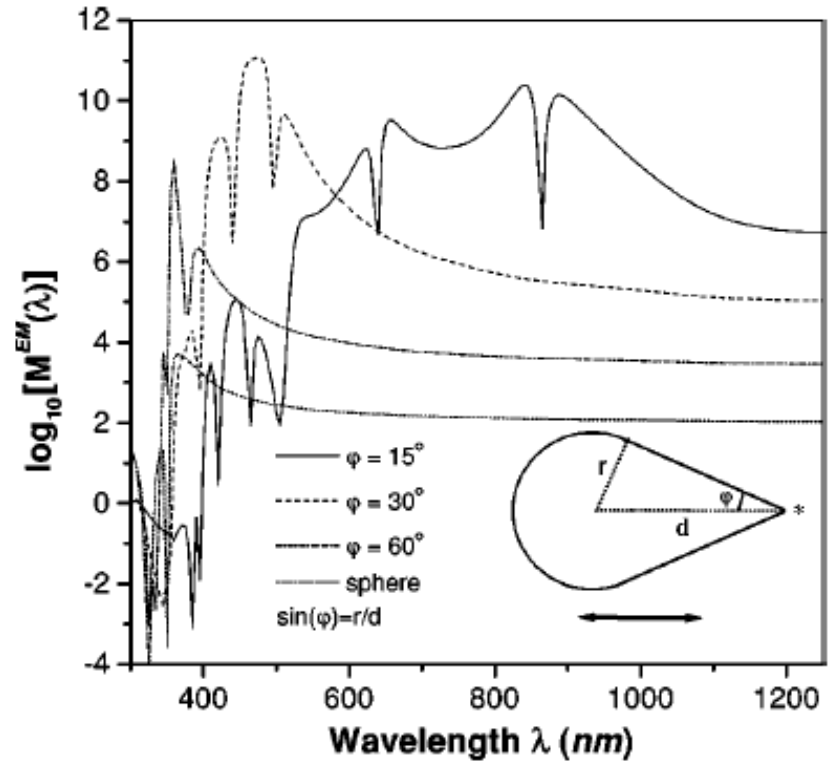


FIG. 5. EM-enhancement factor for a rotationally symmetric silver droplet as a function of the angle defining the opening edge ϕ . The field is polarized parallel to the axis of the droplet and the evaluation position (star) is located 0.5 nm outside the tip. As the droplet becomes sharper the enhancement increases several orders of magnitude.

Nanosphere Arrays with Controlled Sub-10-nm Gaps as Surface-Enhanced Raman Spectroscopy Substrates

J. AM. CHEM. SOC. 2005, 127, 14992–14993

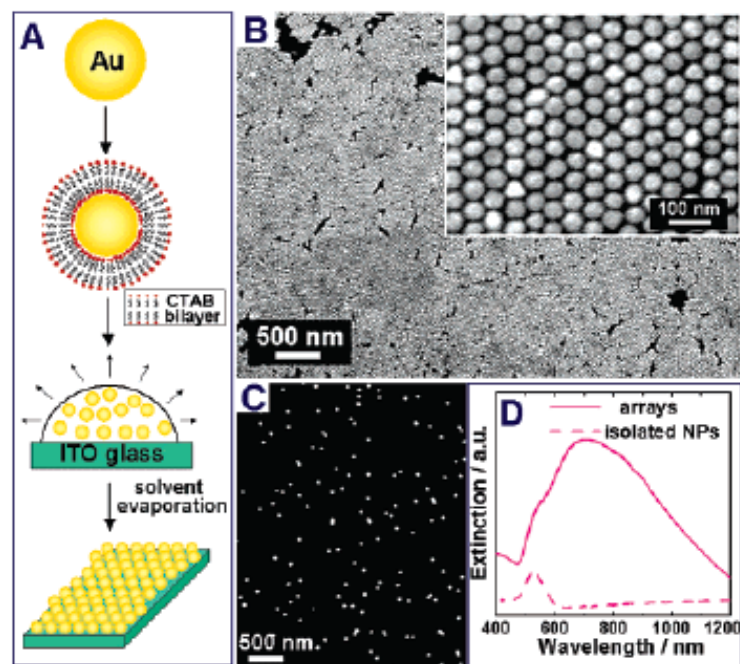


Figure 1. (A) Schematic illustration of the fabrication of sub-10-nm gap Au NP arrays. (B) SEM image of the arrays. (C) SEM image of monolayer of isolated Au NPs on ITO glass. (D) Vis-NIR extinction spectrum of the monolayer of isolated Au NPs and arrays.

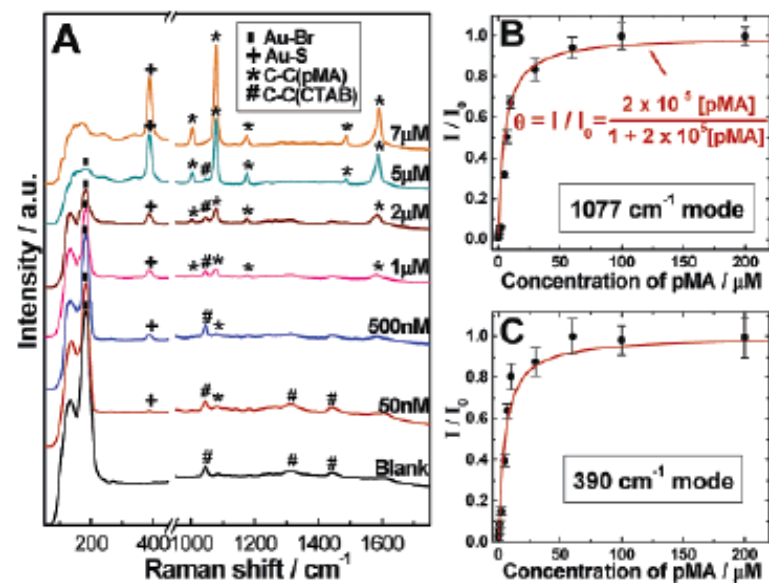
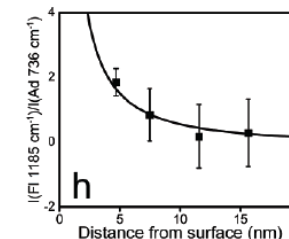
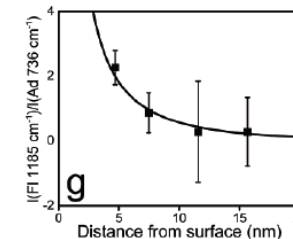
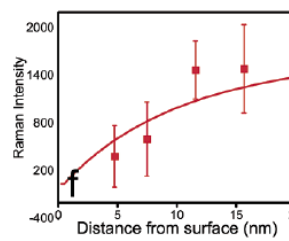
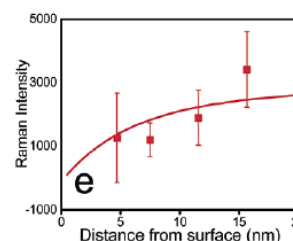
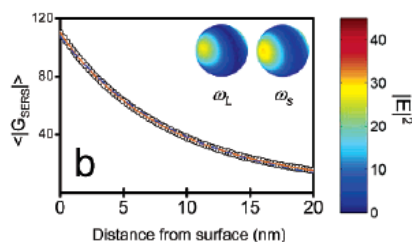
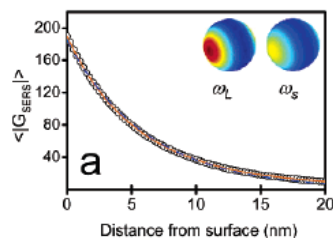
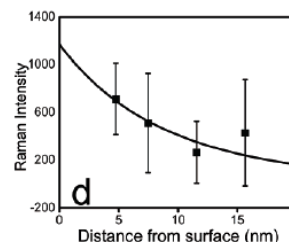
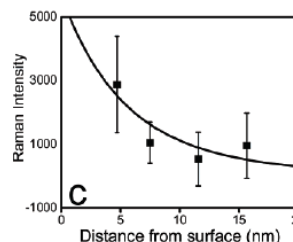
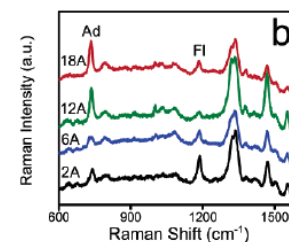
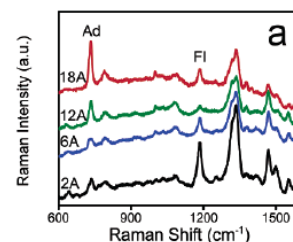
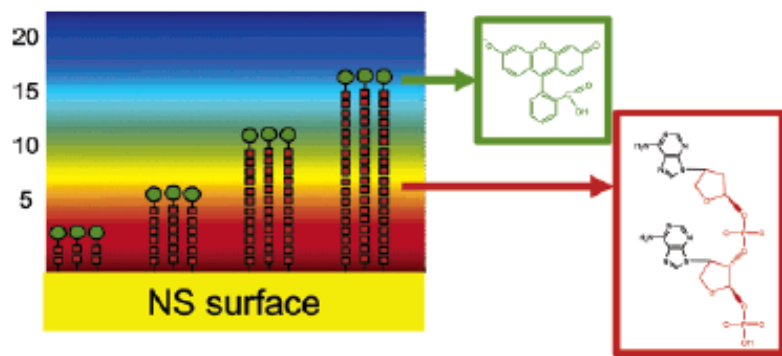


Figure 2. (A) SERS spectra of 5 μL of pMA with different concentrations deposited on the NP arrays. The excitation laser wavelength is 785 nm. Adsorption isotherm of pMA on the NP arrays obtained according to (B) 1077 and (C) 390 cm^{-1} modes in the SERS spectra. I_0 is the peak intensity of a saturated pMA monolayer.

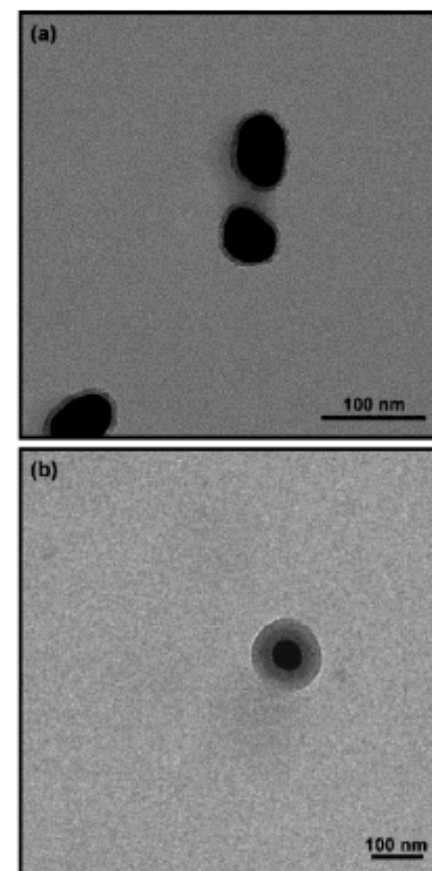
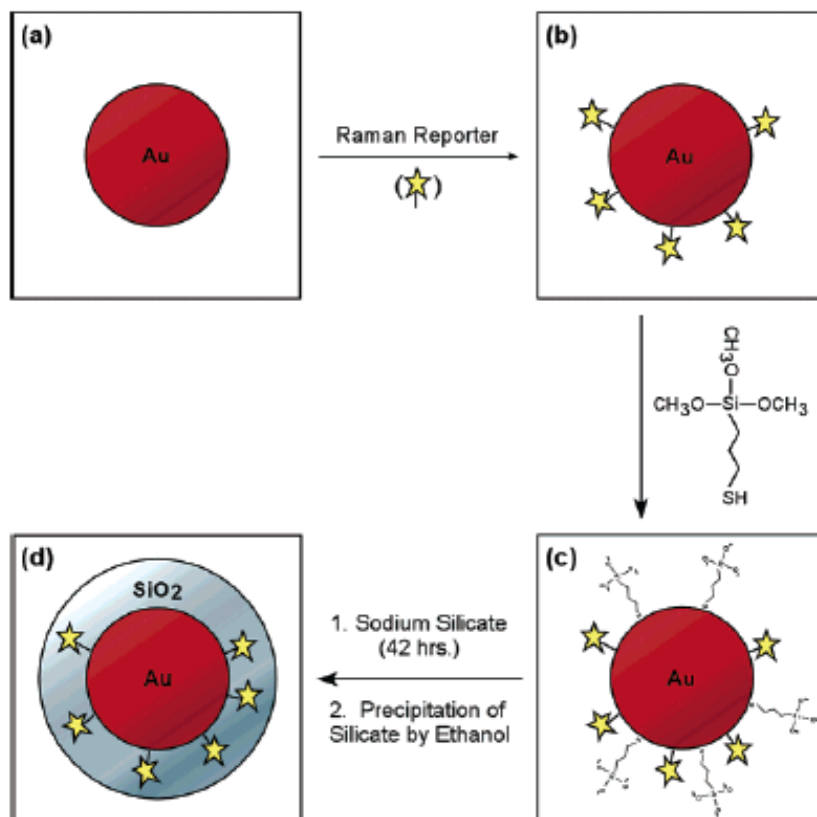
Profiling the Near Field of a Plasmonic Nanoparticle with Raman-Based Molecular Rulers

NANO
LETTERS

2006
Vol. 6, No. 10
2338–2343



Spectroscopic Tags Using Dye-Embedded Nanoparticles and Surface-Enhanced Raman Scattering



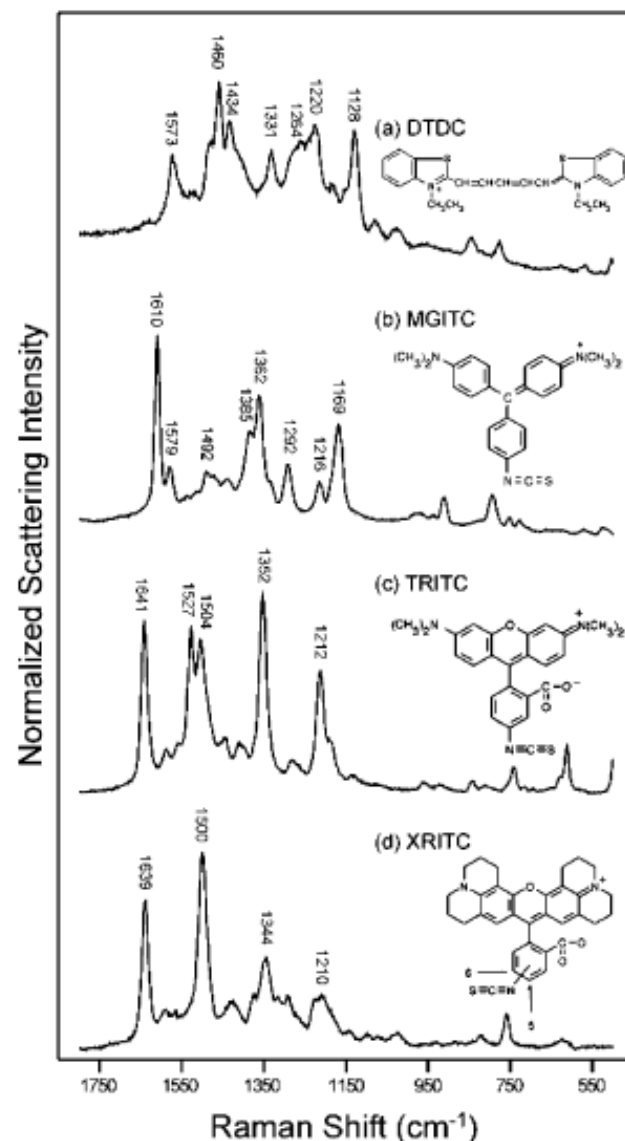
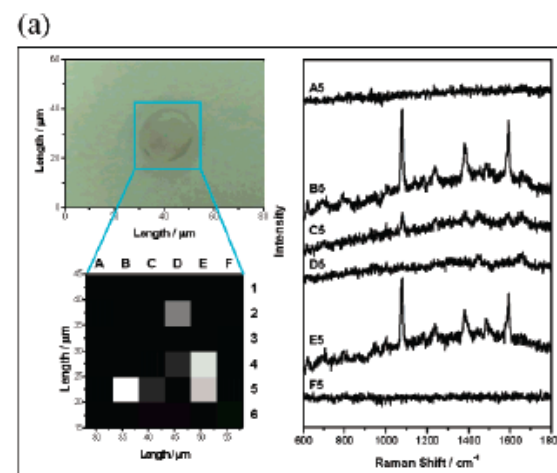
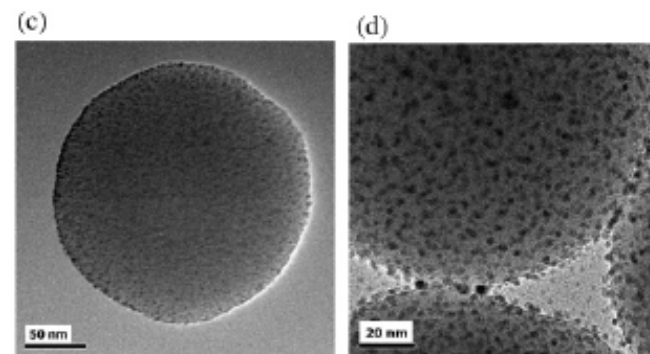
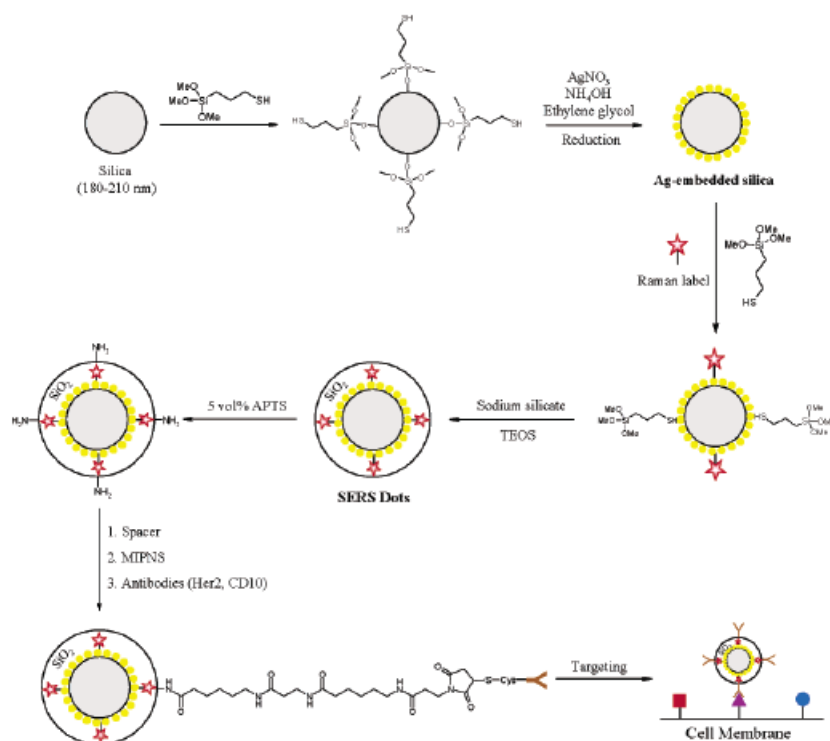
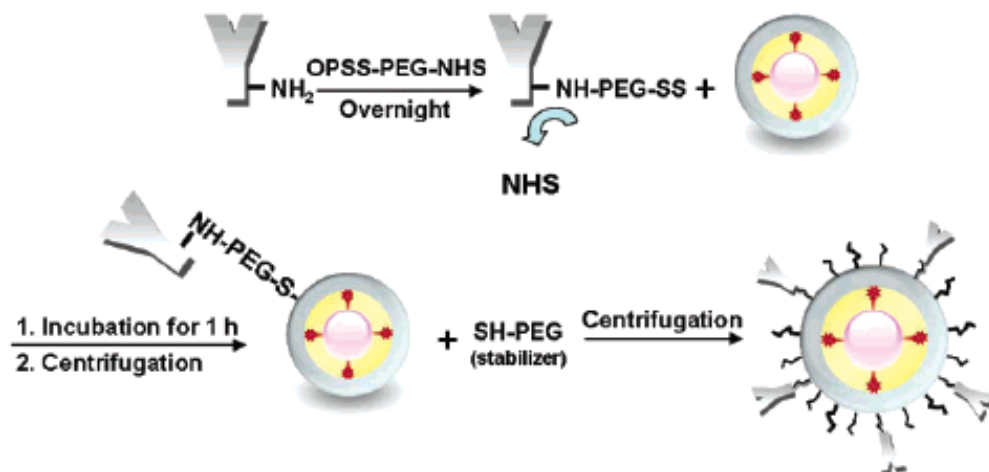
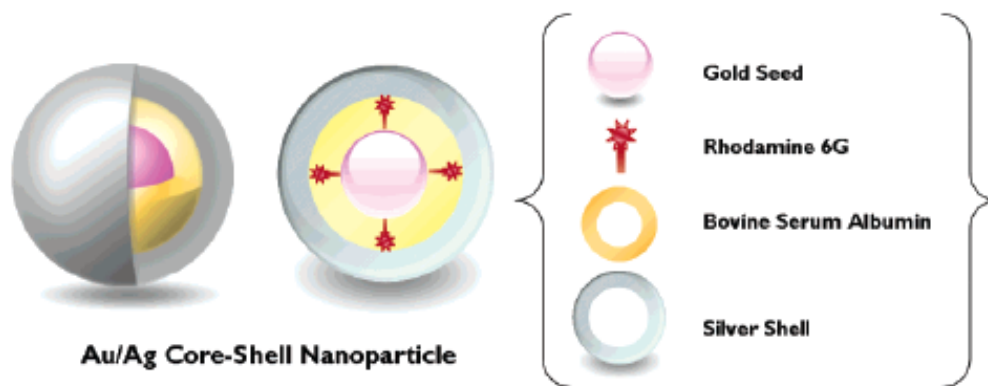


Figure 4. Chemical structures of four Raman reporters and their surface-enhanced resonance Raman spectra: (a) 3,3'-Diethylthiadicarbocyanine iodide (DTDC); (b) malachite green isothiocyanate (MGITC); (c) tetramethylrhodamine-5-isothiocyanate (TRITC); and (e) rhodamine-5-(and-6)-isothiocyanate (XRITC).

Nanoparticle Probes with Surface Enhanced Raman Spectroscopic Tags for Cellular Cancer Targeting



Biological Imaging of HEK293 Cells Expressing PLC γ 1 Using Surface-Enhanced Raman Microscopy



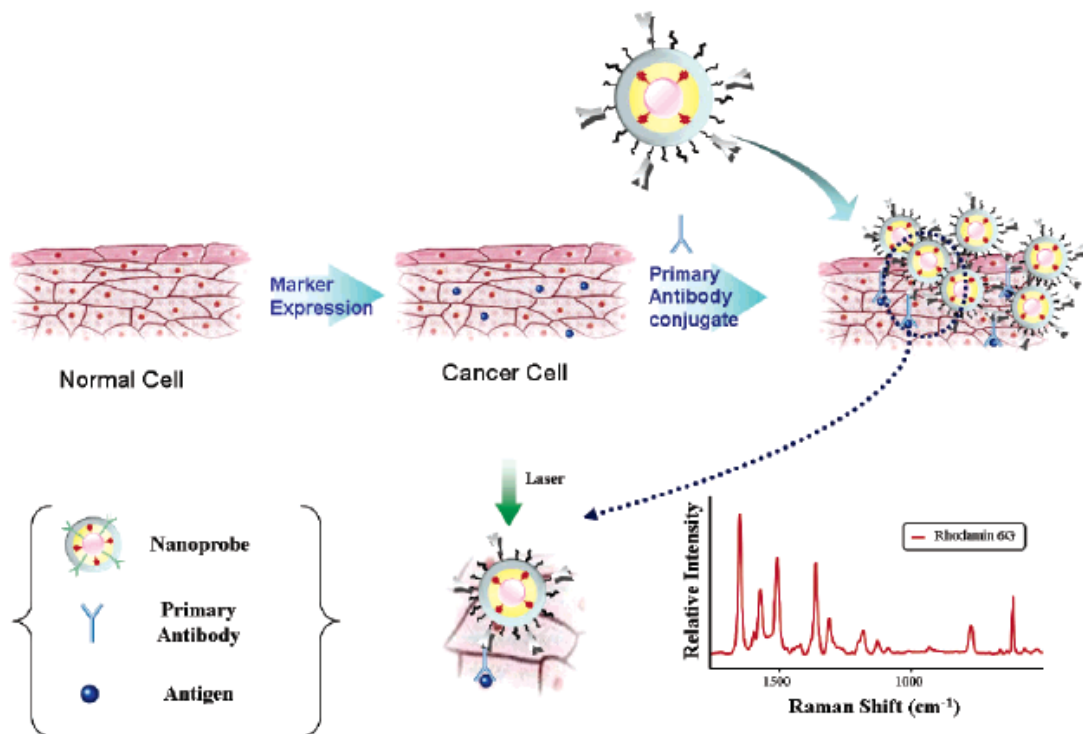


Figure 4. Schematic diagram depicting immobilization of Au/Ag core-shell nanoprobe on PLC γ 1-expressing HEK293 cells and their SERS detection.

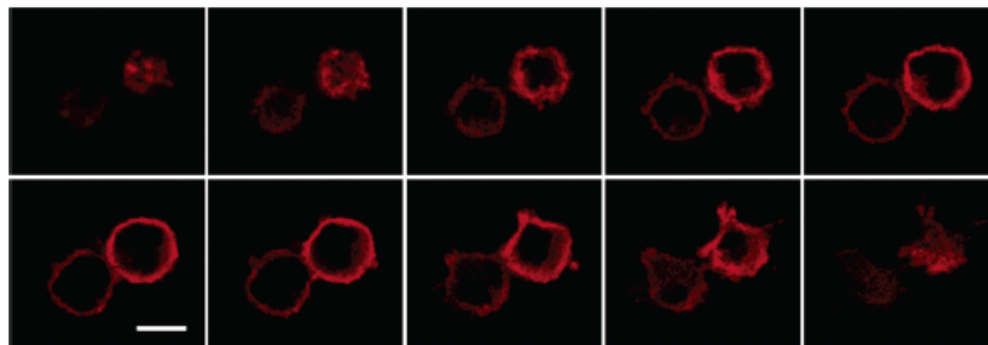


Figure 5. Serial fluorescence optical sections of PLC γ 1-expressing HEK293 cells using red QDs. The z-axis interval of optical slices is 1.3 μ m. Cells were incubated for 30 min in red QDs, after which the free QDs were washed away. These fluorescence images indicate that PLC γ 1 markers are only expressed on the surface membranes. Scale bar, 10 μ m.

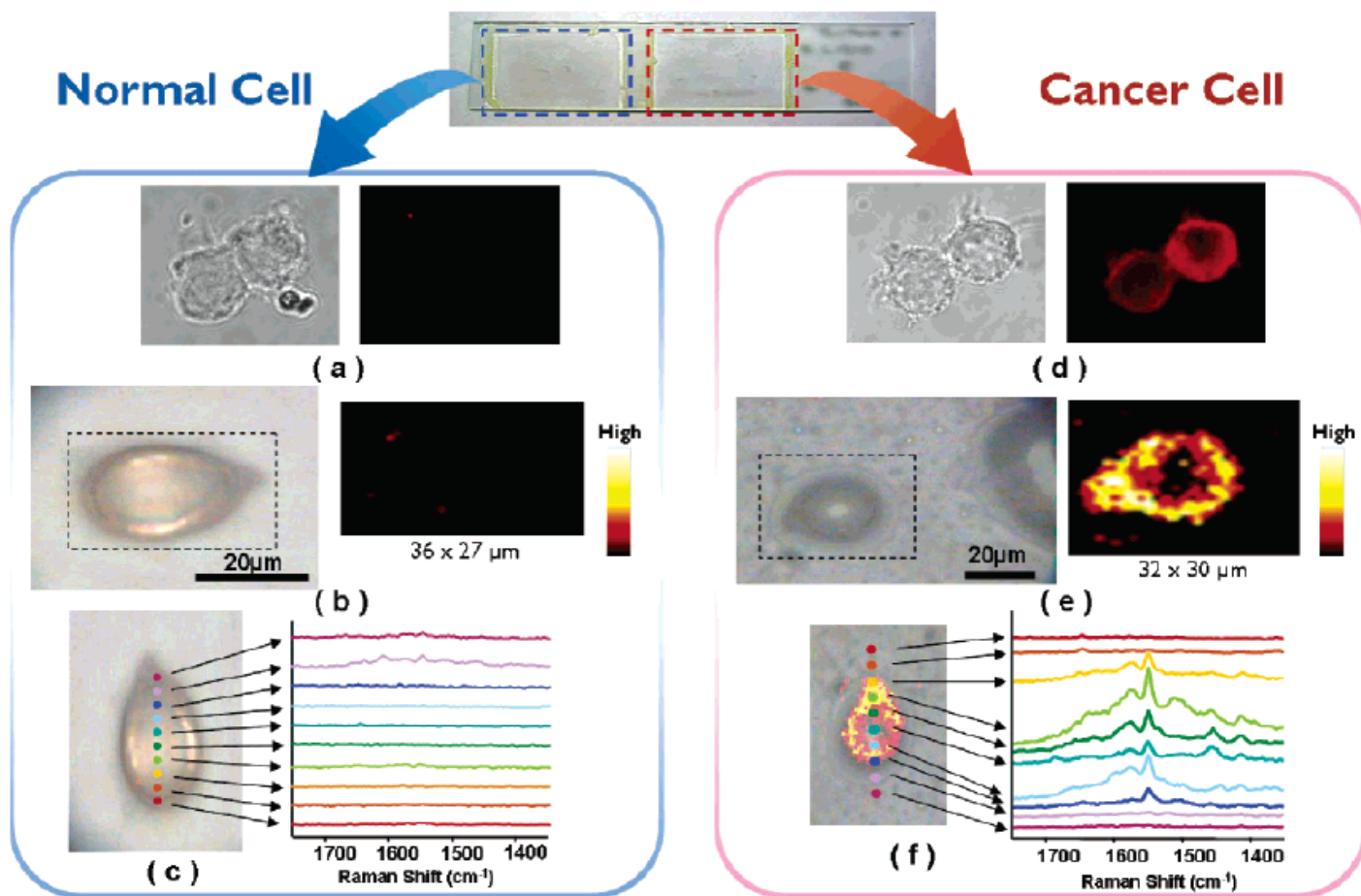


Figure 6. Fluorescence and SERS images of normal HEK293 cells and PLC γ 1-expressing HEK293 cells. (a) QD-labeled fluorescence images of normal cells: (left) brightfield image, (right) fluorescence image. (b) SERS images of single normal cell: (left) brightfield image, (right) Raman mapping image of single normal cell based on the 1650-cm $^{-1}$ R6G peak. The cell area was scanned with an interval of 1 μ m. Intensities are scaled to the highest value in each area. (c) Overlay image of brightfield and Raman mapping for single normal cell. Colorful spots indicate the laser spots across the middle of the cell along the y axis. (d) QD-labeled fluorescence images of cancer cells: (left) brightfield image, (right) fluorescence image. (e) SERS images of single cancer cell: (left) brightfield image, (right) Raman mapping image of single cancer cell based on the 1650-cm $^{-1}$ R6G peak. The cell area was scanned with an interval of 1 μ m. Intensities are scaled to the highest value in each area. (f) Overlay image of brightfield and Raman mapping for single cancer cell. Colorful spots indicate the laser spots across the middle of the cell along the y axis.

Mammalian Cell Surface Imaging with Nitrile-Functionalized Nanoprobes: Biophysical Characterization of Aggregation and Polarization Anisotropy in SERS Imaging

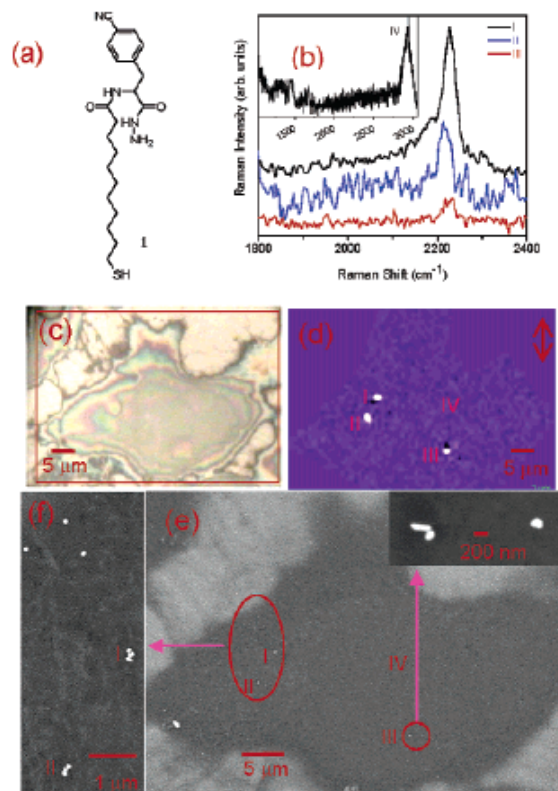


Figure 1. (a) The chemical structure of Raman reporter 1; (b) Raman spectra of the CN vibration mode extracted from positions I, II, and III of the cell shown in the optical image (c). Inset of (b) is a cellular Raman spectrum taken from spot IV of the same cell. (d) Raman intensity map of the C≡N band of the same cell, and (e) the corresponding SEM image. Inset in (e) showed the NPs in the lower right circle. (f) The group of NPs as shown in the large oval of (e).

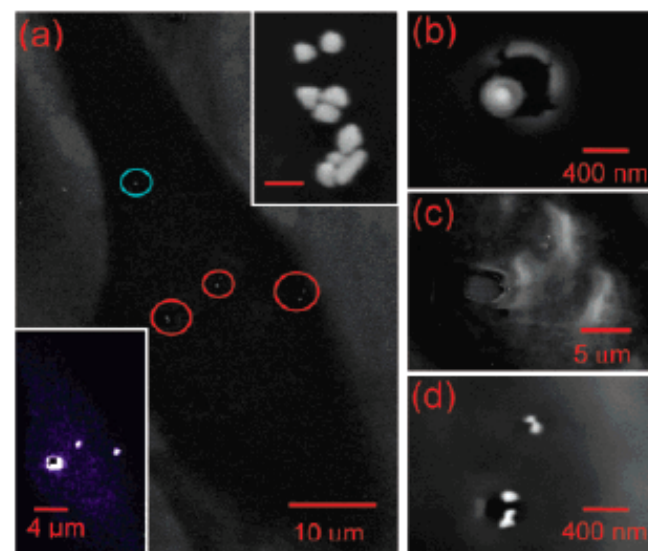
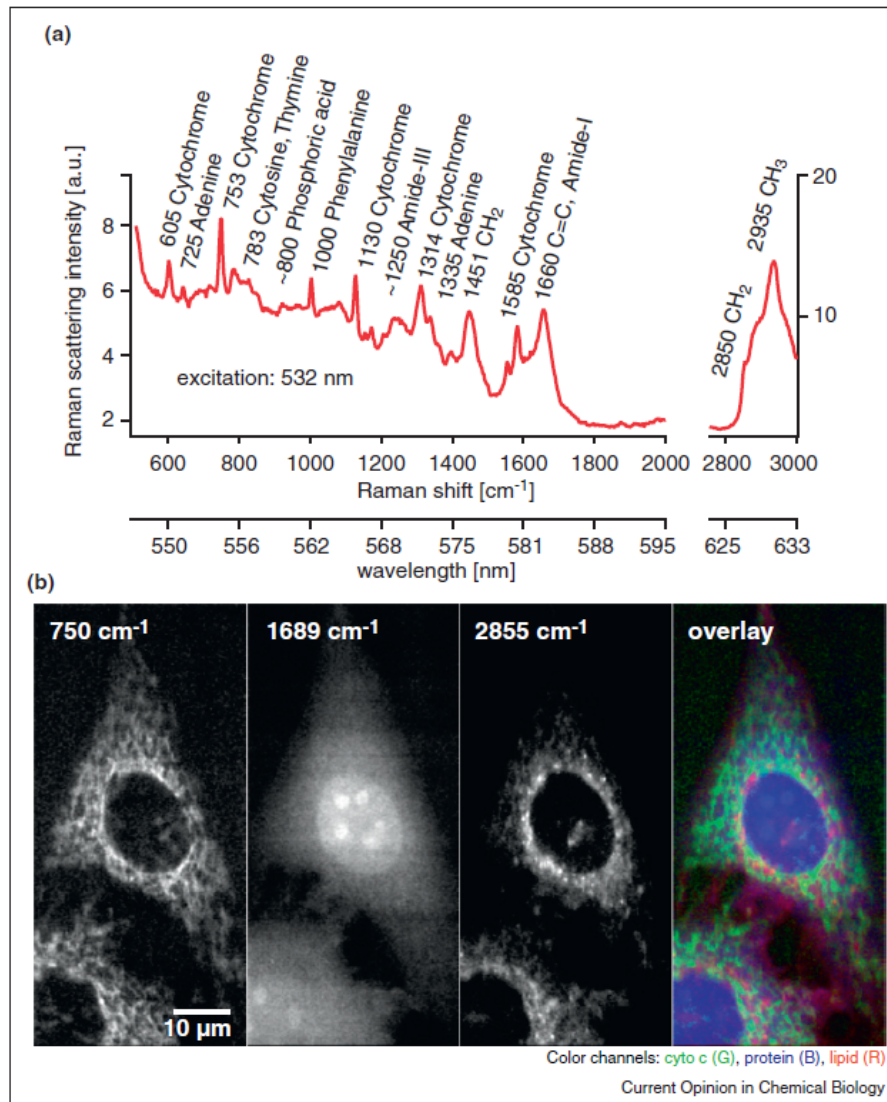


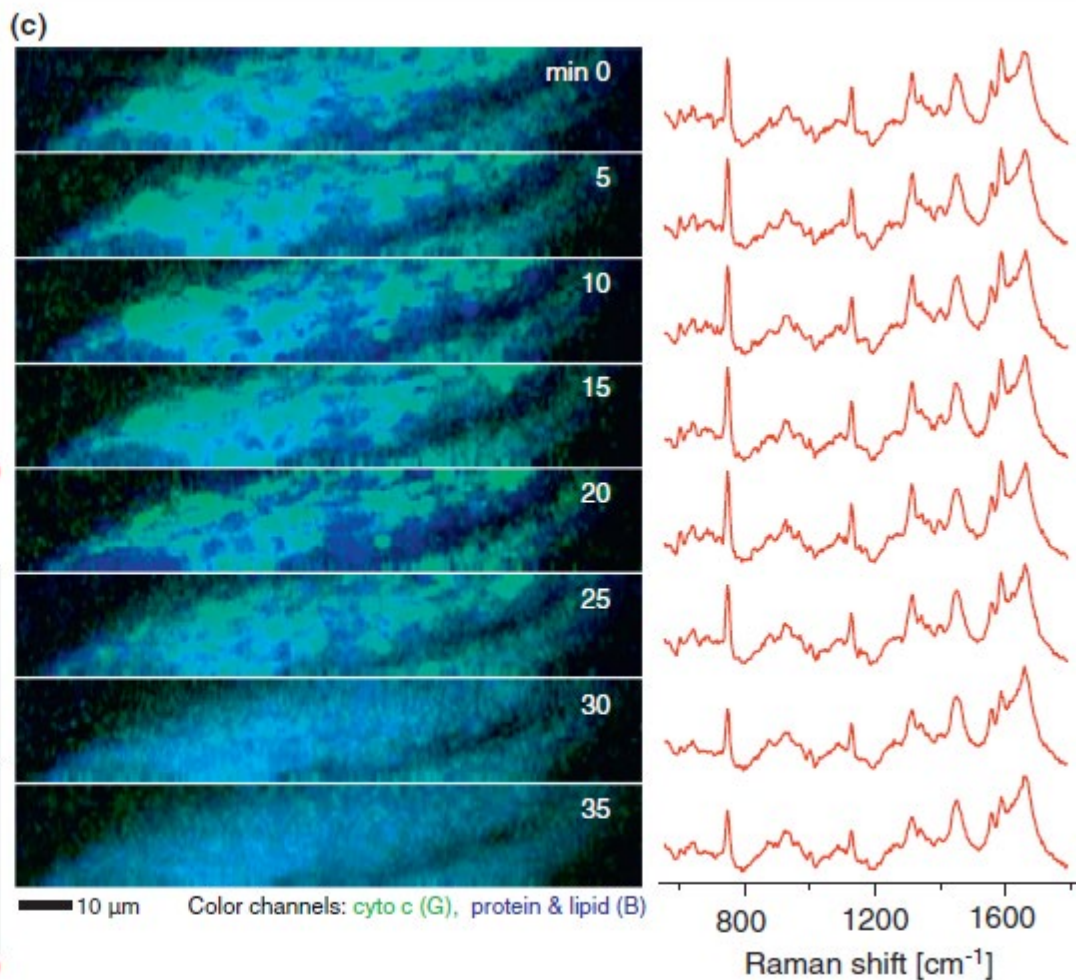
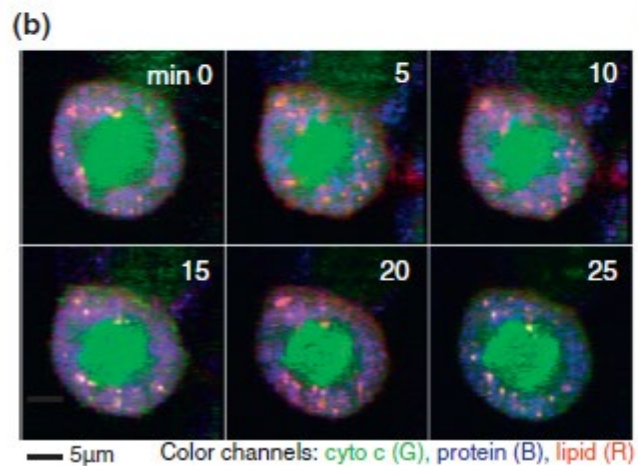
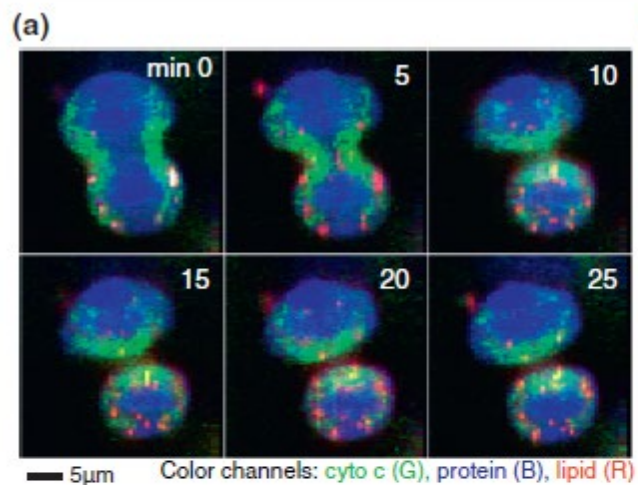
Figure 2. (a) SEM image of a cell. Upper right inset: magnification of a group of aggregated NPs. The scale bar is 200 nm. Lower left inset: the corresponding Raman intensity image of the same cell obtained with a power density of 10^5 W/cm². Laser-induced damage to the cell is shown in (b) the monomer (blue circle in a), (c) the aggregates, and (d) a pair of dimers.

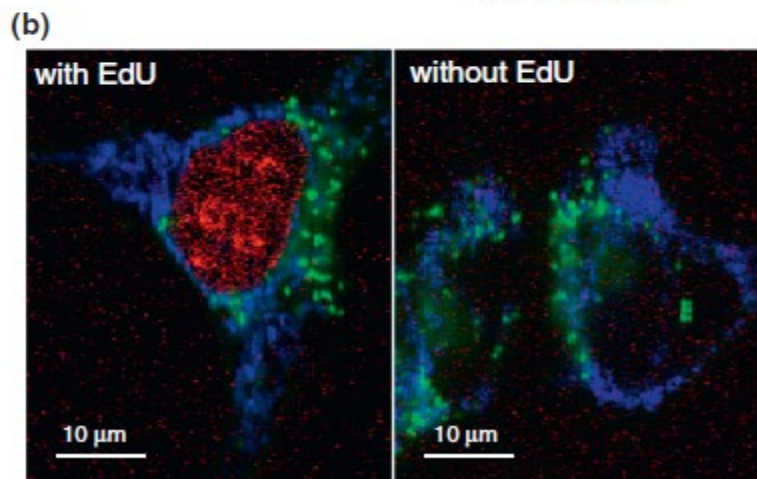
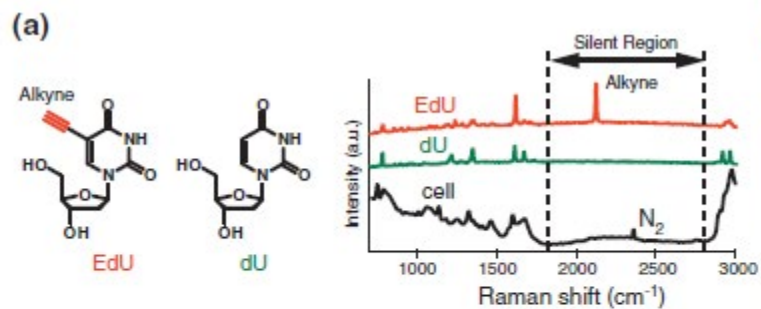
Molecular imaging of live cells by Raman microscopy

Almar F Palonpon^{1,2}, Mikiko Sodeoka^{2,3} and Katsumasa Fujita^{1,2}

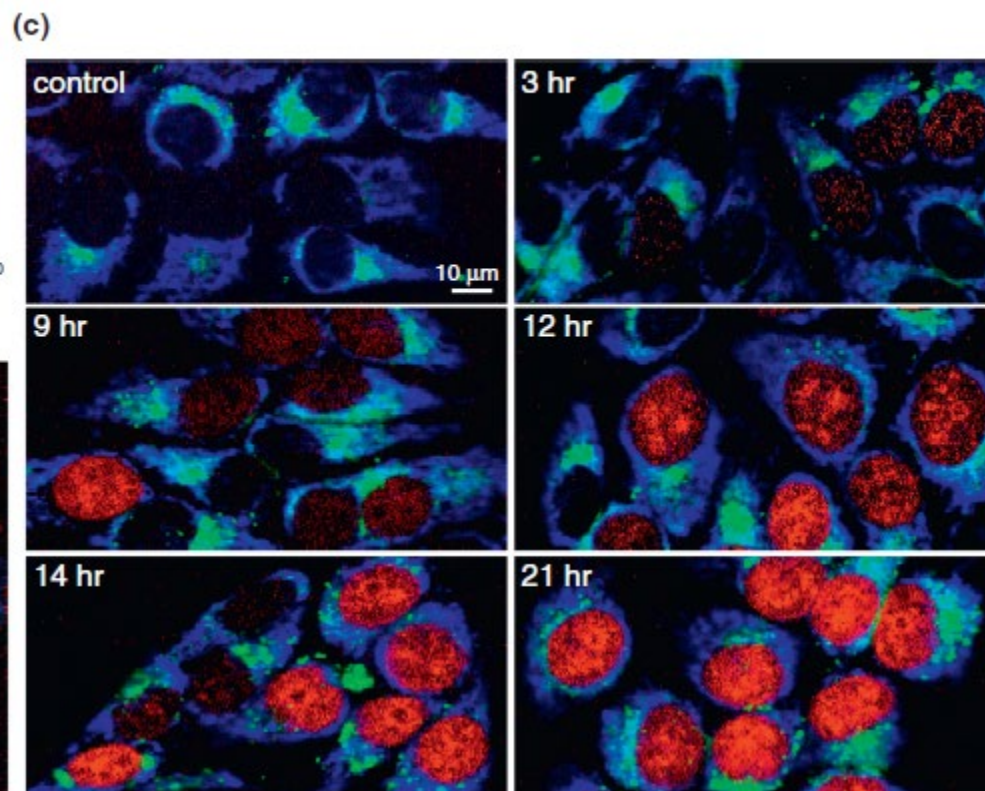
Current Opinion in Chemical Biology 2013, 17:708–715



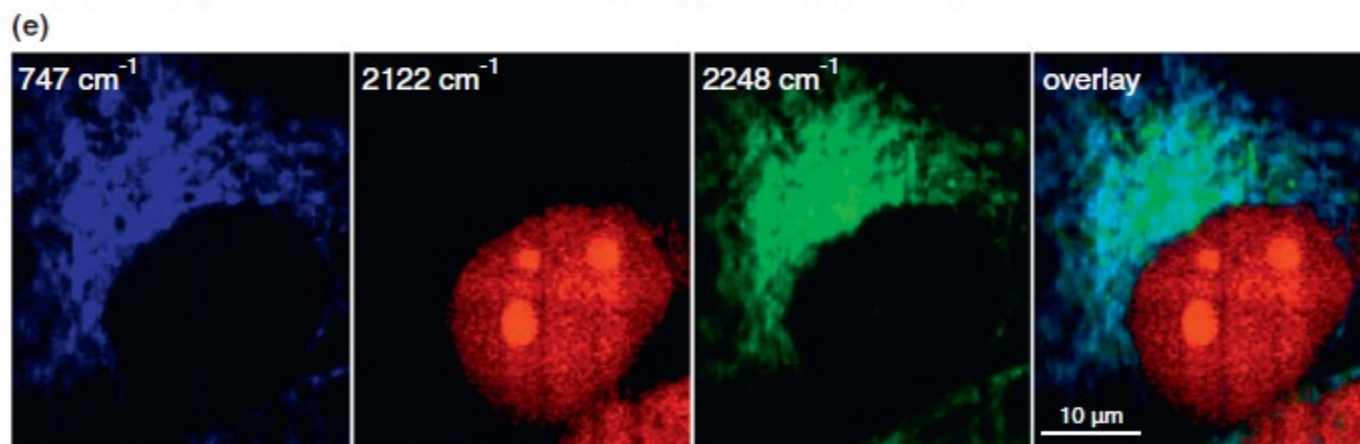
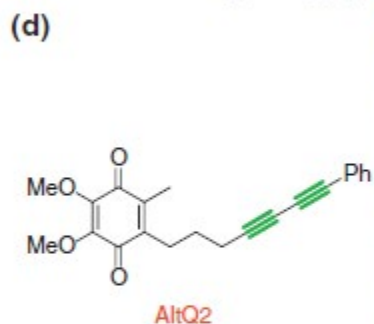




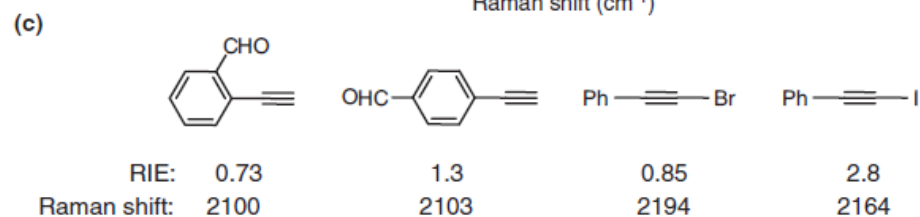
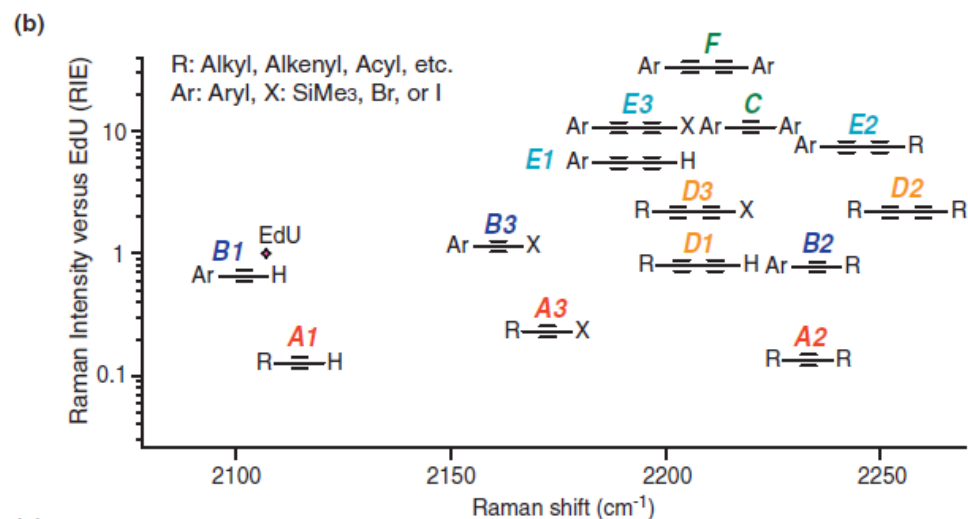
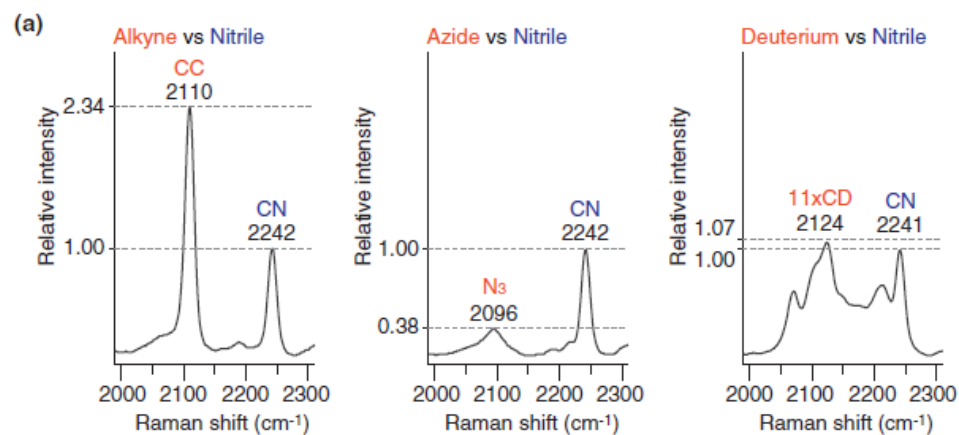
Color channels: cyto c (B), protein (G), EdU (R)



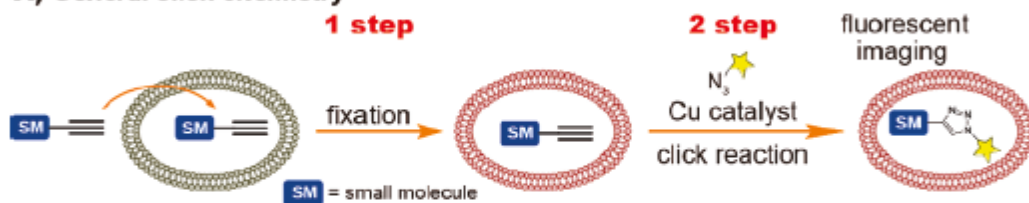
Color channels: cyto c (B), protein (G), EdU (R)



Color channels: cyto c (B), EdU (R), AltQ2 (G)



A) General click chemistry



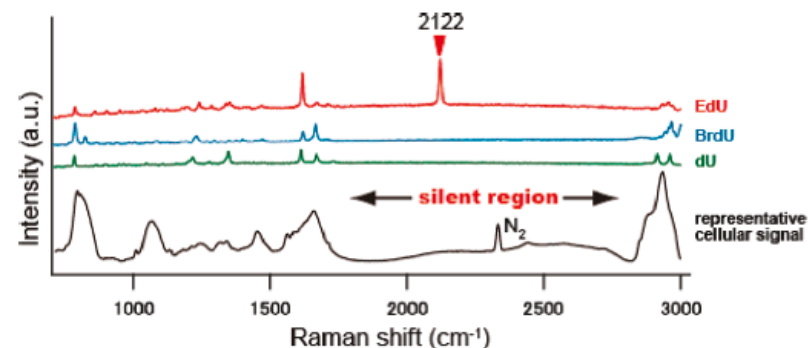
B) Cu-free click chemistry



C) This time (Click-free)



Figure 1. Concept of click-free imaging.



alkyne tag

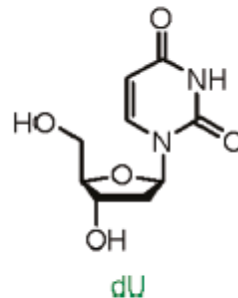
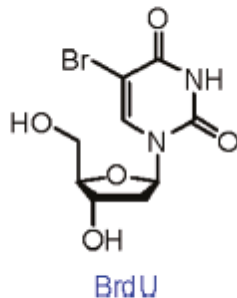
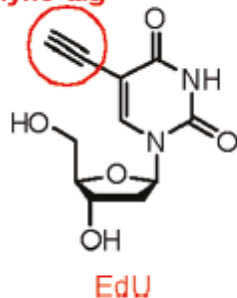
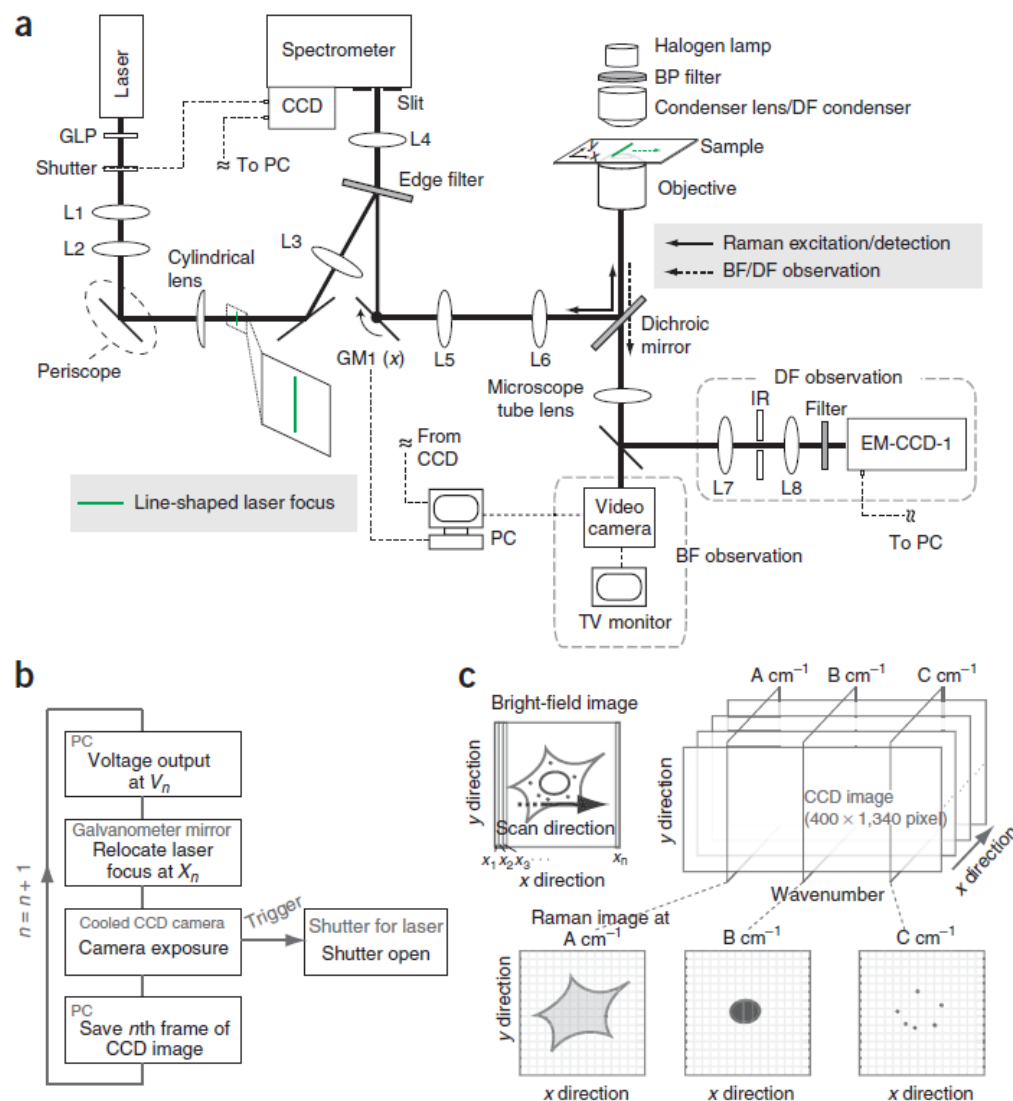
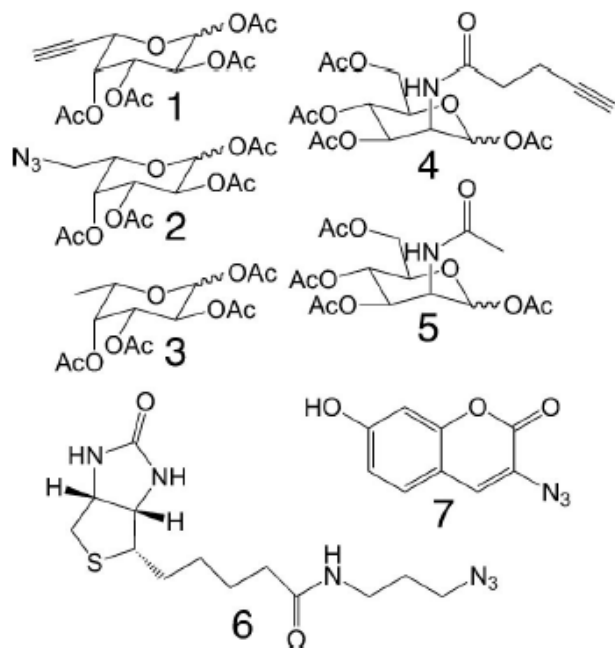


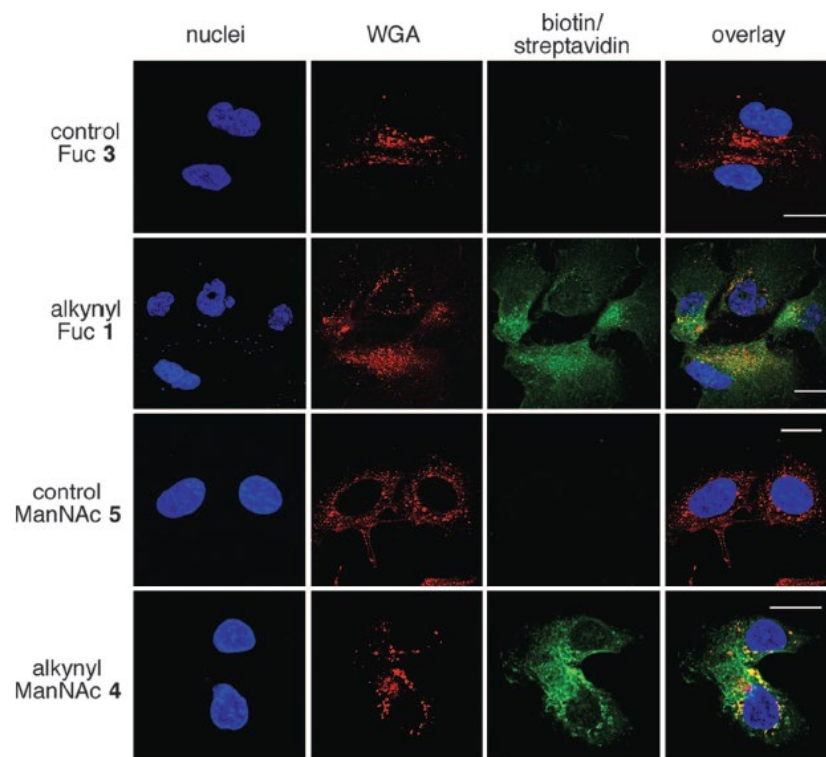
Figure 2. Structures of thymidine analogues.



Alkynyl sugar analogs for the labeling and visualization of glycoconjugates in cells



Scheme 1. Modified sugar analogs and probes used in this study.



Cell-permeable probe for identification and imaging of sialidases

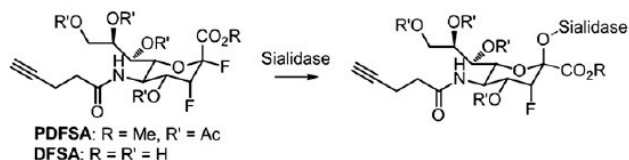
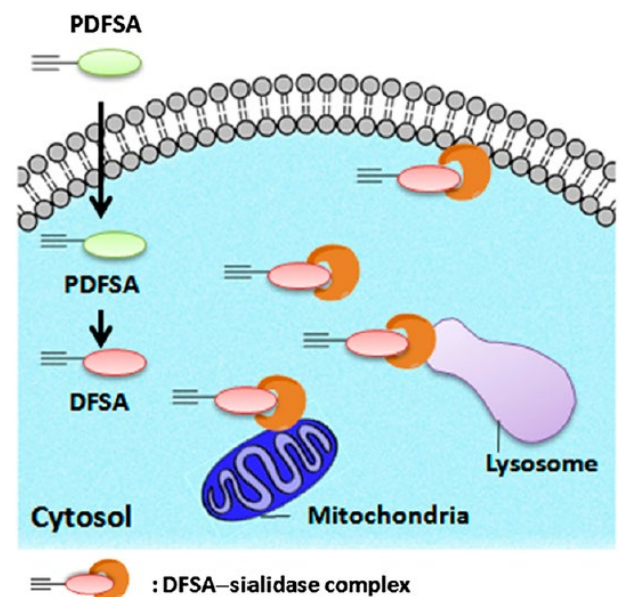
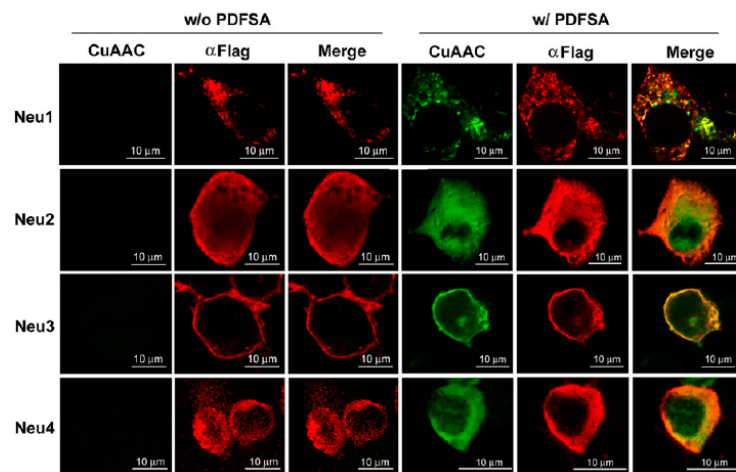
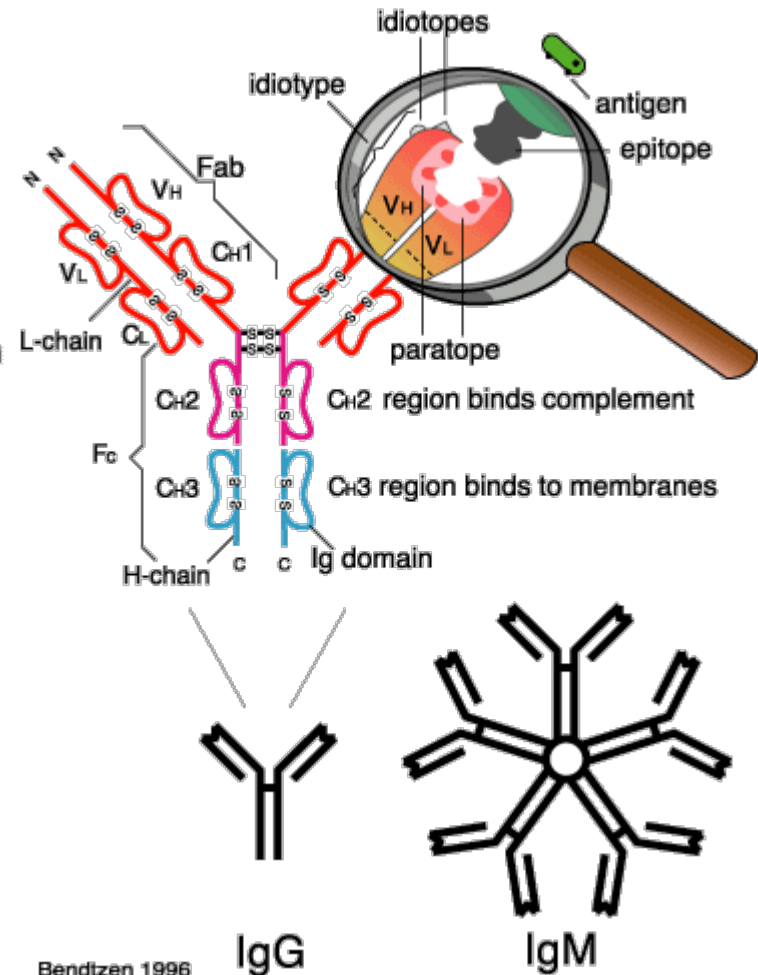
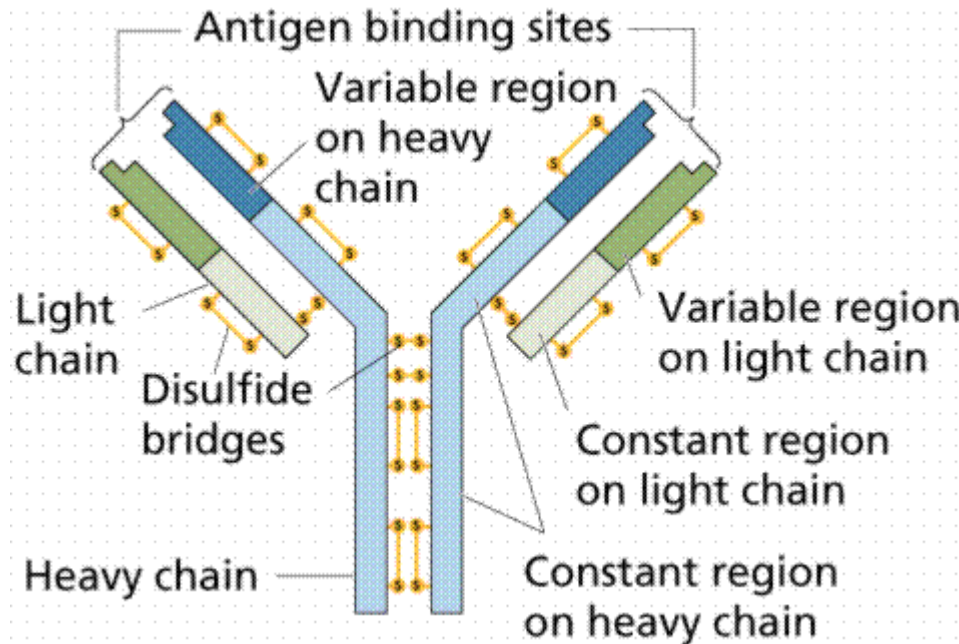


Fig. 1. Identification and imaging of sialidase with activity changes using these activity-based sialidase probes.



Antibody and Antigen

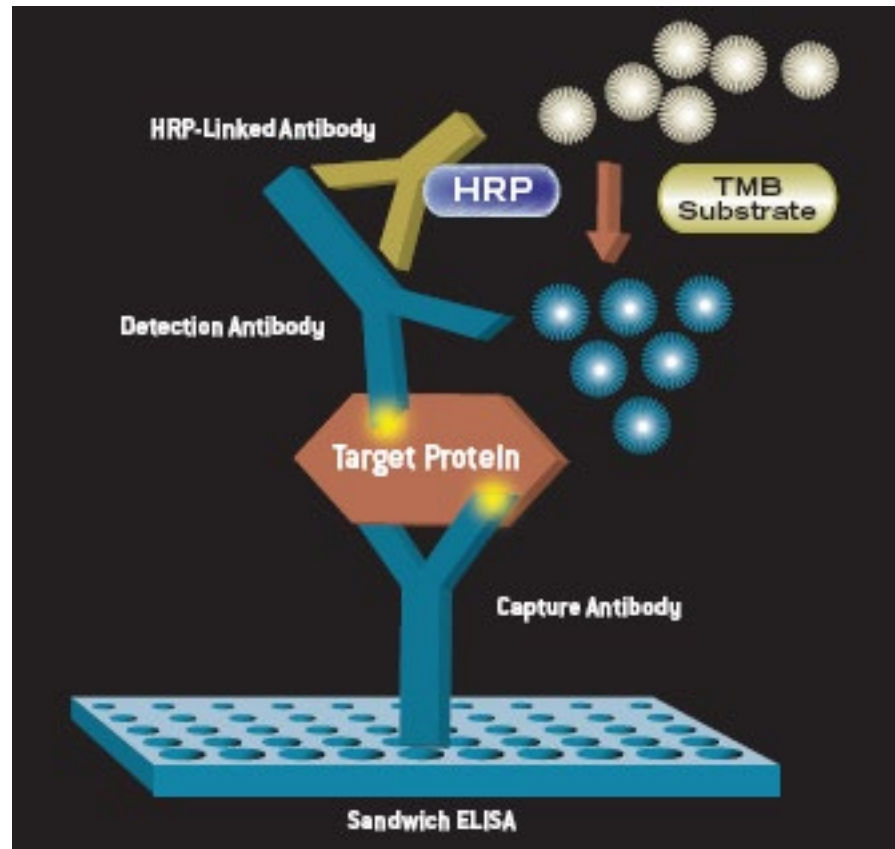


Bendtsen 1996

IgG

IgM

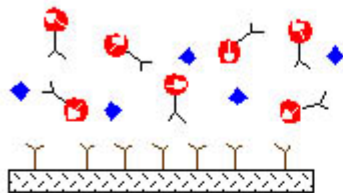
Enzyme-Linked ImmunoSorbent Assay (ELISA)



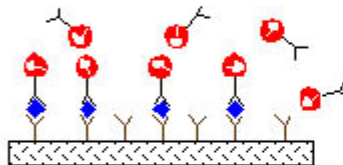
Labeling
BSA/PEG

Microarray

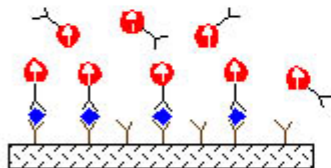
◆ Biomolecules of interest Y Capture antibody [hatched box] Solid support [red circle with Y] Magnetically labeled antibody



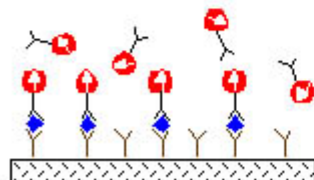
Add biomolecules of interest and magnetically labeled detect antibodies to well coated with capture antibody.



Immobilized immune complexes form on solid support.



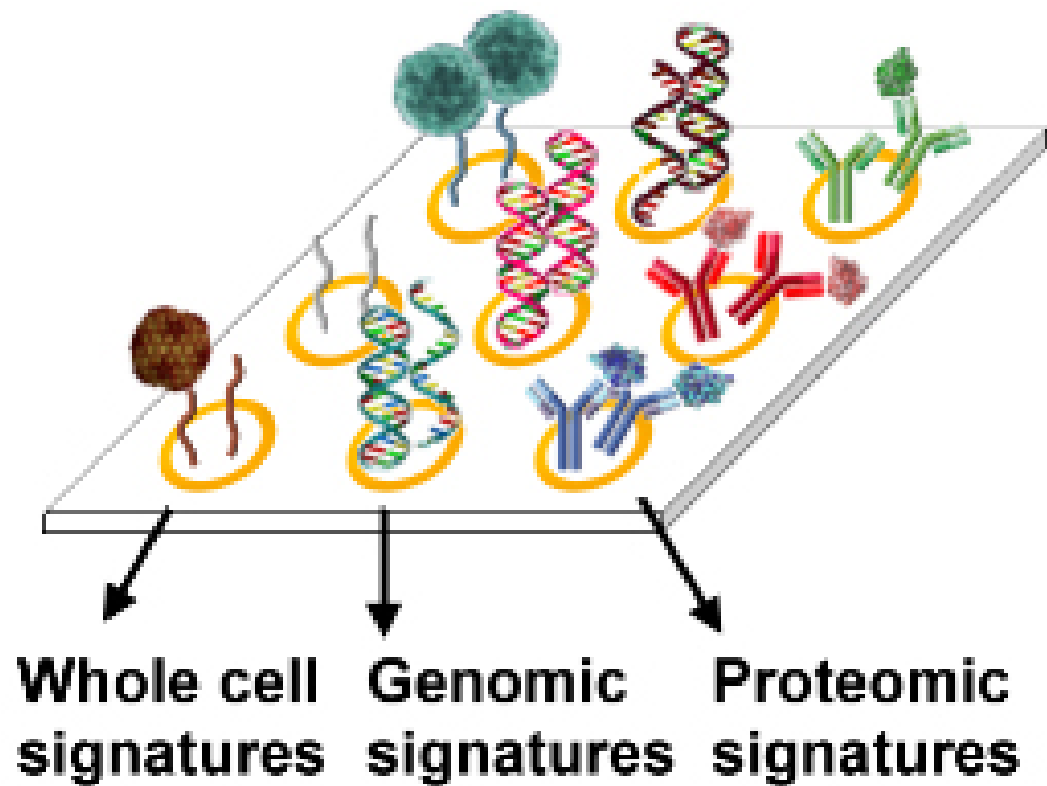
Apply external magnetic field, magnetic dipoles align.



Remove field, measure net magnetization due to bound antibody labels. Unbound labels randomize quickly and contribute no net signal.

Detector

Microarray



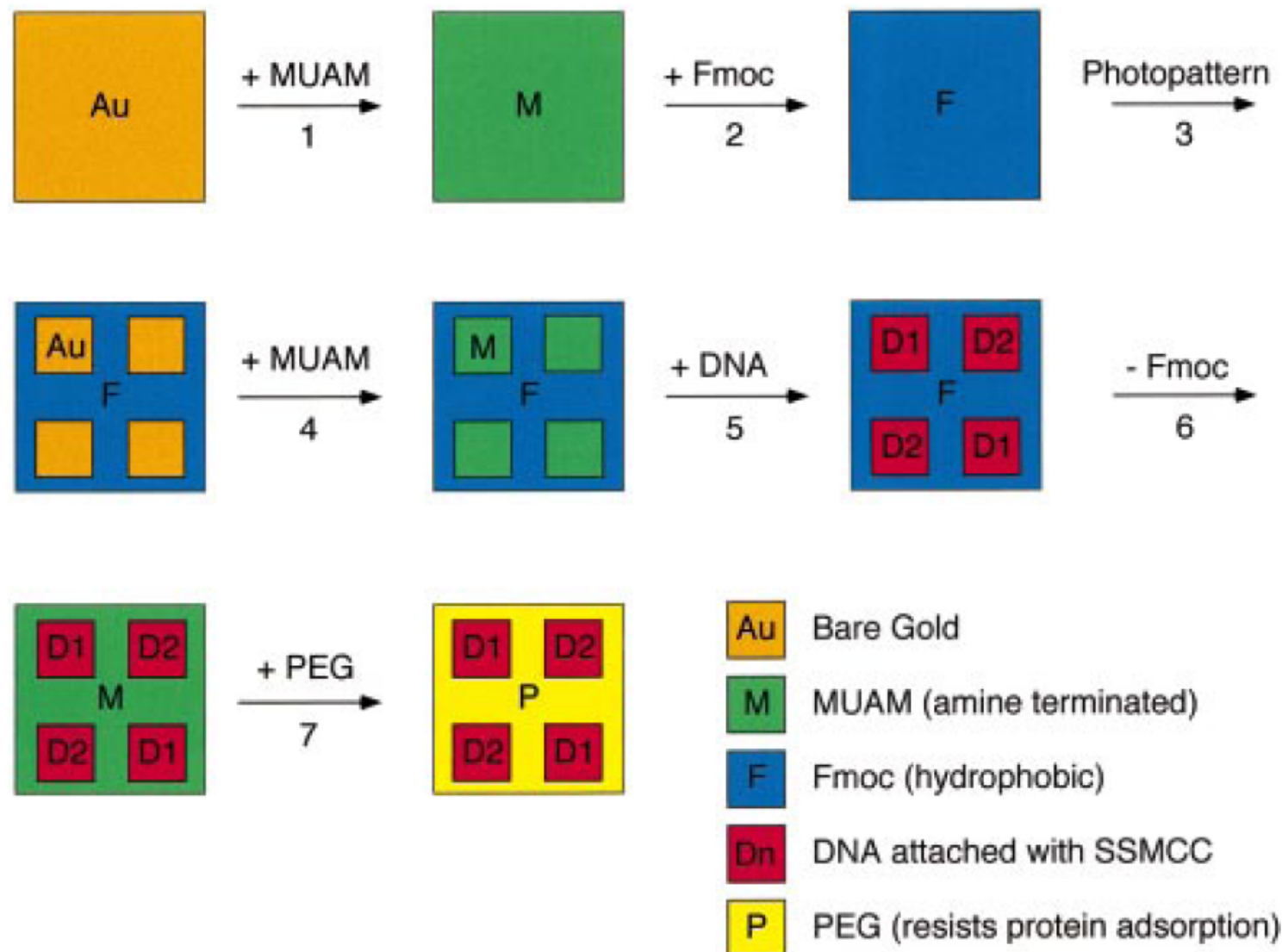


Figure 1. Fabrication scheme for the construction of multi-element DNA arrays. A clean gold surface is reacted with the amine-terminated alkanethiol MUAM, and subsequently reacted with Fmoc-NHS to create a hydrophobic surface. This surface is then exposed to UV radiation through a quartz mask and rinsed with solvent to remove the MUAM+Fmoc from specific areas of the surface, leaving bare gold pads. These bare gold areas on the sample surface are filled in with MUAM, resulting in an array of MUAM pads surrounded by a hydrophobic Fmoc background. Solutions of DNA are then delivered by pipet onto the specific array locations and are covalently bound to the surface via the bifunctional linker SSMCC. In the final two steps, the Fmoc-terminal groups on the array background are removed and replaced by PEG groups which prohibit the nonspecific binding of analyte proteins to the background.

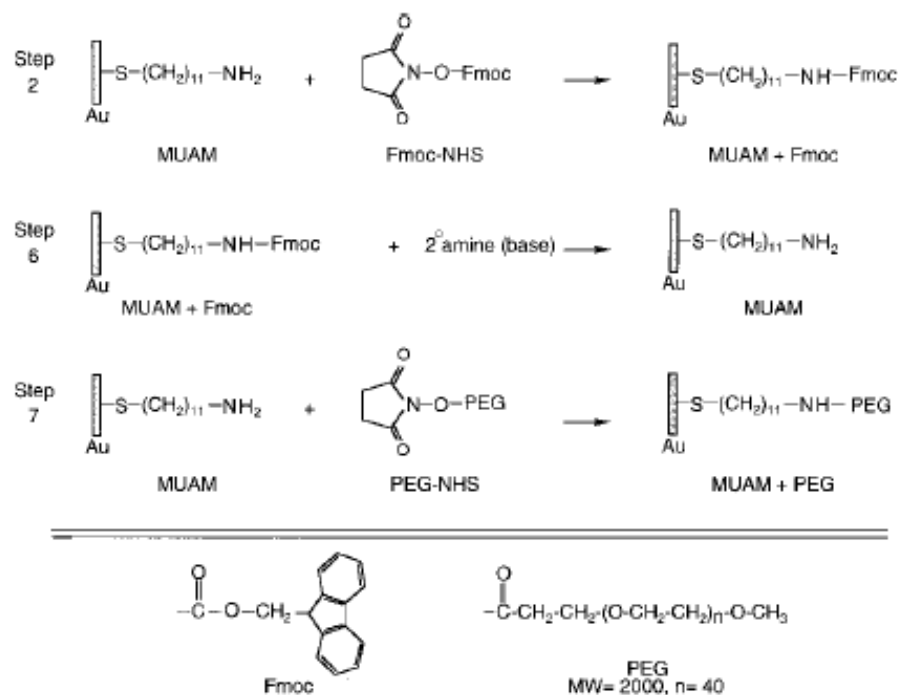


Figure 2. Surface reaction scheme showing the steps involved in the reversible modification of the array background. (Step 2) The starting amine-terminated alkanethiol surface (MUAM) is reacted with the Fmoc-NHS protecting group to form a carbamate linkage thus creating a hydrophobic Fmoc-terminated surface. (Step 6) After DNA immobilization (see Figure 3), the hydrophobic Fmoc group is removed from the surface with a basic secondary amine, resulting in the return of the original MUAM surface. (Step 7) In the final array fabrication step, the deprotected MUAM is reacted with PEG-NHS to form an amide bond that covalently attaches PEG to the array surface.

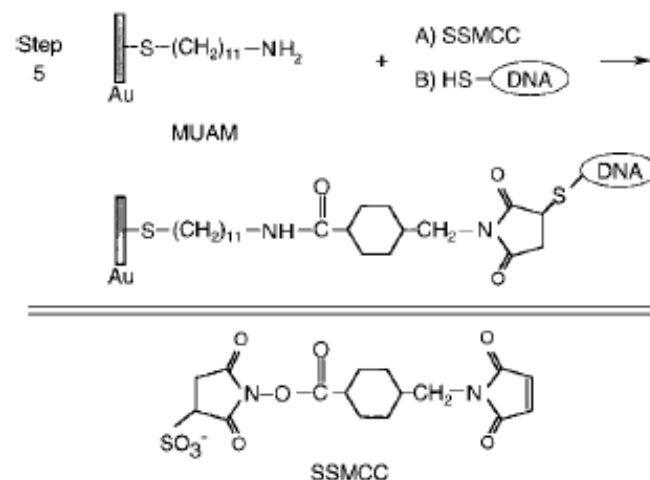
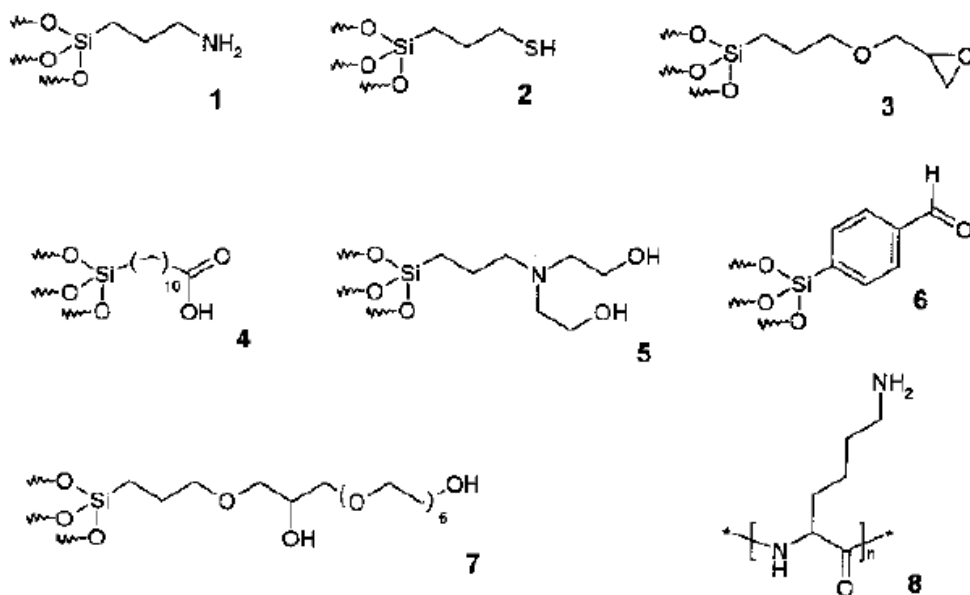
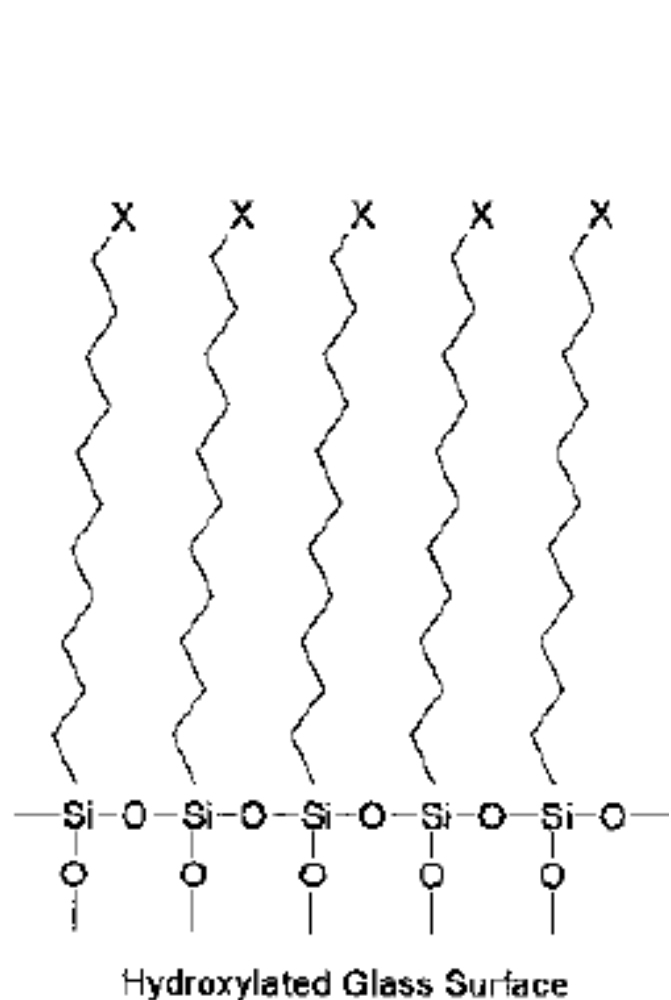


Figure 3. Surface reaction scheme showing the immobilization of thiol-terminated DNA to the array surface. In Step 5 of the DNA array fabrication, the heterobifunctional linker SSMCC is used to attach 5'-thiol modified oligonucleotide sequences to reactive pads of MUAM. This linker contains an NHSS ester functionality (reactive toward amines) and a maleimide functionality (reactive toward thiols). The surface is first exposed to a solution of the linker, whereby the NHSS ester end of the molecule reacts with the MUAM surface. Excess linker is rinsed away and the array surface is then spotted with 5'-thiol-modified DNA that reacts with the maleimide groups forming a covalent bond to the surface monolayer.

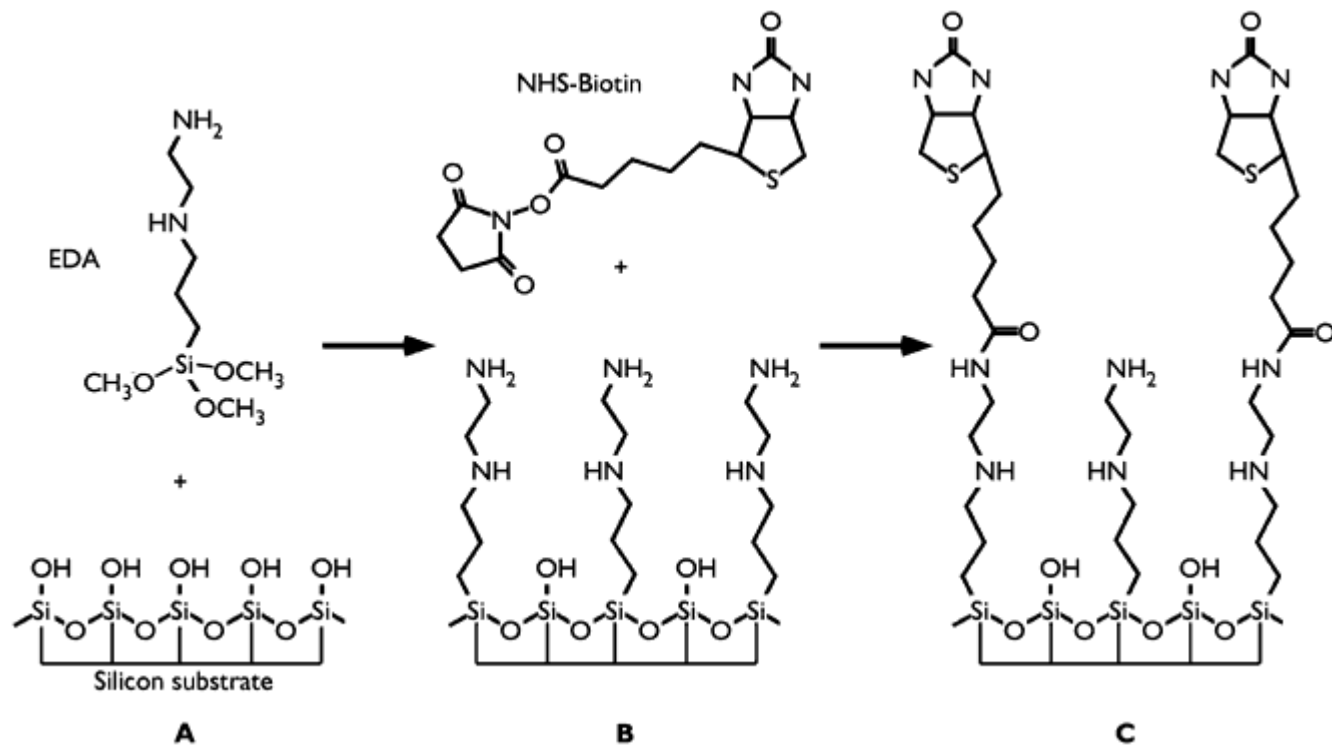
Glass Surface Modification



Scheme 2.2 Reagents for derivatization of glass surfaces. 1 APTES = aminopropyltriethoxysilane; 2 MPTS = 3-mercaptopropyltrimethoxysilane; 3 GPTS = glycidoxypropyltrimethoxysilane; 4 TETU = triethoxysilane undecanoic acid;

5 HE-APTS = bis(hydroxyethyl)aminopropyltriethoxysilane); 6 4-trimethoxysilylbenzaldehyde; 7 GPTS/HEG = glycidoxypropyltrimethoxysilane-hexaethylene glycol; 8 poly(lysine).

Scheme 2.1 2D schematic description of a polysiloxane monolayer on a glass surface (X = terminal functional



Biotin-Streptavidin

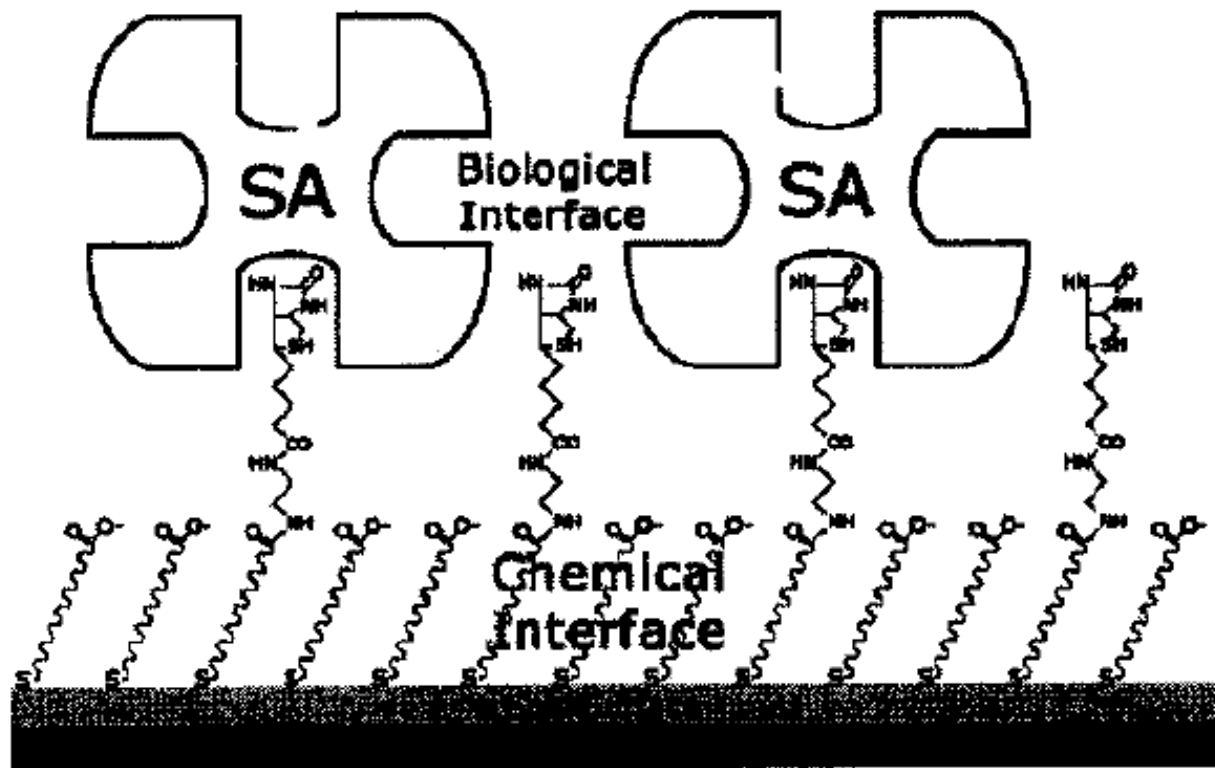
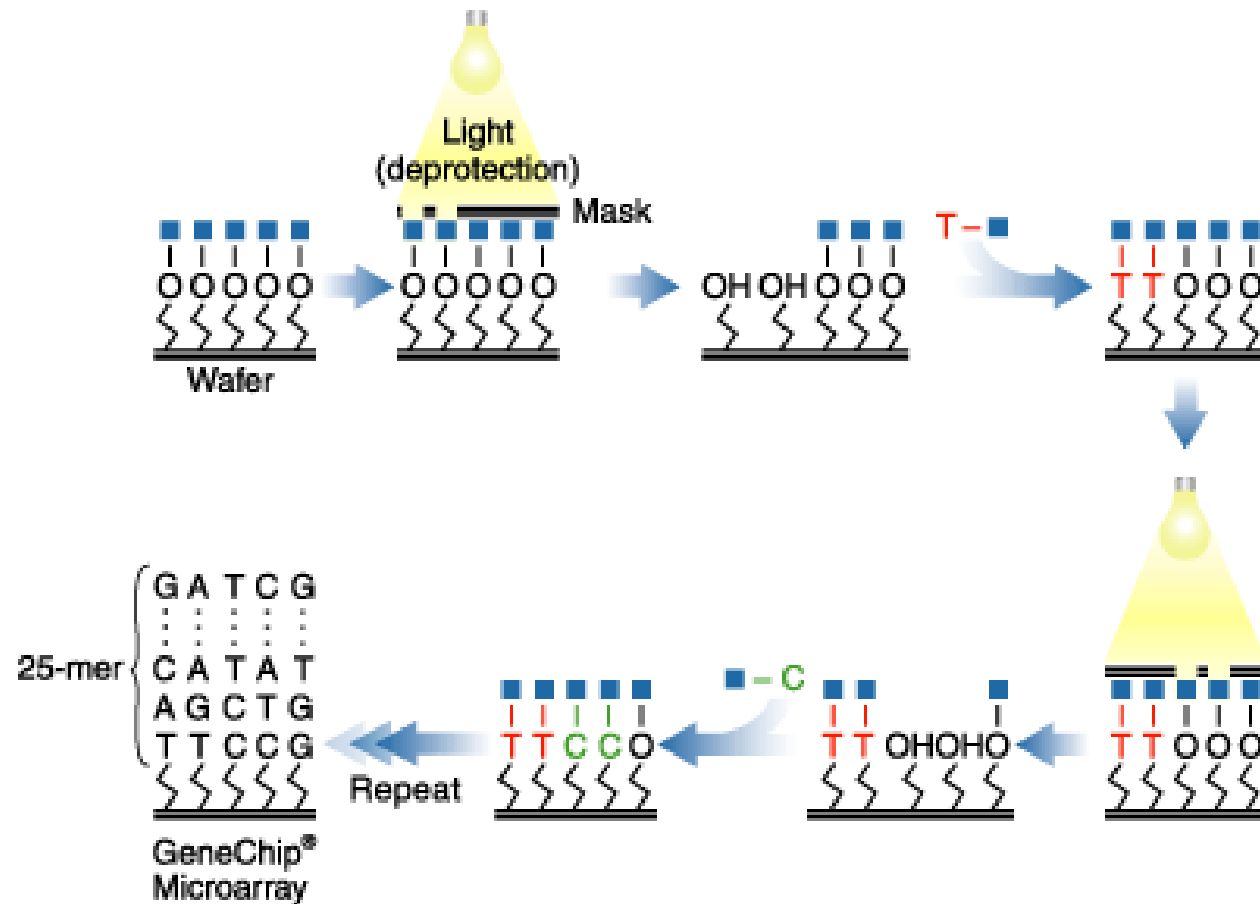
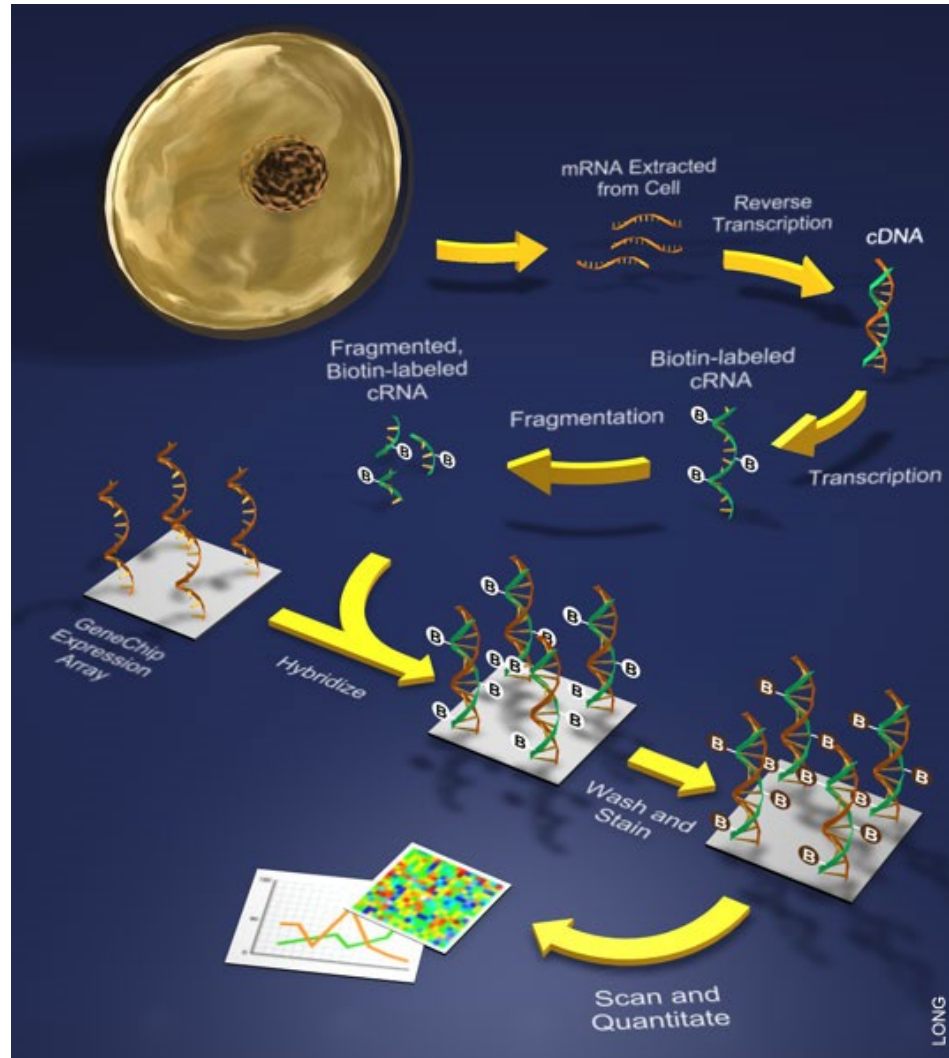


Figure 2.3 Schematic representation of a streptavidin sensor surface assembled on a reaction-controlled biotinylated SAM [28].

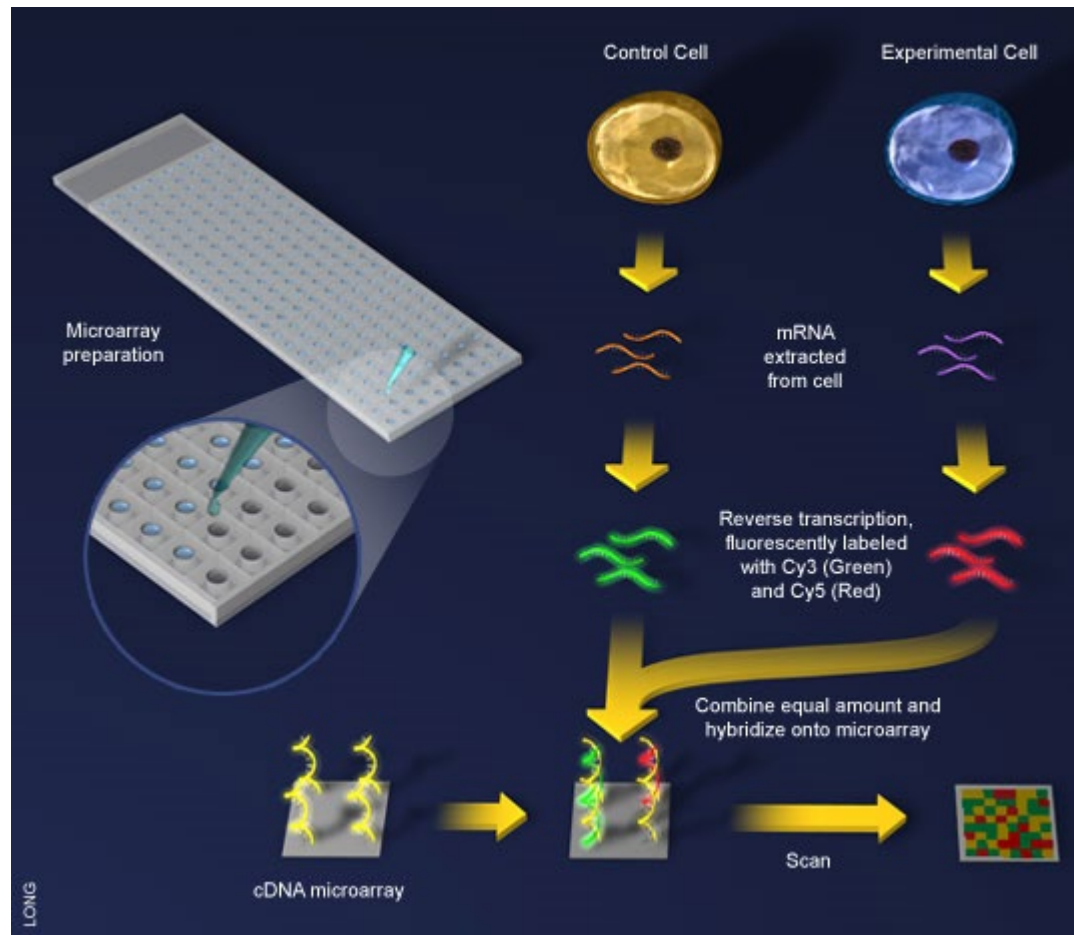
GeneChip



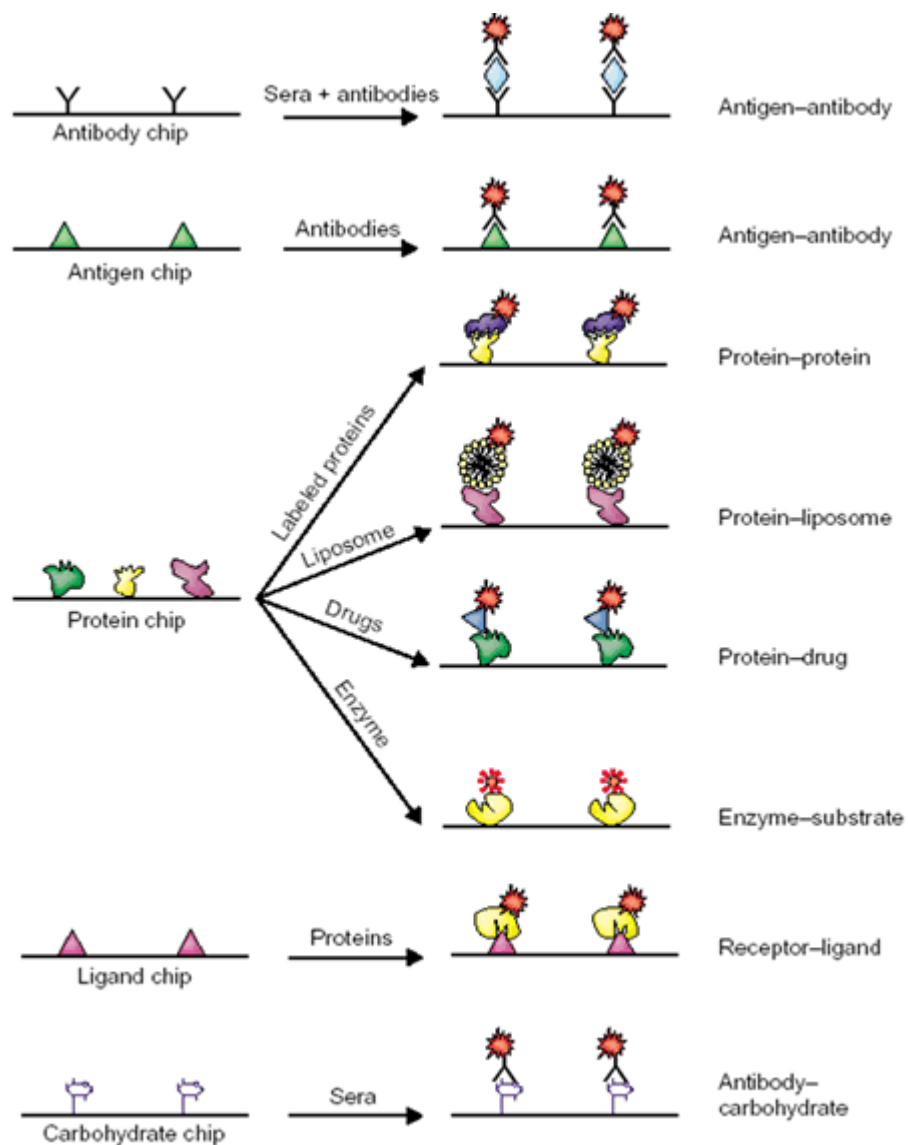
Scheme



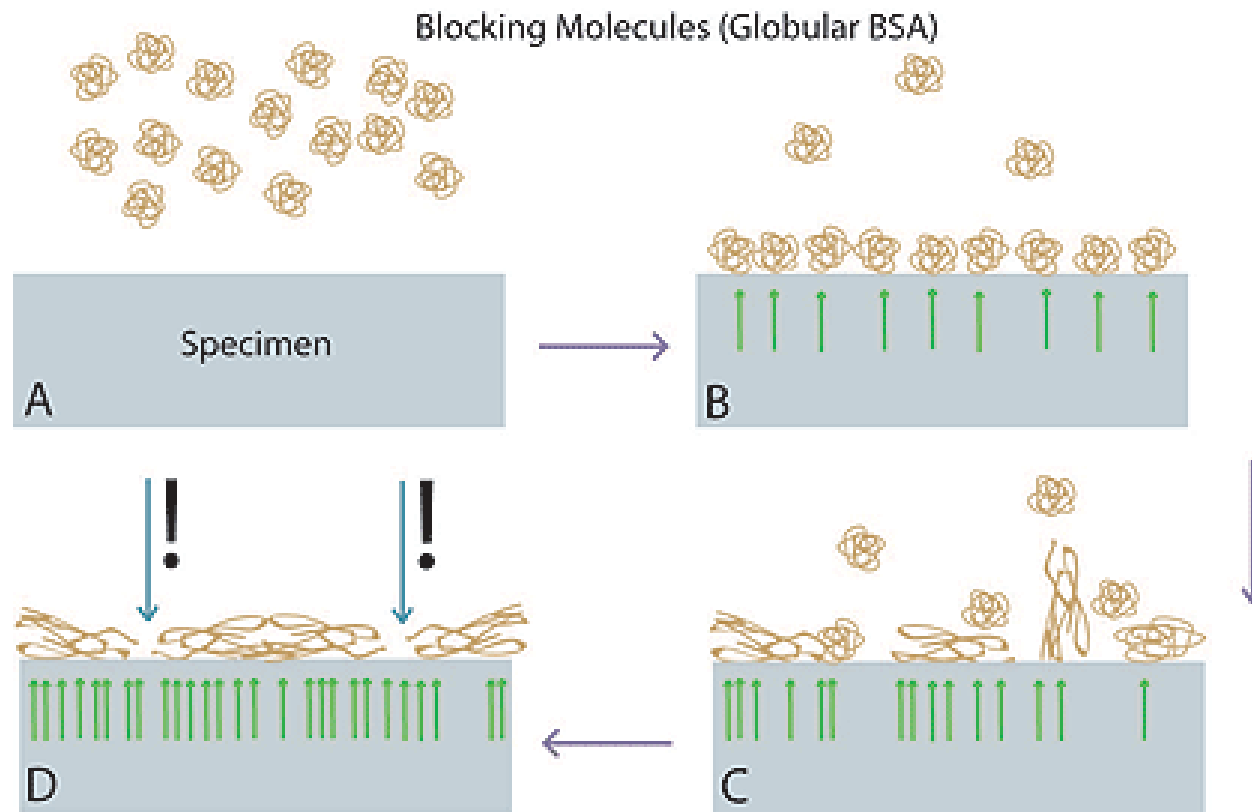
cDNA Microarray



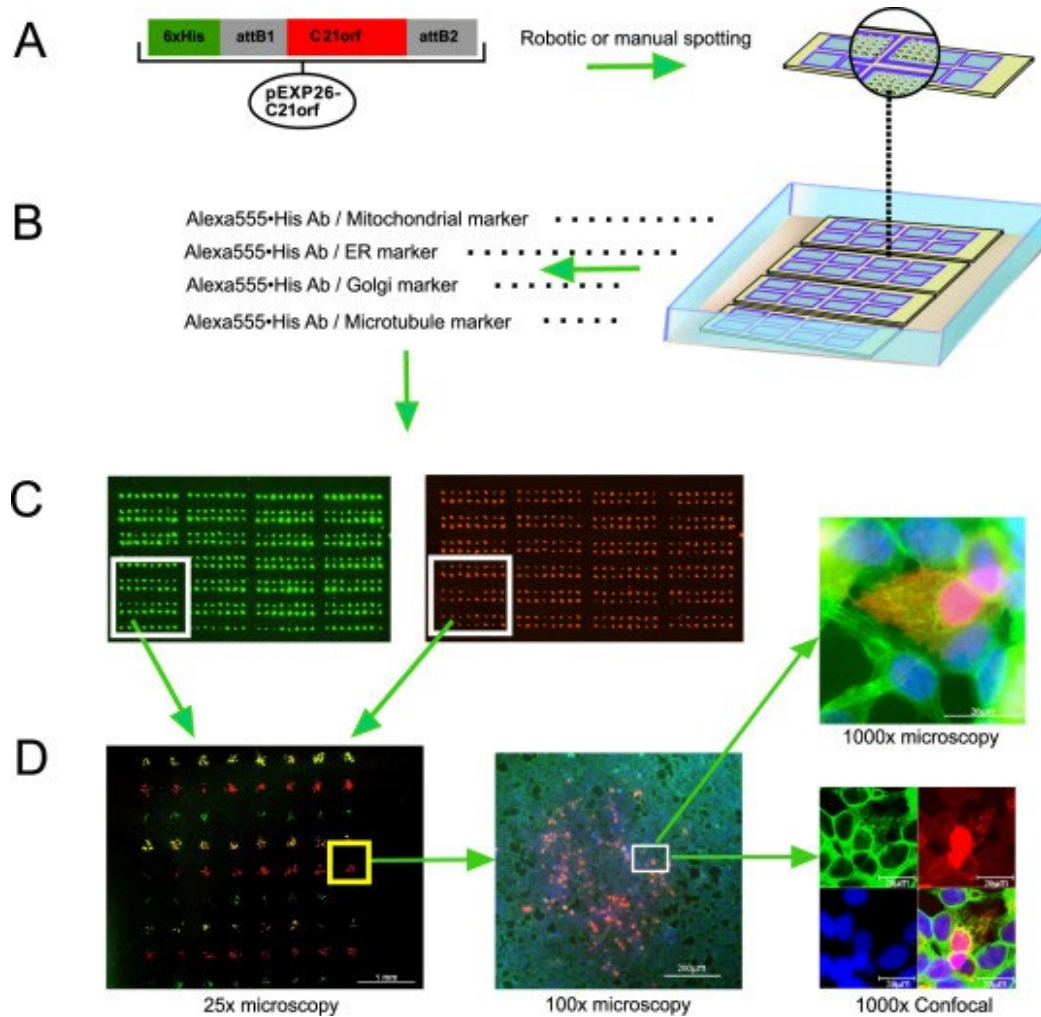
Protein Array



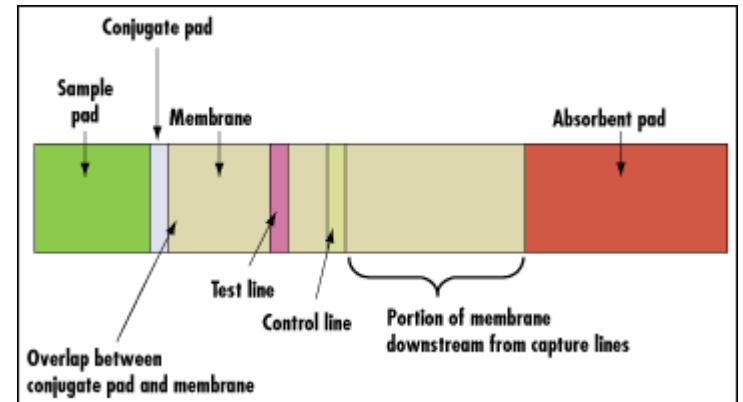
BSA Blocking



Cell Array



hCG immunoassay



human chorionic gonadotropin (hCG)

Nucleotide Sensor

